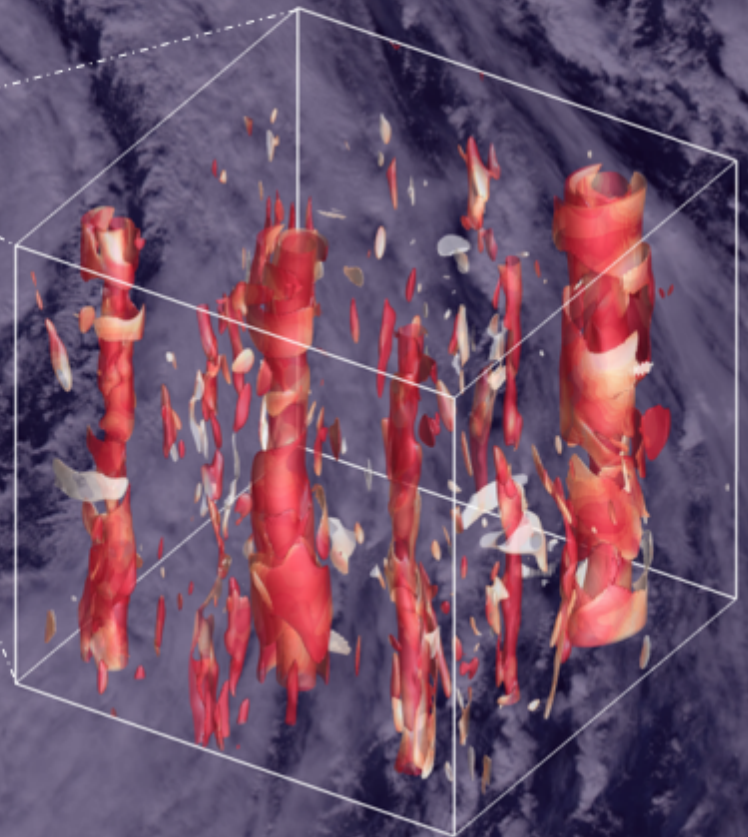


Master of Science Thesis

Explicit Algebraic Subgrid-Scale Stress Model for Homogeneous Turbulence

A.K.Gnanasundaram

May 9, 2018



Explicit Algebraic Subgrid-Scale Stress Model for Homogeneous Turbulence

Master of Science Thesis

For obtaining the degree of Master of Science in Aerospace Engineering
at Delft University of Technology

A.K.Gnanasundaram

May 9, 2018



Delft University of Technology

Copyright © Aerospace Engineering, Delft University of Technology
All rights reserved.

DELFT UNIVERSITY OF TECHNOLOGY
DEPARTMENT OF AERODYNAMICS

The undersigned hereby certify that they have read and recommend to the Faculty of Aerospace Engineering for acceptance the thesis entitled “**Explicit Algebraic Subgrid-Scale Stress Model for Homogeneous Turbulence**” by **A.K.Gnanasundaram** in fulfillment of the requirements for the degree of **Master of Science**.

Dated: May 9, 2018

Prof.dr. S. Hickel

T.C. Pestana

Dr.ir. C.J. Simao Ferreira

Dr. S.J. Hulshoff

Acknowledgement

I have imagined this day in my mind so many times, even call it a fantasy. A milestone merely because I have everything in order to print my thesis. Of course, there were tough days during my thesis. “Sometimes things just don’t work”, said someone in the MSc thesis room. Those are the times when you look for support from fellow colleagues, friends or family. Fortunately, I had a surplus of that.

I am most grateful to my supervisors, Prof. dr. Stefan Hickel, and (soon to be dr.) Tiago Pestana. Firstly, for offering me a challenging and interesting topic for thesis, and secondly, for always patiently resolving any issues I had pertaining to my thesis. Tiago was assigned as my daily supervisor and he really was a DAILY supervisor. I am much indebted for all the times he used to sit with me deriving different equations and most of all for the extensive code repository that he shared with me. I really appreciate the scheduled Skype calls even during Christmas vacation, advising me on my first ever Fortran code. With Stefan, I have had conversations/meetings that lasted from 2 minutes to sometimes more than 2 hours. I am very thankful for the time he spared for me, especially, given how busy he is.

I owe a great deal to the friends I made in Delft. I thought that I was a dramatic person until I met Zeynep. For all the chit-chats, jam sessions, and other countless endeavours, I am grateful. To Giulia-my artistic friend and Panos-the guy who will forever be remembered for introducing me to fredoespresso, I am much grateful. To Mirely and Mattia: my travel companions in a fun trip and for the random dinners, I am thankful. The basement: the place that inevitably became something of a home to us. To all the friends I made during my thesis working alongside each other; to Blanca, for always being cheerful, to Alex, Ka Hin, and Sumedh, for the massive Barbecues and the fun talks, to Jordi, for the ‘scientific’ talks we had, to Gigi, for being the co-founder of the walk-breaks, to Edo, for criticising my ‘pastas’ and all the others I might have missed (it is quite a long list), I owe a great deal of gratitude. They witnessed first hand my excitement, frustration, and quirky ideas, and put up with all of that.

Finally, I thank the two people who brought me into this world and the guy whose toys I stole and broke as a kid, my parents and my brother. Their constant support, was more than instrumental in the completion of my thesis. For that and much more, I am and will be forever indebted to them.

That said, I invite you to read the story of my thesis. Spoilers are in the title!

Arun Kumar Gnanasundaram
Delft, The Netherlands,
May 9, 2018

Abstract

The whole construct of explicit algebraic Reynolds stress models, as they are known in RANS, is based on the weak equilibrium assumption. By employing this assumption, and in addition, incorporating models for terms in the Reynolds stress transport equations, the system of six partial differential equations can be simplified to an algebraic form. However, the resulting equations are non-linear in terms of the Reynolds stress anisotropy and therefore become implicit. The cause of the non-linearity is the presence of the ratio of kinetic energy production to dissipation (\mathcal{P}/ϵ) in the equations. In order to derive an explicit model for the Reynolds stress anisotropy, methods to determine \mathcal{P}/ϵ are required. For RANS, there are many variations of the final formulation based on the procedure by which this ratio is determined. [Marstorp et al. \(2009\)](#) provide an extension of this modelling framework used in RANS to LES in order to model subgrid-scale (SGS) stresses. In their formulation, the value of \mathcal{P}/ϵ , which in LES is the ratio of SGS kinetic energy production to dissipation, is specified as 1, thereby obviating any need for treating non-linearities in the equations.

In this thesis, the performance of the explicit algebraic subgrid-scale stress model (EASSM) developed by [Marstorp et al. \(2009\)](#) is tested in comparison with the dynamic Smagorinsky model (DSM) at an a priori level using DNS data for forced homogeneous turbulence with and without system rotation. Based on the results of the a priori analysis, a new model, termed as the non-equilibrium EASSM is introduced, which does not require the assumption that $\mathcal{P}/\epsilon = 1$. The framework of EASSM demands the determination of the SGS kinetic energy and the time-scale in order to close the system of equation. While [Marstorp et al. \(2009\)](#) use algebraic expressions for determining these additional variables, for the non-equilibrium EASSM, avoiding the assumption that $\mathcal{P}/\epsilon = 1$ enables the use of an evolution equation for the SGS kinetic energy. For the time-scale, an algebraic expression is derived as a function of SGS kinetic energy and dissipation. The performance of the non-equilibrium EASSM in comparison with the DSM and the EASSM of [Marstorp et al. \(2009\)](#) is evaluated by conducting LES of forced and decaying homogeneous turbulence, with and without rotation, using the finite volume code-INCA. For forced cases, the non-equilibrium model outperforms other models in terms of mean resolved and SGS kinetic energy predictions, and also gives a good match for the time averaged resolved spectrum with DNS. In the presence of strong rotation, however, all the models fail to capture the right decay rate as observed in DNS. On examining the DNS data for the two decaying cases, it appears that the isotropic scaling used for the modelling SGS kinetic energy dissipation in the non-equilibrium model deteriorates the model performance making it unable to provide the right level of inhibition in the decay of the resolved kinetic energy and dissipation.

Table of Contents

Acknowledgement	v
Abstract	vii
List of Figures	xiii
List of Tables	xvii
Nomenclature	xix
1 Introduction	1
1.1 Subgrid stress modelling in large eddy simulations	2
1.1.1 Linear eddy viscosity models	2
1.1.2 Non-linear explicit algebraic subgrid-scale stress models	3
1.2 Turbulence under system rotation	4
1.2.1 Characteristic features of turbulence under rotation	5
1.2.2 Large eddy simulations on rotating flows	5
1.3 Outline of the thesis	6
2 Theoretical Background	9
2.1 Filtering: a convolution	9
2.2 The evolution of subgrid scale stresses	11

2.3	Weak equilibrium assumption	12
2.4	Components of the 'simplified' subgrid scale stress equation	14
2.4.1	Modelling of the pressure-strain term	14
2.4.2	Modelling of the dissipation term	17
2.5	Formulation of an explicit model	17
2.5.1	Smagorinsky model	18
2.5.2	Explicit algebraic subgrid-scale stress model by Marstorp et al. (2009)	21
2.5.3	Formulation of an equation for the evolution of subgrid-scale kinetic energy	21
2.6	Modifications required to account for the Coriolis force	23
2.6.1	Changes to the governing equations	23
2.6.2	Some important parameters that characterise rotation	24
2.7	Closing remarks	25
3	Methodology	27
3.1	DNS code: TurBo	27
3.2	LES code: INCA	27
3.3	Forcing scheme	28
4	A Priori Tests	31
4.1	Case description	31
4.2	Results from direct numerical simulation	32
4.3	Tools for a priori analysis	35
4.4	Performance of the linear and the non-linear models for SGS stresses	36
4.5	Modelling of the pressure-strain term	40
4.6	Modelling of the subgrid-scale kinetic energy equation	45
4.6.1	Gradient diffusion hypothesis	45
4.6.2	Modelling of the subgrid-scale kinetic energy dissipation	46

4.7	Perfect equilibrium between the subgrid-scale kinetic energy production and dissipation	47
5	Formulation of an alternative modelling approach for explicit algebraic subgrid-scale stress model	49
5.1	Formulation of an explicit expression for subgrid-scale stress with an additional scalar unknown	49
5.2	Additional closures	54
6	A Posteriori Tests	57
6.1	Test cases	57
6.2	Forced isotropic turbulence	58
6.2.1	Resolved quantities	58
6.2.2	Resolved spectrum	62
6.2.3	Subgrid-scale quantities	63
6.3	Isotropic decaying turbulence	64
6.3.1	Resolved quantities	64
6.3.2	Subgrid-scale quantities	66
6.4	Homogeneously decaying rotating turbulence	68
6.4.1	Resolved quantities	68
6.4.2	Subgrid-scale quantities	71
6.5	Special attention to subgrid-scale evolution in homogeneously decaying rotating turbulence	73
6.5.1	Alternative scaling for SGS kinetic energy dissipation	76
7	Conclusions And Recommendations	79
7.1	Conclusions	79
7.1.1	A priori studies	79
7.1.2	A new formulation of explicitly algebraic subgrid-scale stress model	80
7.1.3	A posteriori studies	81
7.1.4	Behaviour of SGS in decaying turbulence with and without rotation	82

7.2 Recommendations	82
Bibliography	85
A Derivation of the transport equations for subgrid stress	91
B Derivation of the explicit algebraic stress model by Marstorp et al.	95
C Implementation of models into INCA	101
C.1 Computing scalars	102
C.2 Computing the non-linear term: the second tensor	103
C.2.1 Diagonal component	103
C.2.2 Off-diagonal component	104
D A short note on inertial waves in rotating turbulence	109

List of Figures

2.1	An example of a one-dimensional signal in space that is explicitly filtered.	10
4.1	Results from direct numerical simulation of forced homogeneous turbulence. Evolution of mean (a) turbulent kinetic energy non-dimensionalised with the value at steady-state and (b) dissipation non-dimensionalised with the power input due to external forcing, plotted against time non-dimensionalised with the forcing time scale.	33
4.2	Time averaged 1-D spectrum for the (a) DF and (b) DFRs.	34
4.3	Compensated turbulent energy spectrum obtained for DF, DFRw, and DFRs compensated with (a) $\kappa^{5/3}$ and (b) κ^2	34
4.4	Correlation coefficients for the normal and cross terms of the modelled and the actual SGS stress for EASSMs and anisotropy for DSM.	37
4.5	Probability density function f of the actual and modelled SGS kinetic energy production.	39
4.6	Correlation coefficients of the modelled and the actual pressure-strain for the LRR and SSG models obtained for the (a) DF, (b) DFRs, (c) and DFRw.	40
4.7	Correlation coefficients of the models for (a) rapid and (b) slow pressure-strain terms for the cases DF, DFRs.	44
4.8	Probability density function: f of the ratio of SGS kinetic energy production to dissipation for the three cases	48
6.1	Evolution of (left) mean resolved kinetic energy, non-dimensionalised with the steady-state value and (right) dissipation, non-dimensionalised with the power input due to external forcing, for forced isotropic case obtained DNS using different SGS model in LES plotted alongside the corresponding filtered DNS datapoints.	59
6.2	Evolution of the mean resolved kinetic energy for forced isotropic case in the neighbourhood of the peak value plotted alongside filtered DNS interpolated to obtain an estimate of the peak value.	60

6.3	Time averaged resolved spectrum for the forced isotropic case obtained for LES and filtered DNS. (a) $N = 32^3$, (b) 40^3 , and (c) 64^3	62
6.4	Evolution of mean subgrid-scale kinetic energy for forced isotropic case obtained for LES and filtered DNS. (a) $N = 32^3$, (b) 40^3 , and (c) 64^3	63
6.5	Evolution of (left) mean resolved kinetic energy, and (right) dissipation, non-dimensionalised with the corresponding initial value for decaying isotropic case obtained using different SGS model in LES plotted alongside the corresponding filtered DNS datapoints.	65
6.6	Isotropic decay of mean subgrid-scale kinetic energy obtained for LES and filtered DNS. (a) $N = 32^3$, (b) 40^3 , and (c) 64^3	67
6.7	The decay of resolved kinetic energy dissipation, SGS kinetic energy and production for LES with non-equilibrium EASSM on grid $32 \times 32 \times 32$	68
6.8	The evolution of the (a) mean resolved kinetic energy and (b) dissipation for the case of decaying turbulence under strong system rotation predicted by the differences SGS models with and without modifications. The LES are performed on a grid with $N = 32^3$	69
6.9	Evolution of (left) mean resolved kinetic energy, and (right) dissipation, non-dimensionalised with the corresponding initial value for decaying case under strong rotation, obtained using different SGS model in LES plotted alongside the corresponding filtered DNS datapoints.	70
6.10	The evolution of the mean SGS kinetic energy for EASSMs for the case of turbulence decaying with strong system rotation predicted by the different SGS models with and without any modifications. The LES are performed on a grid with $N = 32^3$	71
6.11	Decay of mean subgrid-scale kinetic energy under strong rotation obtained for LES and filtered DNS. (a) $N = 32^3$, (b) 40^3 , and (c) 64^3	72
6.12	The evolution of the (a) mean SGS kinetic energy and (b) dissipation for the case of turbulence decaying with and without strong system rotation obtained from filtering DNS using a spectral cut-off filter with $\kappa_c = 16$	74
6.13	The evolution of the (a) mean SGS kinetic energy production and (b) decay rate for decaying turbulence with and without strong system rotation obtained from filtering DNS using a spectral cut-off filter with $\kappa_c = 16$	75
6.14	The evolution of the mean forward (resolved to SGS) and backward (SGS to resolved scales) transfer of kinetic energy for decaying turbulence with and without strong system rotation obtained from filtering DNS using a spectral cut-off filter with $\kappa_c = 16$	75
6.15	The evolution of the Zeman wavenumber and the wavenumber corresponding the Kolomogorov length scale in decaying turbulence with rotation, computed from DNS.	76

C.1	The configuration of a staggered mesh showing the discretisation of actual velocity along with the interpolated velocity.	101
C.2	Location of the tensor elements on the computational mesh.	102
C.3	(a) Discretisation of the tensor elements in the non-linear term required for τ_{11} when the index $k = 2$ and (b) the corresponding nodes of the current and the neighbouring cells on the shaded x_1x_2- plane shown in (a). The cells to the west, south-west and south are shaded in grey.	104
C.4	(a) Discretisation of the tensor elements in the non-linear term required for τ_{11} when the index $k = 3$ and (b) the corresponding nodes of the current and the neighbouring cells on the shaded x_1x_3- plane shown in (a). The cells to the west, behind-west and behind are shaded in grey.	105
C.5	(a) Discretisation of the tensor elements in the non-linear term required for τ_{12} when the index $k = 1$ and (b) the corresponding nodes of the current and the neighbouring cells on the shaded x_1x_2- plane in (a). The cells to the north, north-east and east are shaded in grey.	106
C.6	(a) Discretisation of the tensor elements in the non-linear term required for τ_{12} when the index $k = 3$; (b) the cells required for interpolating the the tensor components to the black node shown in (a); (c) the cells required for interpolating the non-linear term at the black node onto the grey node where τ_{12} is evaluated.	107

List of Tables

2.1	Functions for one-dimensional box and spectral cut-off filters in physical and wavenumber spaces	10
2.2	Tensorial bases functions for the solution space of a_{ij} in the ‘simplified’ subgrid-scale stress equation shown in matrix form	18
2.3	Dynamic and non-dynamic formulations for the subgrid-scale kinetic energy and time scale in the explicit algebraic subgrid-scale stress model of Marstorp et. al. .	22
4.1	Setup of direct numerical simulations conducted for a priori studies.	32
4.2	Coefficients of the measured correlation between modelled and actual SGS kinetic energy and production for DSM, non-dynamic, and dynamic EASSMs for cases DF, DFRw, and DFRs.	38
4.3	Skewness of the modelled and the actual SGS kinetic energy production and normal SGS stresses for DSM, non-dynamic, and dynamic EASSMs for cases DF, DFRw, and DFRs.	38
4.4	Correlation coefficients for the modelled and the actual tensor elements of the divergence of turbulent kinetic energy transport tensor, and correlation between convective and pressure transport for forced turbulence with and without system rotation (DF, DFRw, and DFRs).	45
4.5	Variance and flatness for the divergence of modelled and actual transport quantities for the three cases.	46
4.6	Correlation coefficients, variance, and flatness for the modelled and the actual subgrid-scale kinetic energy dissipation for the three cases: DF, DFRw, and DFRs.	47
6.1	Time averaged steady-state values of the mean resolved kinetic energy and dissipation obtained for the forced isotropic turbulence using different SGS models and mesh sizes along with the corresponding values from DNS.	61
6.2	A few suggestions for different scaling laws that could be applicable to rotating homogeneous turbulence for modelling the SGS kinetic energy dissipation.	77
B.1	Expressions for C_1 in the model of Marstorp et al. (2009).	99

Nomenclature

Acronyms

NS	Navier-Stokes
DNS	Direct Numerical Simulation
RANS	Reynolds Averaged Navier-Stokes
LES	Large Eddy Simulation
SGS	Subgrid-Scale
EASSM	Explicit Algebraic Subgrid-Scale Stress Model
DSM	Dynamic Smagorinsky Model
LRR	Launder, Reece, and Rodi
IP	Isotropisation of Production
QI	Quasi-Isotropic
SSG	Speziale, Sarkar, and Gatski
PDF	Probability Density Function
CFL	Courant-Friedrichs-Lewy

Greek symbols

ε	SGS kinetic energy dissipation
Δ	Filter size in physical space/ LES grid size
κ_c	Filter size in Fourier space
κ	Wavenumber
ρ	Density
ν	Kinematic viscosity
$\chi(\cdot)$	Generalised central moment
τ_{ij}	SGS stress tensor
τ_{ij}^d	SGS stress anisotropy tensor
δ_{ij}	Kronecker delta
Π_{ij}	Pressure-strain tensor
$\Pi_{ij}^{(r)}$	Rapid pressure-strain tensor
$\Pi_{ij}^{(s)}$	Slow pressure-strain tensor

ε_{ij}	Dissipation tensor
Ω_{ij}	Rotation rate tensor
ν_T	Eddy viscosity
ν_k	Artificial viscosity in the model for transport term in SGS kinetic energy equation
ϵ_{ijk}	Levi-Civita symbol
Ω_i^s	System rotation rate vector
κ_Ω	Zeman wavenumber
κ_f	Forced mode
κ_\perp	Resultant wavenumber perpendicular to system rotation vector : $(\kappa_x^2 + \kappa_y^2)^{0.5}$
κ_\parallel	Wavenumber parallel to system rotation vector : $(\kappa_z^2)^{0.5}$
$\hat{\rho}$	Correlation coefficient
τ^*	Timescale in the EASSM model = k_{sgs}/ε
η	Scalar quantity in non-equilibrium EASSM = $\mathcal{P}/\varepsilon - 1 + C_1$
ε^r	Resolved turbulent kinetic energy dissipation
τ_L	Large eddy turnover time computed from DNS
κ_η	Wavenumber corresponding to Kolmogorov length scale

Latin symbols

\mathcal{P}	SGS kinetic energy production
k_{sgs}	SGS kinetic energy
\mathcal{F}	Filter function
H	Heaviside function
u_i	Velocity vector
p	Pressure
F_i	External forcing velocity
$\langle D \rangle / Dt$	Material derivative
a_{ij}	Normalised SGS stress anisotropy tensor
\mathcal{T}_{ijk}	SGS stress transport quantity
\mathcal{P}_{ij}	Production tensor
C_R	Rotta's constant
C_1, C_2	Constant in pressure-strain model
S_{ij}	Strain rate tensor
U	Velocity scale
L	Length scale
C_S	Smagorinsky constant
C_K	Kolmogorov constant
C_d	Dynamic constant in Smagorinsky model
$G^{(n)}$	Coefficients of generalised tensor for a_{ij}
$T_{ij}^{(m)}$	Generalised tensor for a_{ij}
C_c	Constant in the model for ε
C_{ij}^f	Coriolis force
C_{ij}^r	Coriolis term in the SGS stress evolution equation

Ro	Rossby number
A_{ran}, B_{ran}	External force coefficients
F_{sph}	Force spectrum
\mathcal{P}_f	Power input due to external force
Re_f	Reynolds number based on forcing parameters
Ro_f	Rossby number based on forcing parameters
$e1_i, e2_i$	Basis vectors of external force
A_f	Amplitude of force at $\kappa = \kappa_f$
c_f	Forcing input parameter to determine the degree of concentration of forcing
\hat{E}	Energy spectrum
f	PDF
p^r	Rapid pressure term
p^s	Slow pressure term
K^r	Resolved turbulent kinetic energy
\mathcal{P}^+	Kinetic energy transfer from resolved to SGS
\mathcal{P}^-	Kinetic energy transfer from SGS to resolved

Chapter 1

Introduction

Turbulence still remains one of the unsolved mysteries of classical physics. The existence of smooth, bounded solutions to the Navier-Stokes (NS) equations, that represent the motion of fluids, is yet to be verified and is stated as one of the ‘Millennium Prize Problems’. Fortunately, instead of addressing the million dollar question, computers can be utilized to find numerical solutions to the NS equations. This approach of solving for the complete solution of the NS equations is called Direct Numerical Simulation (DNS) and requires immense computational power for practical application to engineering flows. An alternative is to split the flow variables, i.e. velocity and pressure, into mean and fluctuating components. The resulting equations for the mean quantities are called as the Reynolds Averaged NS (RANS) equations, which can be solved numerically at relatively lower cost. These equations contain a second order tensor called the Reynolds stress, that requires additional relations in order to close the system of equations. There are numerous techniques available to model the Reynolds stresses. However, the modelling approximations and the general framework of RANS simulations limit its applicability to simple flow situations (predominantly statistically stationary scenarios). Another alternative to DNS is to resolve a majority of the turbulent energy spectrum, and limit the extent of modelling to the small scales. When compared to RANS, this approach is expected to improve the accuracy of the solution (if the small scales are modelled appropriately) while also providing a framework for application to unsteady flow scenarios. Large Eddy Simulations (LES) work based on this principle. The resulting set of equations contain a non-linear term, analogous to the Reynolds stress, called as the subgrid-scale (SGS) stress that needs to be modelled. Simplistic eddy viscosity models for the SGS stress that are formulated based on the Boussinesq hypothesis are still widely used for closure.

LES are gaining popularity in the characterisation of complex flows. While the computational requirements still limit its use in industrial applications, it serves as a helpful tool in studying the behaviour of flows. Acoustic studies and unsteady cavitation are some examples where LES has proven to be a useful tool ([Manoha et al. \(2000\)](#), [Asnaghi \(2015\)](#), [Lu et al. \(2010\)](#)). The computational demand of LES can be directly attributed to the number of scales that are

to be resolved. The mesh used to discretise the computational domain should be sufficiently refined to capture the large scales of motion, so that the unresolved SGS can be modelled. While many linear models in LES provide a good estimate of the behaviour of SGS stress for isotropic or even wall bounded flows, these fail in the presence of strong system rotation. Rotation introduces a Coriolis force which alters the dynamics of turbulence drastically and brings forth complex features, some of which are the inverse energy cascade, the suppressed levels of SGS production and dissipation, and the anisotropy of SGS scales, which are not accurately captured by linear eddy viscosity models (Lu et al. (2007)). Therefore, a model that is capable of improving the representation of the SGS stresses in flows with strong rotation can have large practical applications in the study of flow inside turbines, planetary flows, and formation of cyclones, for example. Explicit Algebraic Subgrid-scale Stress Models (EASSM), also referred to as non-linear or mixed models, have shown some potential to be applied in these scenarios. Since EASSMs are derived by simplifying the equation for evolution of SGS stress, they provide a more physical description of the flow than linear models. In this thesis, the deficiencies of the present formulations of EASSMs, and a systematic approach to deriving a new EASSM for homogeneous flow (including rotating flows¹) will be elaborated.

1.1 Subgrid stress modelling in large eddy simulations

The main governing equations in LES, upon solving will give the filtered solution, i.e. filtered velocity and pressure (for an incompressible case). Filtering is merely an operation performed to limit the number of scales that will be used to construct the solution. However, a result of the filtering operation is the inclusion of SGS stress in the NS equations which couples the resolved and the SGS. In order to get the correct representation of the resolved quantities, the effect of this non-linear coupling must be modelled in the ‘right way’. Numerous techniques are available to compute the unknown SGS stress using the known resolved quantities. The closure models used in LES can be broadly categorised into linear and non-linear models. As a complete review of all the linear and the non-linear models in LES is far beyond the present scope of work, in the current section, an overview of the models employed in this thesis is provided.

1.1.1 Linear eddy viscosity models

Linear closure models work based on the eddy viscosity hypothesis and are common in LES. The first model that was proposed for LES is the computationally simple Smagorinsky model (Smagorinsky (1963)). The model works based on an implied alignment between the SGS stress tensor and the resolved strain rate tensor. To complete the relation, an eddy viscosity is formulated using the local mesh dimension as a length scale and a time scale obtained from the resolved strain rate. The eddy viscosity, when formulated in this way is strictly positive, which makes the model purely dissipative, thereby improving its numerical stability.

¹Rotating flows in this thesis implies flows that are subject to solid body rotation. Not to be confused with rotational flows which indicates that $\nabla \times \vec{u} \neq 0$.

However, the presence of a predetermined constant, i.e. Smagorinsky constant, makes the model unable to suitably adapt the level of dissipation in an inhomogeneous direction or in the presence of laminar regions in the flow. [Germano et al. \(1991\)](#) suggested an improvement by introducing a dynamic approach that is capable of adjusting the eddy viscosity locally. This version of the Smagorinsky model came to be known as the Dynamic Smagorinsky Model (DSM). The main advantage of DSM is that it does not require any additional wall damping to obtain the right near wall behaviour. [Piomelli \(1993\)](#) presented a good agreement between the results of LES using DSM and experimental values for the first and the second moments of velocity. The success of the dynamic procedure is also documented in the works of [Akselvoll and Moin \(1996\)](#), and [Ghosal and Rogers \(1997\)](#). While dynamic determination of the constant drastically improves the performance of Smagorinsky model, especially in wall bounded flows, the linearity of the formulation still poses as a strong limitation. The assumed alignment between SGS stress tensor does not seem to hold even for the simple case of isotropic turbulence ([Horiuti \(2003\)](#), [Tao et al. \(2000\)](#)).

1.1.2 Non-linear explicit algebraic subgrid-scale stress models

Formulating a model with a higher level of closure can be obtained by solving the complete SGS stress evolution equations. This is a set of six independent partial differential equations where the transport, the pressure-strain, and the dissipation terms will need to be further modelled. Numerically solving these additional equations to determine the SGS stresses is computationally highly demanding. Therefore, a way to simplify these equations to an algebraic form, while still representing most of the relevant physics of SGS stress evolution will prove to be beneficial. Such a simplification exists in RANS for expressing the Reynolds stress and it is called as the ‘weak equilibrium assumption’, which was proposed by [Rodi \(1972\)](#). Fortunately, SGS stress in LES and Reynolds stress in RANS share similarities in their formulation (as do the governing equations in LES and RANS) ([Germano \(1992\)](#)). Owing to this similarity, many approaches for modelling Reynolds stress in RANS have been borrowed and adapted to model SGS stress in LES.

The formulation of an explicit expression for the normalised SGS stress anisotropy was first introduced by [Pope \(1975\)](#) by making use of the Caley-Hamilton theorem. The normalised Reynolds stress anisotropy was expressed in terms of ten independent tensorial bases that are functions of the resolved strain rate and the rotation rate tensors. The mathematical complexity of the formulation limited [Pope \(1975\)](#) to derive semi-explicit expressions only for two dimensional flows. The final expression was semi-explicit, because the solution to the equations was dependent on the ratio of turbulent kinetic energy production to dissipation. Since this ratio is in-turn a function of normalised Reynolds stress anisotropy, the resulting system of equations were non-linear. Based on the strategy adopted to solve the resulting non-linear equation, various formulations are possible ([Taulbee \(1992\)](#), [Gatski and Speziale \(1993\)](#), [Girimaji \(1996\)](#), [Wallin \(2000\)](#), [Sjögren and Johansson \(2000\)](#), [Wallin and Johansson \(2000\)](#)). Using computational tools, [Taulbee \(1992\)](#), and [Gatski and Speziale \(1993\)](#) extended the algebraic formulation of [Pope \(1975\)](#) to three dimensional flows. The main difference between the modelling approaches of [Taulbee \(1992\)](#), and [Gatski and Speziale \(1993\)](#) is that the model proposed by the former retained the ratio of turbulent kinetic energy production to dissipation

implicitly, while the latter involved pre-calibration of this ratio to equilibrium values, thereby avoiding the need for an iterative procedure to solve the model equations. Although, the model of Gatski and Speziale (1993) gave poor predictions, giving wrong asymptotic values for flows subject to rapid distortions. Wallin and Johansson (2000), and Girimaji (1996) suggested an alternative formulation for two dimensional flows by providing an explicit third order polynomial for the ratio of turbulent kinetic energy production to dissipation. Wallin and Johansson (2000) also extended this approach to three dimensional flows with a sixth order equation for this ratio.

The first extension of this modelling framework to LES was done by Marstorp et al. (2009). The resulting expression for normalised SGS stress anisotropy, after applying the weak equilibrium assumption would contain the ratio of SGS kinetic energy production to dissipation, i.e. \mathcal{P}/ϵ . This ratio poses as a non-linearity in the same way that the ratio of kinetic energy production to dissipation makes the expression non-linear for RANS. However, by assuming that the SGS kinetic energy production and the dissipation are in perfect balance, i.e. $\mathcal{P}/\epsilon = 1$, Marstorp et al. (2009) removed the non-linearity in the equations. An isotropic model and a modified version of the model from Launder et al. (1975) were used to model the dissipation and the pressure-strain terms respectively. By using the tensorial bases for two dimensional mean flows (Pope (1975)), the final expression was derived. An extension of this model to rotating flows was also done by modifying the rotation rate tensor in a such a way to account for the inclusion of the Coriolis term to the SGS evolution equation. Separate algebraic expressions were formulated for SGS kinetic energy and time scale (k_{sgs}/ϵ). Two versions - a dynamic and a non-dynamic version of the model were formulated. The resulting dynamic and non-dynamic EASSMs, when applied to turbulent channel flow showed an improved description of SGS anisotropy compared to DSM especially at coarser grid resolutions. Also, the DSM was found to over-predict the near wall peak in SGS kinetic energy while the dynamic EASSM showed a closer resemblance to DNS data. In a recent work, Montecchia et al. (2017) used the dynamic formulation of Marstorp et al. (2009) for high Reynolds number turbulent channel flow and reported similar results. The model gave superior prediction for the mean velocity profiles when compared to DSM.

1.2 Turbulence under system rotation

Linear eddy viscosity models for turbulence in LES perform well when the subgrid scales, which are predominantly dissipative in nature, maintain an isotropic state. When an initially isotropic state of turbulence suddenly comes under the influence of system rotation, the characteristics of turbulence thus far change drastically. The ensuing features of these rotating flows and the performance of some of the current SGS models under weak and strong rotation make an interesting case for further investigation.

1.2.1 Characteristic features of turbulence under rotation

Rotation brings Coriolis and centrifugal force terms into the NS equations. While the centrifugal contribution modifies the pressure term, the Coriolis force has an interesting effect on the turbulent dynamics. Under strong rotation, the isotropy of the subgrid-scales is significantly disrupted. Coriolis forces shape the seemingly random and chaotic turbulence in a specific manner characterized by formation of coherent columnar structures in the flow. Though rotation does not directly add or remove energy from the system (Davidson (2004)), it influences the evolution of the quantities in the (both resolved and SGS) kinetic energy equation. Early experimental analysis by Traugott (1958) concluded that the process of turbulence intensity decay took place much slower for flows in the presence of system rotation than without rotation. With the advent of DNS, the evolution of NS equations when subject to rotation have been better scrutinized. Results from numerical simulations of Bardina et al. (1985) showed that, in the case of homogeneous turbulence under system rotation, the dissipation of turbulent kinetic energy becomes suppressed and the turbulent structures parallel to the axis of rotation become elongated. McEwan (1976) also observed the formation of columnar structures that aligned themselves to the axis of rotation in his experiments. Moreover, these intense vortices always seemed to favor the cyclonic² orientation than anticyclonic. This cyclone-anticyclone asymmetry has also been further investigated and confirmed by Hopfinger et al. (1982), Morize et al. (2005), Staplehurst et al. (2008), and Naso (2015). Another interesting feature that is brought about by system rotation is a modified energy scaling with wavenumber in the inertial range caused due to an increased amount of backscatter, i.e. energy transfer from small to large scales. When turbulence was subject to system rotation and forced using a random three-dimensional forcing, Smith et al. (1996) observed a κ^{-3} scaling of the kinetic energy spectrum for wavenumbers that are smaller than the forcing wavenumber. This was reported to be caused by an increased amount of backscatter, which was also confirmed by Smith and Waleffe (1999). A detailed account of the features discussed so far and the current state of the art (both experimental and numerical investigations) of turbulence under system rotation can be found in the review done by Godefert and Moisy (2015). In conclusion, the evolution of both the resolved and the SGS of turbulence under solid body rotation is highly altered compared to a non-rotating case. Therefore the SGS models for LES when applied to rotating flows must be capable of predicting the (altered) dynamics of the SGS such that their influence on the resolved scales can be correctly accounted.

1.2.2 Large eddy simulations on rotating flows

The performances of SGS models for rotating flows in LES have been documented for over three decades now. Early work of Speziale (1985) covered the theoretical constraints such as Galilean invariance³ and material-frame indifference⁴, that an SGS model is expected to fulfill. Standard eddy viscosity models were analysed and a modified linear combination model

²‘Cyclonic’ corresponds to when $\vec{\omega} \cdot \vec{\Omega}^s > 0$, where $\vec{\omega}$ and $\vec{\Omega}^s$ denote the vorticity and system rotation vector, respectively.

³Property of SGS stresses to be unaffected under a Galilean transformation.

⁴Property of SGS force that makes the divergence of the SGS stresses indifferent to the frame of reference.

(Bardina et al. (1983)) was recommended for rotating turbulent flows. The constraint of material-frame indifference was further analysed by means of a priori tests by Lu et al. (2007). An improved performance was reported when a transport equation for SGS kinetic energy (Yoshizawa and Horiuti (1985)) was solved to compute eddy viscosity when compared with the original Smagorinsky model. New one-equation models (non viscosity models) were also proposed by Lu et al. (2007) which satisfy material-frame indifference, which recorded significantly higher levels of correlation for SGS stresses than standard and dynamic Smagorinsky models. Kobayashi and Shimomura (2001) examined dynamic models - DSM, dynamic mixed model (Zang et al. (1993), Vreman et al. (1994)), dynamic Clark model (Clark et al. (1979), Vreman et al. (1996)), and dynamic two-parameter Clark model (Shimomura (1999)) in the context of rotating homogeneous turbulence. A reformulation of the DSM model was also introduced for rotating flows and it was reported that the reformulated DSM gave unphysical fluctuations during decay. Furthermore, all SGS models that were employed seemed to dissipate excessively when compared with results from DNS.

The case of rotating turbulent channel flows is a challenging case for study, as there are distinct regions of stabilized and destabilized flow found at the suction side⁵ and pressure side of the channel, respectively (Kristoffersen and Andersson (1993)). Therefore the SGS model that is employed is required to suitably adapt the level of dissipation in these regions in addition to incorporating the effects of Coriolis force on the turbulence characteristics. Though rotating channel flows is outside the main focus of this thesis, it is still worth taking a moment to discuss the performance of different SGS models for this case. Oberlack et al. (2006) studied the performance of DSM for channel flow under streamwise rotation and compared the values with DNS. DSM seemed to capture most of the dynamics at high rotation rates, however, it failed to predict the linear regions of the mean velocity in the streamwise direction. Furthermore, the normal stresses, especially in the streamwise direction gave poor agreement with DNS results. Marstorp et al. (2009) performed LES on spanwise rotating channel flows using EASSM (accounting for system rotation). The model was able to capture the stable regions in the flow, but the re-laminarisation was found to be delayed towards higher Reynolds number. The dynamic EASSM required reduced computational effort compared to DSM due to the lesser number of test filtering operations (for dynamic procedure). An attractive feature of the EASSMs formulated by Marstorp et al. (2009) is the inclusion of the system rotation rate into their formulation. This inclusion immediately lowers the tensor coefficients in the formulation, consequently lowering the amount of SGS production. However, since the SGS production is modelled in a strictly positive manner, the model cannot account for any backscatter. Nevertheless, lowering the SGS production aid in lowering the amount of forward energy cascade. This aspect of EASSMs fuelled the curiosity to further examine their application to homogeneous turbulence under system rotation.

1.3 Outline of the thesis

This report contains details of tests performed on rotating and non-rotating homogeneous turbulence. The necessary theoretical background for this work is covered in Ch. 2, where

⁵The side of the channel that is characterized by a low static pressure.

the modelling framework and the models that will be employed for the different cases will be explained. The simulations (DNS and LES) are run using different codes which will be introduced in Ch. 3. Chapter 3 will also cover the details of the forcing scheme that will be employed. The results of this work are divided into a priori and a posteriori results. A priori studies (covered in Ch. 4) involves entirely the use of DNS data to test the performance of different modelling approaches. Once this is established, a new modelling approaches for EASSM is introduced in Ch. 5 and the performance of the new model is tested by conducting actual (a posteriori) LES. The results of the new formulation in comparison of other SGS models will be covered in Ch. 6. Finally, the conclusions from the current work and the recommendations for any future work will be provided in Ch. 7.

Chapter 2

Theoretical Background

Building an EASSM in LES can be described as a four step process. First step involves simplifying the SGS stress evolution equations to a ‘simplified’ algebraic form by invoking the weak equilibrium assumption. The second step is the appropriate modelling of the remaining terms in the ‘simplified’ equation. The third step involves the selection of bases tensors (Pope (1975)) that will be used in the final (model) expression. The final step is the determination of the required (additional) SGS quantities, for instance, the SGS kinetic energy and dissipation, in order to close the system of equations. However straightforward as these steps might seem, the selection at each step is rather tedious. Starting from the general equations for the evolution of the SGS stresses, the different terminologies and the theoretical background necessary for understanding the execution of each of these steps will be covered in this chapter.

2.1 Filtering: a convolution

LES work by decomposing the solution field into resolved and unresolved components. This decomposition can be achieved with the use of filters. Filtering can be understood as a smoothing operation that dampens the fluctuations due to large wavenumbers. As a consequence, the resulting filtered LES solution can be represented on a coarser grid than DNS. In physical space, filtering is defined as a convolution of the complete solution field with the filter function. For a one dimensional signal, say $u(x)$, the convolution is expressed as

$$\langle u(x) \rangle = \int_{-\infty}^{\infty} \mathcal{F}(r)u(x-r)dr, \quad (2.1)$$

where $\mathcal{F}(r)$ is the filter function and $\langle u(x) \rangle$ is the filtered signal (Pope (2001)). There are many different types of filters that are available to perform this convolution. In this section, two of the commonly used filters for LES: the box, and the spectral cut-off filter, will be described in brief. For the sake of simplicity, we shall restrict the filter definitions to one

Filter	Physical space	Wavenumber space
Box	$\frac{1}{\Delta} H\left(\frac{\Delta}{2} - \ r\ \right)$	$\frac{\sin(\kappa\pi/2)}{\kappa\pi/2}$
Spectral cut-off	$\frac{\sin(\pi r/\Delta)}{\pi r}$	$H\left(\frac{\pi}{\Delta} - \ \kappa\ \right)$

Table 2.1: Functions for box and spectral cut-off filters in physical and wavenumber spaces (Pope (2001)). H is the Heaviside function-the integral of the Dirac delta function, i.e. $\int_{-\infty}^x \delta(x)dx$.

dimension. The extension to three dimensions can be done intuitively.

One way to smoothen or filter the solution field is to average the original field in the interval $(x - \frac{1}{2}\Delta, x + \frac{1}{2}\Delta)$ where Δ is the filter width. This form of filtering can be accomplished by the use of box filters. The corresponding filter functions in both physical and wavenumber spaces are shown in Tab. 2.1. Spectral cut-off filters are easier understood in wavenumber space. It simply removes the wavenumbers that are above a specified cut-off: $\kappa_c = \pi/\Delta$. The filter functions for spectral cut-off are also given in Tab. 2.1. The box filter operates locally only in physical space while spectral cut-off filter is local only in wavenumber space (Sagaut (2006)). Figure 2.1 shows the example of a one dimensional signal in space that is filtered using box and spectral cut-off filters with same Δ .

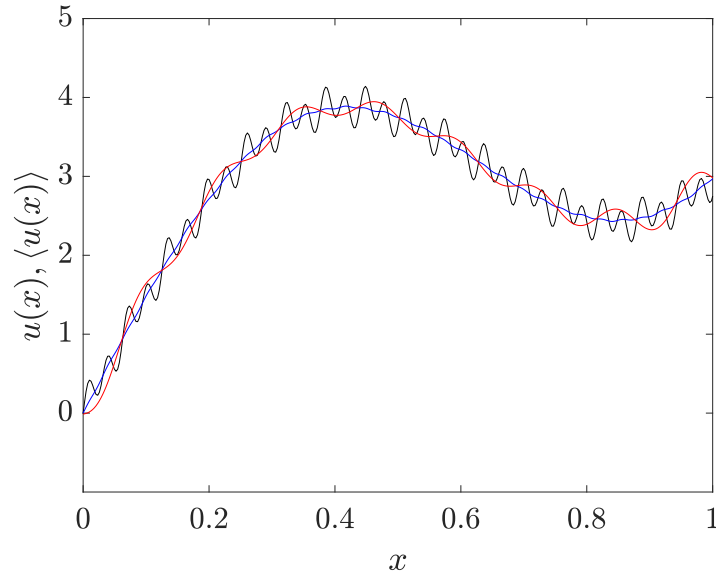


Figure 2.1: An example of a one-dimensional signal in space that is explicitly filtered. Black line - original signal, blue line - box filter, red line - spectral cut-off filter.

In reality however, filtering is not often done explicitly. In a finite volume approach, when the governing equations in LES are discretised on a computational grid, the size of the grid determines the filter width, i.e. Δ . This is equivalent to applying a box filter with a filter width that is equal to the grid size. Therefore, care has to be taken while performing LES to ensure that the grid is sufficiently refined such that (energy containing) large scales are effectively resolved. This is one of the reasons for the need for higher computational power in LES compared to RANS, especially for high Reynolds number wall bounded flows, while performing wall-resolved LES (Baggett et al. (1997), Fureby et al. (2004)).

2.2 The evolution of subgrid scale stresses

The NS equations are the starting point in deriving the equations for evolution of different resolved and subgrid-scale stresses (and kinetic energy). For incompressible flows $\left(\frac{\partial u_j}{\partial x_j} = 0\right)$ with constant viscosity, the NS equations under inertial frame of reference, in index notation read,

$$\frac{\partial u_i}{\partial t} + \frac{\partial u_i u_k}{\partial x_k} = -\frac{1}{\rho} \frac{\partial p}{\partial x_i} + \nu \frac{\partial^2 u_i}{\partial x_k \partial x_k} + F_i, \quad (2.2)$$

where, u_i , p are the (unfiltered) velocity and pressure, respectively. F_i is the external force. When $F_i = 0$, we can derive the evolution equations for the unfiltered stresses as

$$\frac{\partial u_i u_j}{\partial t} + \frac{\partial u_i u_j u_k}{\partial x_k} = -\left(\frac{u_i}{\rho} \frac{\partial p}{\partial x_j} + \frac{u_j}{\rho} \frac{\partial p}{\partial x_i}\right) + \nu \frac{\partial^2 u_i u_j}{\partial x_k \partial x_k} - 2\nu \frac{\partial u_i}{\partial x_k} \frac{\partial u_j}{\partial x_k}. \quad (2.3)$$

From Eq. (2.2) and (2.3) by means of filtering, the SGS stress evolution equations can be derived. This derivation is provided in App. A. For incompressible flows without any body forces, this equation under inertial reference frame is given in index notation as

$$\begin{aligned} \frac{\langle D \rangle \chi(u_i, u_j)}{Dt} + \frac{\partial}{\partial x_k} \left[\underbrace{\chi(u_i, u_j, u_k)}_{\text{turbulent transport}} + \underbrace{\frac{1}{\rho} \chi(p, u_j) \delta_{ik} + \frac{1}{\rho} \chi(p, u_i) \delta_{jk}}_{\text{pressure transport}} - \underbrace{\nu \frac{\partial \chi(u_i, u_j)}{\partial x_k}}_{\text{viscous diffusion}} \right] = \\ \underbrace{-\chi(u_j, u_k) \frac{\partial \langle u_i \rangle}{\partial x_k} - \chi(u_i, u_k) \frac{\partial \langle u_j \rangle}{\partial x_k}}_{\text{production}} + \underbrace{\chi\left(\frac{p}{\rho}, \frac{\partial u_j}{\partial x_i}\right) + \chi\left(\frac{p}{\rho}, \frac{\partial u_i}{\partial x_j}\right)}_{\text{pressure-strain}} - \underbrace{2\nu \chi\left(\frac{\partial u_i}{\partial x_k}, \frac{\partial u_j}{\partial x_k}\right)}_{\text{dissipation}}, \end{aligned} \quad (2.4)$$

where, $\chi(\cdot)$ is the generalized central moment, defined as

$$\chi(u_i, u_j) = \langle u_i u_j \rangle - \langle u_i \rangle \langle u_j \rangle, \quad (2.5)$$

$$\begin{aligned} \chi(u_i, u_j, u_k) = & \langle u_i u_j u_k \rangle - \langle u_i \rangle \chi(u_j, u_k) - \langle u_j \rangle \chi(u_k, u_i) - \langle u_k \rangle \chi(u_i, u_j) \\ & - \langle u_i \rangle \langle u_j \rangle \langle u_k \rangle. \end{aligned} \quad (2.6)$$

The symbol $\langle \cdot \rangle$ denotes a convolution operation and in the current context of LES represents filtering. The operator $\langle D \rangle(\cdot)/Dt = \partial(\cdot)/\partial t + \langle u_j \rangle \partial(\cdot)/\partial x_j$ is the material derivative. For the sake of convenience, some of the SGS quantities that will be encountered often in the thesis are defined below.

$$\text{SGS stress: } \tau_{ij} = \chi(u_i, u_j) = \langle u_i u_j \rangle - \langle u_i \rangle \langle u_j \rangle, \quad (2.7)$$

$$\text{SGS kinetic energy: } k_{sgs} = \frac{1}{2} \chi(u_i, u_i) = \frac{1}{2} (\langle u_i u_i \rangle - \langle u_i \rangle \langle u_i \rangle), \quad (2.8)$$

$$\text{anisotropy of SGS stress: } \tau_{ij}^d = \tau_{ij} - \frac{2}{3} k_{sgs} \delta_{ij}, \quad (2.9)$$

$$\text{normalised anisotropy SGS stress: } a_{ij} = \frac{\tau_{ij}^d}{k_{sgs}} = \frac{\tau_{ij}}{k_{sgs}} - \frac{2}{3} \delta_{ij}. \quad (2.10)$$

In order to ease the discussion in the following sections, the terms in Eq. (2.4) can be further written in a compact form. For this purpose, we shall introduce \mathcal{T}_{ijk} , \mathcal{P}_{ij} , Π_{ij} , and ε_{ij} , which we use to rewrite Eq. (2.4) as

$$\frac{\langle D \rangle \tau_{ij}}{Dt} + \frac{\partial \mathcal{T}_{ijk}}{\partial x_k} = \mathcal{P}_{ij} + \Pi_{ij} - \varepsilon_{ij}. \quad (2.11)$$

The different terms in Eq. (2.11) represent the functional equivalence of the terms in Eq. (2.4). \mathcal{T}_{ijk} denotes the transport quantities and is a collective of the turbulent, pressure, and viscous effects. \mathcal{P}_{ij} , Π_{ij} , and ε_{ij} represents the production, pressure-strain, and dissipation tensors, respectively. EASSMs are derived by reducing Eq. (2.4) using the ‘weak equilibrium’ assumption, followed by the modelling of the remaining terms. The weak equilibrium assumption and the formulation of explicit expression for SGS stress will be the subject of the subsequent discussions.

2.3 Weak equilibrium assumption

Application of the weak equilibrium assumption is vital for deriving an EASSM. Before defining the weak equilibrium assumption, the first term in Eq. (2.4) is rewritten by dividing and

multiplying the SGS stress by the SGS kinetic energy. This operation results in,

$$\begin{aligned}
\frac{\langle D \rangle \tau_{ij}}{Dt} &= \frac{\langle D \rangle}{Dt} \left(k_{sgs} \frac{\tau_{ij}}{k_{sgs}} \right) \\
&= \frac{\langle D \rangle}{Dt} \left(k_{sgs} \left(a_{ij} + \frac{2}{3} \delta_{ij} \right) \right) \\
&= k_{sgs} \frac{\langle D \rangle a_{ij}}{Dt} + \left(a_{ij} + \frac{2}{3} \delta_{ij} \right) \frac{\langle D \rangle k_{sgs}}{Dt} \\
&= k_{sgs} \frac{\langle D \rangle a_{ij}}{Dt} + \frac{\tau_{ij}}{k_{sgs}} \frac{\langle D \rangle k_{sgs}}{Dt}
\end{aligned} \tag{2.12}$$

A revelation of Kolomogorov's similarity hypotheses is the existence of an equilibrium range in the turbulent energy cascade where the small scales of motion maintain a state of equilibrium with the large scales, i.e. they quickly adapt to any changes in the large scales of motion. For sufficiently large Reynolds numbers, an inertial subrange is observed where energy is merely transferred from the large scales of motion to the small scales in the viscous region. Therefore, in the context of LES, when the cut-off wavenumber is placed in the inertial region, one can infer that the total production and dissipation of SGS kinetic energy are approximately in balance. The interpretation of this is that the subgrid-scales adjust quickly to match the dissipation to the production, i.e. $\mathcal{P} \approx \varepsilon$. However, a perfect (local) balance between SGS kinetic energy production and dissipation is not practical as turbulence is always evolving in time. Rodi (1972) assumed that the evolution of the SGS quantities due to imbalance in SGS production and dissipation can be captured in the transient behaviour of SGS kinetic energy while the normalised SGS anisotropy still maintains a state of quasi-equilibrium. The temporal and spatial variation of the normalised SGS stress anisotropy is assumed to be negligible compared to the corresponding variation in the SGS kinetic energy. This is called as the weak equilibrium assumption that was originally proposed by Rodi (1972). By applying this, Eq. (2.12) simplifies to

$$\frac{\langle D \rangle \tau_{ij}}{Dt} \approx \frac{\tau_{ij}}{k_{sgs}} \frac{\langle D \rangle k_{sgs}}{Dt}. \tag{2.13}$$

The transport equation for k_{sgs} (Eq. (2.14)) is formulated by simply evaluating half of the trace of Eq. (2.4), i.e.

$$\begin{aligned}
\frac{\langle D \rangle k_{sgs}}{Dt} + \frac{\partial}{\partial x_j} \left[\underbrace{\frac{1}{2} \chi(u_i, u_i, u_j)}_{\text{turbulent transport}} + \underbrace{\frac{1}{\rho} \chi(p, u_i)}_{\text{pressure transport}} - \underbrace{\frac{\nu}{2} \frac{\partial \chi(u_i, u_i)}{\partial x_j}}_{\text{viscous diffusion}} \right] = \\
\underbrace{-\chi(u_i, u_j) \frac{\partial \langle u_i \rangle}{\partial x_j}}_{\text{production}} - \underbrace{\nu \chi \left(\frac{\partial u_i}{\partial x_j}, \frac{\partial u_i}{\partial x_j} \right)}_{\text{dissipation}}.
\end{aligned} \tag{2.14}$$

A consequence of ignoring the spatial derivatives of τ_{ij}/k_{sgs} is that the transport terms in SGS evolution equation (Eq. (2.4)) can be modelled such that they scale with the transport

quantities in the SGS kinetic energy evolution equation times the SGS stress normalised by the SGS kinetic energy, i.e.

$$\frac{\partial \mathcal{T}_{ijk}^{mod}}{\partial x_k} = \frac{\tau_{ij}}{k_{sgs}} \frac{\partial \mathcal{T}_{mmk}}{\partial x_k}. \quad (2.15)$$

These simplifications result in a ‘simplified’ algebraic expression for the SGS stresses of the form:

$$\frac{\tau_{ij}}{k_{sgs}} (\mathcal{P} - \varepsilon) = \mathcal{P}_{ij} + \Pi_{ij} - \varepsilon_{ij}, \quad (2.16)$$

where \mathcal{P} and ε are $\mathcal{P}_{ii}/2$ and $\varepsilon_{ii}/2$, respectively. Equation (2.16) is an adaptation of the effect of weak equilibrium assumption to LES from RANS. The corresponding equation for RANS is the starting point for all the different formulations of algebraic Reynolds stress models. Similarly in LES, depending on the modelling of the different terms in Eq. (2.16) and the treatment of non-linearity (which will be covered in Sec. 2.5), different formulations can be obtained.

2.4 Components of the ‘simplified’ subgrid scale stress equation

Equation (2.16) is the ‘simplified’ equation for SGS stresses, for which explicit solutions are to be sought. The terms on the right hand side (RHS) of Eq. (2.16) are the production, the pressure-strain, and the dissipation terms, respectively. Among these, the production term is in the closed form as it is a function of the SGS stress and the resolved velocity gradients (see Eq. (2.4)). On the other hand, the pressure-strain and the dissipation terms require to be modelled. The role of pressure-strain term in the evolution of SGS stress is crucial. It plays the important role of redistributing energy between the different SGS stress components. It is interesting to note that this term, however, does not alter the total energy at the subgrid-scales. Therefore, it does not feature in the equation for k_{sgs} (see Eq. (2.14)) as the tensor is traceless, i.e. $\Pi_{ii} = 0$. Various linear and non-linear models are available for modelling the pressure-strain term. Three of the more commonly used models for pressure-strain term and the isotropic modelling of the dissipation term shall be discussed in detail in this section.

2.4.1 Modelling of the pressure-strain term

Any examination of the pressure-strain term must start from the Poisson equation for pressure. [Chou \(1945\)](#) formulated the Poisson equation for the residual pressure term. The solution for the residual pressure fluctuations has three parts: a rapid term, a slow term, and a harmonic term. The rapid and slow terms are so named based on their respective time scales. The contribution of these three parts of pressure will also be reflected in the pressure-strain term,

therefore Π_{ij} can be split into $\Pi_{ij}^{(r)}$, $\Pi_{ij}^{(s)}$, and $\Pi_{ij}^{(h)}$. However, the contribution to the pressure-strain term from the harmonic pressure fluctuation is often neglected in RANS, because, in the context of Reynolds stress budgets, this term plays a very minor role (Mansour et al. (1988)). Consequently, the final modelling of the pressure-strain term involves modelling of the rapid and slow parts only, i.e. $\Pi_{ij}^{(r)}$, and $\Pi_{ij}^{(s)}$. The relative importance of these two parts depends on the flow case that is under consideration.

When turbulence is allowed to decay from an anisotropic state, the initial anisotropy slowly disappears and the system tends towards an isotropic state (Uberoi (1957)). In the case of RANS, in the absence of mean flow, the process of return to isotropy is entirely dictated by the the slow term $\Pi_{ij}^{(s)}$. Rotta (1951) proposed a linear model for the slow term, i.e.

$$\Pi_{ij}^{(s)} = -C_R \varepsilon a_{ij}, \quad (2.17)$$

where C_R is called the Rotta constant. Although this model suggests that the return to isotropy is linear, this is not the case, as in reality, this process is highly non-linear¹ (Choi and Lumley (2001)). Lumley (1979) was the first to demonstrate the need for inclusion of non-linearity in the model for $\Pi_{ij}^{(s)}$, which inspired the formulation of models that captured the phenomenon of non-linear return to isotropy (Speziale et al. (1991), and Shih and Lumley (1985)). The modelling of the slow term is based on the idea that for decaying anisotropic turbulence, the slow pressure-strain term can be characterised by τ_{ij} , ε , and ν (Pope (2001)). On the other hand, for the case of rapidly distorted flows, it is expected that the resolved/mean strain rate tensors play a dominant role (Townsend (1954)). Nevertheless, even for homogeneous shear flows, Reynolds (1972) showed that the inclusion of mean strain rate in the modelling is required. Thus a general model for pressure-strain must be able to predict the right behaviour for both isotropic and rapid distortion limits, thereby requiring that the models for both $\Pi_{ij}^{(s)}$ and $\Pi_{ij}^{(r)}$ be included. Three models that are formulated based on this reasoning: two linear and one non-linear model, will now be introduced.

Linear pressure-strain models

The linear model of Launder, Reece, and Rodi (Launder et al. (1975)) combines Rotta’s model for the slow term $\Pi_{ij}^{(s)}$ with the rapid term $\Pi_{ij}^{(r)}$. For LES, the corresponding model equation can be expressed as

$$\begin{aligned} \Pi_{ij} &= \Pi_{ij}^{(s)} + \Pi_{ij}^{(r)} \\ &= -C_R \varepsilon a_{ij} - \frac{(C_2 + 8)}{11} \left(\mathcal{P}_{ij} - \frac{2}{3} \mathcal{P} \delta_{ij} \right) - \frac{(30C_2 - 2)}{55} k_{sgs} \langle S_{ij} \rangle \\ &\quad - \frac{(8C_2 - 2)}{11} \left(D_{ij} - \frac{2}{3} \mathcal{P} \delta_{ij} \right) \end{aligned} \quad (2.18)$$

$$\begin{aligned} &= -C_R \varepsilon a_{ij} + \frac{4}{5} k_{sgs} \langle S_{ij} \rangle + \frac{3}{11} (2 + 3C_2) k_{sgs} \left(\langle S_{ik} \rangle a_{kj} + a_{ik} \langle S_{kj} \rangle - \frac{2}{3} \langle S_{kl} \rangle a_{kl} \delta_{ij} \right) \\ &\quad + \frac{1}{11} (10 - 7C_2) k_{sgs} (\langle \Omega_{ik} \rangle a_{kj} - a_{ik} \langle \Omega_{kj} \rangle). \end{aligned} \quad (2.19)$$

¹In terms of a_{ij} .

The constants were calibrated to $C_1 = 1.5$ and $C_2 = 0.4$. $\langle S_{ij} \rangle$ and $\langle \Omega_{ij} \rangle$ are the resolved strain rate and rotation rate tensors respectively that are defined as

$$\langle S_{ij} \rangle = \frac{1}{2} \left\langle \frac{\partial u_i}{\partial x_j} + \frac{\partial u_j}{\partial x_i} \right\rangle,$$

$$\langle \Omega_{ij} \rangle = \frac{1}{2} \left\langle \frac{\partial u_i}{\partial x_j} - \frac{\partial u_j}{\partial x_i} \right\rangle.$$

Equation (2.19) is called the LRR-QI model. [Launder et al. \(1975\)](#) also formulated a simplified version of LRR-QI by assuming that the rapid part of pressure-strain works entirely to reduce the anisotropy in the production between different SGS stress components. With this assumption of isotropisation of production (IP), the LRR-IP model was formulated. This is derived in an attempt to represent the rapid term based only on the second term in the LRR-QI model (Eq. (2.18)), as it was found to be the dominant term in the formulation for $\Pi_{ij}^{(r)}$. The LRR-IP model can be formulated in LES as

$$\begin{aligned} \Pi_{ij} &= -C_R \varepsilon a_{ij} - C_2 \left(\mathcal{P}_{ij} - \frac{2}{3} \mathcal{P} \delta_{ij} \right) \\ &= -C_R \varepsilon a_{ij} + \frac{4}{3} C_2 k_{sgs} \langle S_{ij} \rangle + C_2 k_{sgs} \left(\langle S_{ik} \rangle a_{kj} + a_{ik} \langle S_{kj} \rangle - \frac{2}{3} \langle S_{kl} \rangle a_{lk} \delta_{ij} \right) \\ &\quad + C_2 k_{sgs} (\langle \Omega_{ik} \rangle a_{kj} - a_{ik} \langle \Omega_{kj} \rangle), \end{aligned} \quad (2.20)$$

where the constant C_1 is analogous to Rotta's constant. They were calibrated to $C_1 = 1.5$ and $C_2 = 0.6$. As the first term decreases the anisotropy and tends to a more isotropic state, the second term tends to isotropise the turbulence production tensor ([Launder et al. \(1975\)](#)). This modelling approach for $\Pi_{ij}^{(r)}$ was derived by [Naot et al. \(1970\)](#) who used this to solely represent the entire pressure-strain term, while the approach taken by [Launder et al. \(1975\)](#) combines this term with Rotta's model for $\Pi_{ij}^{(s)}$ for a more general prediction. [Launder et al. \(1975\)](#) conducted RANS using LRR-QI and LRR-IP models and reported that the QI model outperformed the IP model in certain cases like the case of axisymmetric contraction, while for homogeneous shear flows and flow over curved surfaces, both models reported similar predictions of the normal stresses.

Non-linear pressure-strain model

[Speziale et al. \(1991\)](#) attempted to make an improvement over LRR models where the coefficients of the tensors are functions of anisotropy and as a result, the pressure-strain term becomes nonlinear. For plane homogeneous turbulent flows, a general hierarchy of models with second order closure was taken as the starting point, from which the equilibrium states of the invariants (which were non-trivial) were found to be well captured by inclusion of a non-linearity in terms of the anisotropy tensor to the equation. The resulting expression for

Π_{ij} that came to be called as the SSG model is expressed in LES as follows,

$$\begin{aligned} \Pi_{ij} = & -\frac{(C_1\varepsilon + C_1^*\mathcal{P})}{2}a_{ij} + \frac{C_2}{4}\varepsilon\left(a_{ik}a_{kj} - \frac{1}{3}a_{mn}a_{nm}\delta_{ij}\right) + \frac{(2C_3 - C_3^*II_a^{1/2})}{2}k_{sgs}\langle S_{ij}\rangle \\ & + \frac{C_4}{2}k_{sgs}\left(\langle S_{ik}\rangle a_{kj} + a_{ik}\langle S_{kj}\rangle - \frac{2}{3}\langle S_{kl}\rangle a_{lk}\delta_{ij}\right) + \frac{C_5}{2}k_{sgs}\left(\langle \Omega_{ik}\rangle a_{kj} - a_{ik}\langle \Omega_{kj}\rangle\right). \end{aligned} \quad (2.21)$$

The values of the constants were calibrated from experimental data to $C_1 = 3.4$, $C_1^* = 1.8$, $C_2 = 4.2$, $C_3 = 0.8$, $C_3^* = 1.3$, $C_4 = 1.25$, $C_5 = 0.4$. II_a is the second invariant of the anisotropy defined as $II_a = a_{ij}a_{ji}$. The SSG model was reported to perform better than LRR models for different cases of homogeneous turbulent flows including axisymmetric contraction and rotating shear flows simulated using RANS. However, for flows that exhibited strong levels of anisotropy, the SSG model was not recommended as it gave unrealisable² predictions of Reynolds stresses (Speziale et al. (1991)).

2.4.2 Modelling of the dissipation term

According to Kolmogorov's local isotropy hypothesis, the anisotropy in the large scales disappears during the energy cascade and the small scales of motion maintain a state of (statistical) isotropy. This local isotropy hypothesis, however, does not apply to cases of turbulence, for instance near the wall in turbulent channel flows (Spalart (1988)). Irrespective of this, the dissipation tensor is often modelled isotropically. An explanation for this lies in the modelling of the slow pressure-strain term. Lumley and Newman (1977) suggested a modelling approach where the anisotropic part of dissipation be included in the model for the slow pressure-strain term. By this interpretation, Rotta's model for the slow pressure-strain term is modelled such that it reduces the anisotropy in the dissipation tensor. Therefore, the only term that is left to be modelled is the isotropic part of the the dissipation tensor which reads

$$\varepsilon_{ij}^{iso} = \frac{2}{3}\varepsilon\delta_{ij}. \quad (2.22)$$

2.5 Formulation of an explicit model

The simplifications and the models that have been discussed so far do not directly result in a linear expression where the SGS stresses are explicitly determined. Even with the use of linear LRR models for pressure-strain term, the left hand side (LHS) of the Eq. (2.16) is non-linear in terms of τ_{ij} . Rewriting Eq. (2.16) in terms of normalised SGS stress anisotropy,

$$\left(a_{ij} + \frac{2}{3}\delta_{ij}\right)\left(\frac{\mathcal{P}}{\varepsilon} - 1\right) = \frac{1}{\varepsilon}(\mathcal{P}_{ij} + \Pi_{ij} - \varepsilon_{ij}). \quad (2.23)$$

²Strong realisability condition implies that the normal SGS stresses stay positive, i.e. $\tau_{ii} > 0$. Models that violate this condition are not said to satisfy strong realisability.

$$\begin{aligned}
\mathbf{T}^{(1)} &= \langle \mathbf{S}^* \rangle & \mathbf{T}^{(2)} &= \langle \mathbf{S}^* \rangle^2 - \frac{1}{3} II_S \mathbf{I} \\
\mathbf{T}^{(3)} &= \langle \Omega^* \rangle^2 - \frac{1}{3} II_\Omega \mathbf{I} & \mathbf{T}^{(4)} &= \langle \mathbf{S}^* \rangle \langle \Omega^* \rangle - \langle \Omega^* \rangle \langle \mathbf{S}^* \rangle \\
\mathbf{T}^{(5)} &= \langle \mathbf{S}^* \rangle^2 \langle \Omega^* \rangle - \langle \Omega^* \rangle \langle \mathbf{S}^* \rangle^2 & \mathbf{T}^{(6)} &= \langle \mathbf{S}^* \rangle \langle \Omega^* \rangle^2 + \langle \Omega^* \rangle^2 \langle \mathbf{S}^* \rangle - \frac{2}{3} IV \mathbf{I} \\
\mathbf{T}^{(7)} &= \langle \mathbf{S}^* \rangle^2 \langle \Omega^* \rangle^2 + \langle \Omega^* \rangle^2 \langle \mathbf{S}^* \rangle^2 - \frac{2}{3} IV \mathbf{I} & \mathbf{T}^{(8)} &= \langle \mathbf{S}^* \rangle \langle \Omega^* \rangle \langle \mathbf{S}^* \rangle^2 - \langle \mathbf{S}^* \rangle^2 \langle \Omega^* \rangle \langle \mathbf{S}^* \rangle \\
\mathbf{T}^{(9)} &= \langle \Omega^* \rangle \langle \mathbf{S}^* \rangle \langle \Omega^* \rangle^2 - \langle \Omega^* \rangle^2 \langle \mathbf{S}^* \rangle \langle \Omega^* \rangle & \mathbf{T}^{(10)} &= \langle \Omega^* \rangle \langle \mathbf{S}^* \rangle^2 \langle \Omega^* \rangle^2 - \langle \Omega^* \rangle^2 \langle \mathbf{S}^* \rangle^2 \langle \Omega^* \rangle
\end{aligned}$$

Table 2.2: Tensorial bases functions for the solution space of a_{ij} in the ‘simplified’ subgrid-scale stress equation (Pope (1975)) shown in matrix form.

The non-linearity which still persists in Eq. (2.23) is caused by the presence of \mathcal{P}/ε , which can be expressed as a function of a_{ij} ($\mathcal{P}/\varepsilon = -a_{ij} \langle S_{ij}^* \rangle k_{sgs}/\varepsilon$). One way to deal with this non-linearity is to retain the ratio \mathcal{P}/ε as an extra unknown and sought out explicit solutions for a_{ij} . The solution for a_{ij} becomes a function of SGS kinetic energy, SGS dissipation, resolved strain rate and rotation rate tensors. This can further be simplified if the resolved strain rate and rotation rate tensors are normalised using a turbulent time scale, i.e. k_{sgs}/ε . The normalised quantities then become

$$\begin{aligned}
\langle S_{ij}^* \rangle &= \frac{k_{sgs}}{\varepsilon} \left[\frac{1}{2} \left\langle \frac{\partial u_i}{\partial x_j} + \frac{\partial u_j}{\partial x_i} \right\rangle \right], & \text{and} \\
\langle \Omega_{ij}^* \rangle &= \frac{k_{sgs}}{\varepsilon} \left[\frac{1}{2} \left\langle \frac{\partial u_i}{\partial x_j} - \frac{\partial u_j}{\partial x_i} \right\rangle \right].
\end{aligned}$$

With these normalised resolved strain rate and rotation rate tensors, Pope (1975) formulated ten tensorial bases for the solution space of a_{ij} , i.e. independent, symmetric, and deviatoric tensorial functions of $\langle S_{ij}^* \rangle$ and $\langle \Omega_{ij}^* \rangle$ which can be used to express a_{ij} . This relation is written as

$$a_{ij} = \sum_{n=1}^{10} G^{(n)} T_{ij}^{(n)}, \quad (2.24)$$

where $T_{ij}^{(1)} - T_{ij}^{(10)}$ are the tensorial bases given in Tab. 2.2, and $G^{(1)} - G^{(10)}$ are coefficients that depend on five invariants of $\langle S_{ij}^* \rangle$ and $\langle \Omega_{ij}^* \rangle$: $II_S = tr(\langle S \rangle^2)$, $II_\Omega = tr(\langle \Omega \rangle^2)$, $III_S = tr(\langle S \rangle^3)$, $IV = tr(\langle S \rangle \langle \Omega \rangle^2)$, and $V = tr(\langle S \rangle^2 \langle \Omega \rangle^2)$. This was accomplished using Cayley-Hamilton theorem³. Depending on the choice of tensors (and coefficients), the complexity of the model can be varied from simple linear to more complex nonlinear models.

2.5.1 Smagorinsky model

The tensorial bases shown in Tab. 2.2 show a wide range of non-linear models that can be formulated for the normalised SGS stress anisotropy. Based on the choice of tensors, the

³States that every square matrix \mathbf{S} , satisfies its own characteristic equation $S^3 - I_S S^2 + II_S S - III_S I = 0$, where I_S, II_S , and III_S are linear, quadratic, and cubic combinations of the eigenvalues. As a consequence, higher order matrices, \mathbf{S}^n for $n \geq 3$ can be expressed as a linear combination of \mathbf{I} , \mathbf{S} , and \mathbf{S}^2 with coefficients that are functions of its invariants (Pope (2001)).

degree of non-linearity in the formulation can be varied. Consider the choice of the linear term, i.e. $T_{ij}^{(1)}$. The normalised SGS stress anisotropy thus becomes,

$$\begin{aligned} a_{ij} &= G^{(1)} \langle S_{ij}^* \rangle \\ &= G^{(1)} \frac{k_{sgs}}{\varepsilon} \langle S_{ij} \rangle \end{aligned} \quad (2.25)$$

Equation (2.25) can be rewritten in terms of the SGS stress anisotropy as

$$\begin{aligned} \tau_{ij}^d &= k_{sgs} G^{(1)} \frac{k_{sgs}}{\varepsilon} \langle S_{ij} \rangle \\ &= G^{(1)} \frac{k_{sgs}^2}{\varepsilon} \langle S_{ij} \rangle \\ &= G^{*(1)} \langle S_{ij} \rangle \end{aligned} \quad (2.26)$$

where $G^{*(1)} = G^{(1)} \frac{k_{sgs}^2}{\varepsilon}$, rewritten in this way for the sake of convenience. If we assume that the SGS kinetic energy production and dissipation are in balance,

$$\begin{aligned} \mathcal{P} &= \varepsilon, \\ -\tau^d \langle S_{ij} \rangle &= \varepsilon \end{aligned} \quad (2.27)$$

We now substitute Eq. (2.26) in the LHS of Eq. (2.27) and use the scaling $\varepsilon \sim \frac{U^3}{L}$ (for the RHS), where U and L are velocity and length scales, respectively, which are chosen as

$$U \sim \Delta \sqrt{\langle S_{ij} \rangle \langle S_{ij} \rangle}, \quad \text{and} \quad L \sim \Delta.$$

Δ is the LES grid dimension. As per this scaling, Eq. (2.27) can be rewritten with C^ϵ as a constant chosen for the modelling of SGS kinetic energy dissipation,

$$\begin{aligned} -G^{*(1)} \langle S_{ij} \rangle \langle S_{ij} \rangle &= C^\epsilon \frac{(\Delta \sqrt{\langle S_{ij} \rangle \langle S_{ij} \rangle})^3}{\Delta}, \\ G^{*(1)} &= -C^\epsilon \Delta^2 \sqrt{\langle S_{ij} \rangle \langle S_{ij} \rangle}. \end{aligned} \quad (2.28)$$

The corresponding expression for SGS stress anisotropy is thereby expressed (in a linear form) as

$$\tau_{ij}^d = \left(-C^\epsilon \Delta^2 \sqrt{\langle S_{ij} \rangle \langle S_{ij} \rangle} \right) \langle S_{ij} \rangle. \quad (2.29)$$

Equation (2.29) is a restatement of the Smagorinsky model, where the deviatoric part of SGS stress τ_{ij}^d is modelled using only the resolved strain rate tensor. The isotropic part of τ_{ij} , i.e. $1/3 \tau_{kk} \delta_{ij}$ modifies the pressure in the NS equations and hence does not affect the prediction of resolved velocity fields. If we replace C^ϵ by $2\sqrt{2}C_S^2$, we obtain the model for τ_{ij}^d proposed by Smagorinsky (1963), which reads

$$\tau_{ij}^d = -2\nu_T \langle S_{ij} \rangle. \quad (2.30)$$

The eddy viscosity ν_T is defined as

$$\begin{aligned}\nu_T &= (C_S \Delta)^2 \sqrt{2 \langle S_{ij} \rangle \langle S_{ij} \rangle}, \\ &= (C_S \Delta)^2 \| \langle S \rangle \| \end{aligned} \quad (2.31)$$

where C_S is the Smagorinsky constant, dependent on the Kolmogorov constant C_K through the relation $C_S = (1/\pi)(2/(3C_K))^{2/3}$ (Pope (2001)). The value of C_S is typically chosen to lie between 0.10 and 0.25. The use of a constant value for C_S makes the eddy viscosity constant irrespective of the local flow regime, i.e. unable to adapt based on the presence of laminar and turbulent regions that are localised, or to the presence of walls. To circumvent this, Germano et al. (1991) proposed a dynamic approach to evaluate the constant C_S by performing an additional filtering operation. The second filter $\langle \cdot \rangle_g$ with a filter width Δ_g is chosen to be larger than Δ_f , the filter width of the first filter $\langle \cdot \rangle_f$. If,

$$\begin{aligned}\langle \tau_{ij} \rangle_g &= \langle \langle u_i u_j \rangle_f \rangle_g - \langle \langle u_i \rangle_f \langle u_j \rangle_f \rangle_g, \quad \text{and} \\ L_{ij} &= \langle \langle u_i u_j \rangle_f \rangle_g - \langle \langle u_i \rangle_f \rangle_g \langle \langle u_j \rangle_f \rangle_g, \quad \text{then} \\ L_{ij} - \langle \tau_{ij} \rangle_g &= \langle \langle u_i \rangle_f \langle u_j \rangle_f \rangle_g - \langle \langle u_i \rangle_f \rangle_g \langle \langle u_j \rangle_f \rangle_g. \end{aligned} \quad (2.32)$$

Using Smagorinsky's formulation, the deviatoric part of Eq. (2.32) can be expressed as

$$L_{ij}^d - \langle \tau_{ij} \rangle_g^d = 2C_S^2 \Delta_f^2 \| \langle S \rangle_f \| \langle S_{ij} \rangle_{f,g} - 2C_S^2 \Delta_g^2 \| \langle S \rangle_f \| \langle \langle S_{ij} \rangle_f \rangle_g. \quad (2.33)$$

Lilly (1992) proposed a method of determining the constant in the Eq. (2.33) using least squares technique. In the above expression, we replace C_S^2 with C_d . If the terms on the LHS and RHS of Eq. (2.33) are reduced to \mathcal{L}_{ij} and $C_d \mathcal{M}_{ij}$ respectively, the value of C_d can be found by solving the above expression by minimising the mean-square error as follows,

$$\begin{aligned}R &= (\mathcal{L}_{ij} - C_d \mathcal{M}_{ij})^2 \\ &= \mathcal{L}_{ij} \mathcal{L}_{ij} - 2C_d \mathcal{M}_{ij} \mathcal{L}_{ij} + C_d^2 \mathcal{M}_{ij} \mathcal{M}_{ij}. \end{aligned}$$

The above expression is differentiated with respect to C_d and set to zero to find the minima.

$$\begin{aligned}\frac{\partial R}{\partial C_d} &= -2\mathcal{M}_{ij} \mathcal{L}_{ij} + 2C_d \mathcal{M}_{ij} \mathcal{M}_{ij} = 0, \\ 2\mathcal{M}_{ij} \mathcal{L}_{ij} &= 2C_d \mathcal{M}_{ij} \mathcal{M}_{ij}, \\ C_d &= \frac{\mathcal{L}_{ij} \mathcal{M}_{ij}}{\mathcal{M}_{mn} \mathcal{M}_{mn}}. \end{aligned} \quad (2.34)$$

The Smagorinsky model is a purely dissipative model when the value of C_d is to be maintained positive everywhere in the flow field. However, in some cases, the dynamic procedure shown above leads to unstable simulations, when C_d takes negative values locally. In such situations, the numerator and denominator in Eq. (2.34) are averaged in all homogeneous directions thereby maintaining a strictly positive nature.

2.5.2 Explicit algebraic subgrid-scale stress model by Marstorp et al. (2009)

In the case of RANS, separate equations were formulated to find the value of \mathcal{P}/ε (Girimaji (1996) and Wallin and Johansson (2000)), while in the case of LES, Marstorp et al. (2009) completely removed the presence of non-linearity by assuming that the SGS production and dissipation maintain perfect equilibrium. As a consequence, the LHS of Eq. (2.23) disappears and the resulting equation becomes

$$\mathcal{P}_{ij} + \Pi_{ij} - \varepsilon_{ij} = 0. \quad (2.35)$$

A modified LRR-QI model was employed to model the pressure-strain term and an isotropic model was used for the dissipation term. The modification that was done on the original formulation of LRR-QI model was that the coefficient of the second term on the RHS of Eq. (2.19) was reduced from 4/5 to 3/5. This modification seemed to increase the anisotropy of the predicted SGS stress. The constant C_2 in the modified LRR-QI was taken to be 5/9 which, upon substitution resulted in an implicit expression for a_{ij} of the form

$$C_1 a_{ij} = \left[\frac{-11}{15} \langle S_{ij}^* \rangle + \frac{4}{9} \left(a_{ik} \langle \Omega_{kj}^* \rangle - \langle \Omega_{ik}^* \rangle a_{kj} \right) \right]. \quad (2.36)$$

For explicit algebraic models in RANS, the final formulation was obtained by using only the first three tensors $T_{ij}^{(1)} - T_{ij}^{(3)}$ (Gatski and Speziale (1993), Girimaji (1996), Wallin (2000), Sjögren and Johansson (2000)). This is following the argument made by Pope (1975) that for statistically two-dimensional flows, these three tensors can be used to construct the solution space with the coefficients $G^{(4)} - G^{(10)}$ set to zero. Furthermore, it is to be noted that the tensor $T_{ij}^{(3)}$ does not alter the velocity fields and instead modifies only the pressure. Therefore, using the same tensors as used by Pope (1975) and neglecting the tensor $T_{ij}^{(3)}$, Marstorp et al. (2009) formulated the final explicit model for SGS stress. The final model reads

$$\tau_{ij} = k_{sgs} \left(\frac{2}{3} \delta_{ij} + G^{(1)} \langle S_{ij}^* \rangle + G^{(2)} \left(\langle S_{ik}^* \rangle \langle \Omega_{kj}^* \rangle - \langle \Omega_{ik}^* \rangle \langle S_{kj}^* \rangle \right) \right). \quad (2.37)$$

In order to solve the RHS of Eq. (2.37), the SGS kinetic energy and an SGS time scale were required. Marstorp et al. (2009) formulated two versions of the model: a dynamic and a non-dynamic, based on the way k_{sgs} is determined. The time scale was defined as $\tau^* = k_{sgs}/\varepsilon$. The final expressions are shown in Tab. 2.3. The detailed derivation of Eq. (2.35), the expressions, and the values for the model constants are given in appendix B.

2.5.3 Formulation of an equation for the evolution of subgrid-scale kinetic energy

The approach taken by Marstorp et al. (2009) to evaluate the SGS kinetic energy is by using a Smagorinsky velocity scale, from which a local algebraic equation is obtained. One of the

Version	k_{sgs}	τ^*
Dynamic	$c\Delta^2\ \langle S \rangle\ ^2$	$c'_3 \frac{1.5C_K^{1.5}\sqrt{c}}{2C_S}\ \langle S \rangle\ ^{-1}$
Non-dynamic	$-\frac{1}{2}G^{(1)}c_k^2\Delta^2\ \langle S \rangle\ ^2$	$c_3\ \langle S \rangle\ ^{-1}$

Table 2.3: Dynamic and non-dynamic formulations for the subgrid-scale kinetic energy and time scale in the explicit algebraic subgrid-scale stress model of [Marstorp et al. \(2009\)](#)

reasons to sought out an algebraic relation for k_{sgs} is the assumption that the SGS kinetic energy maintains a state of equilibrium with the resolved scales adapting instantly to the resolved velocity scales. This is a consequence of assuming that the SGS kinetic energy production and dissipation are in perfect balance. If such a limiting assumption is not made, other ways to trace the evolution of k_{sgs} can be sought out. An obvious starting point is to model the trace of SGS stress evolution equation (Eq. (2.14)). This requires modelling of the transport and the dissipation terms. A common approach for modelling the transport quantities is to model the turbulent and the pressure transport together using a single model. Based on this approach, a gradient diffusion model proposed by [Shir \(1973\)](#) can be employed to model the (pressure and turbulent) transport quantities. The dissipation term can modelled using a velocity scale computed from k_{sgs} and a length scale which was taken to be the local mesh size. The transport and the dissipation models thus read,

$$\mathcal{T}_{mmk}^{(u+p)} = -C_s \frac{k_{sgs}^2}{\varepsilon} \frac{\partial k_{sgs}}{\partial x_k}, \quad (2.38)$$

$$\varepsilon = C_c \frac{k_{sgs}^{3/2}}{\Delta}. \quad (2.39)$$

The practice of modelling both pressure and turbulent transport together using a single model became very common after [Lumley \(1979\)](#) examined the variation of pressure and turbulent transport quantities in the turbulent kinetic energy equation and reported that the turbulent transport represents the majority of the total transport while the pressure transport merely counters the turbulent transport. This counter gradient hypothesis for pressure transport resulted in the application of a single gradient diffusion model to represent the effects of both turbulent and pressure transport.

With this modelling strategy, [Yoshizawa and Horiuti \(1985\)](#) formulated an equation for evolution of k_{sgs} that reads

$$\frac{\langle D \rangle k_{sgs}}{Dt} = -\tau_{ij} \frac{\partial \langle u_i \rangle}{\partial x_j} + \frac{\partial}{\partial x_j} \left[(\nu_k + \nu) \frac{\partial k_{sgs}}{\partial x_j} \right] - C_c \frac{k_{sgs}^{3/2}}{\Delta}, \quad (2.40)$$

where C_c was calibrated to 1. The artificial viscosity ν_k (analogous to an eddy viscosity) was formulated based on the velocity scale and length scale and reads

$$\nu_k = C_k \sqrt{k_{sgs}} \Delta, \quad (2.41)$$

where C_k is taken as 0.1. Using Eq. (2.40) avoids the assumption that the SGS kinetic energy instantly adapts based on the resolved velocity scales and instead allows us to evaluate its transient behaviour.

2.6 Modifications required to account for the Coriolis force

The governing equations and the modelling for SGS stresses that were discussed so far are only applicable in an inertial frame of reference with no body forces in play. When turbulence is subject to uniform rotation, centrifugal and Coriolis forces affect the evolution of turbulence in the (filtered) NS equations. The centrifugal force can be absorbed into the filtered pressure resulting in a modified pressure term. Thereby the centrifugal force does not alter the resolved velocity fields directly and for this reason will not be a focus of the current discussion. The Coriolis force on the other hand, influences the evolution of resolved velocity fields and also affects the SGS stresses. As mentioned in Ch. 1, the SGS scales becomes less dissipative in the presence of strong system rotation. This must be appropriately captured by the model used for the SGS stress. EASSMs require some modifications to the equations such that they can be used in the case of rotating turbulence.

2.6.1 Changes to the governing equations

The Coriolis force in the filtered NS equation (is to added on the RHS of Eq. (2.2)) can be expressed in index notation as

$$\langle C_{ij}^f \rangle = \varepsilon_{ijk} \Omega_j^s \langle u_k \rangle, \quad (2.42)$$

where ε_{ijk} is called the Levi-Civita symbol, which takes the value of +1 for even permutations of ijk , is -1 for odd permutations, and is 0 when the indices repeat. Ω_j^s is the system rotation vector. In the evolution equation for SGS stresses, the contribution due to the Coriolis force appears as

$$C_{ij}^T = -2 (\varepsilon_{imn} \Omega_m^s \tau_{nj} + \varepsilon_{jmn} \Omega_m^s \tau_{ni}). \quad (2.43)$$

From Eq. (2.43), certain aspects of the Coriolis force become evident. Firstly, the contribution of the Coriolis force in the SGS stress evolution equation is in closed form. Secondly, the tensor C_{ij}^T is traceless⁴, and therefore does not (directly) alter the total kinetic energy of the system. In the absence of system rotation, Eq. (2.43) becomes zero and thus, including C_{ij}^T/ε to the RHS of Eq. (2.23) as an additional term will naturally account for rotation. Another way of

⁴Consider $\Omega^s = (0, 0, 1)$; Then, $C_{ii}^T = -4(\varepsilon_{i3n} \tau_{ni}) = -4(\varepsilon_{132} \tau_{21} + \varepsilon_{231} \tau_{21}) = 0$.

including this term in the governing equations is to incorporate the system rotation vector into the definition of the resolved rotation rate tensor to get a modified rotation rate tensor. Marstorp et al. (2009) took the second approach and defined a modified resolved rotation rate tensor given by

$$\langle \Omega_{ij}^R \rangle = \langle \Omega_{ij} \rangle + \frac{13}{4} \varepsilon_{ikj} \Omega_k^s. \quad (2.44)$$

The factor of 13/4 in Eq. (2.44) is a result of the total contribution from the production, pressure-strain and a component of Coriolis term. The procedure for deriving Eq. (2.44) is documented in the work of Wallin and Johansson (2000). This modification of the rotation rate tensor increases the value of the corresponding invariant II_{Ω}^R , thereby reducing the coefficients $G^{(1)}$, and $G^{(2)}$ in Eq. (2.37). As a consequence, this lowers the prediction of SGS stresses. As mentioned earlier in Sec. 1.2.2, the SGS production thus modelled using the (reduced) SGS stress tensor replicates the effect of an suppressed total energy cascade. It must be pointed out that, when the contribution from the Coriolis term C_{ij}^T is included in the derivation of an explicit model, we do not obtain the factor 13/4 (in Eq. (2.44)) for the modified rotation rate tensor. Instead, we obtain the factor 9/2. However, in this thesis, we stick to the modification provided in Eq. (2.44) when using the EASSM of Marstorp et al. (2009) for rotating cases.

2.6.2 Some important parameters that characterise rotation

The inclusion of Coriolis force to the equations introduces a new time scale. The relative importance of rotation can be represented using some parameters which will be defined in the current section.

Rossby number

The ratio the inertial forces to the Coriolis force is an important parameter in rotating turbulence and is called the Rossby number:

$$Ro = \frac{U^2/L}{2\Omega_s U} = \frac{U}{2\Omega_s L}, \quad (2.45)$$

where, U and L are the velocity and length scales respectively, and Ω_s is the system rotation rate. The Rossby number can also be interpreted as a ratio of rotation to inertial time scales. Strong rotations are characterised by $Ro \ll 1$.

Zeman wavenumber

As the rotation rate of the system increases, the Coriolis force starts to dominate over the inertial forces thereby controlling the evolution of the different length scales in turbulence. For weak case of rotation, i.e. $Ro \approx 1$, the viscous scales are not always influenced by rotation. On the other hand, for $Ro \ll 1$, rotation influences a large range of scales, including the scales

inside the universal equilibrium range. Zeman (1994) introduced a wavenumber κ_Ω , which gives an indication of the largest wavenumber that is affected by rotation. This came to be known as the Zeman wavenumber, and is defined as

$$\kappa_\Omega = \sqrt{\frac{\Omega_s^3}{\varepsilon}}. \quad (2.46)$$

Ekman number

For completion, we shall also define the Ekman number here. It is simply a ratio of the Rossby number to the Reynolds number of the flow. It gives a measure of the ratio of the viscous force to the Coriolis force. Ekman number reads

$$Ek = \frac{\nu U/L^2}{2\Omega_s U} = \frac{\nu}{2\Omega_s L^2}. \quad (2.47)$$

2.7 Closing remarks

The modelling approaches that were described so far either simplify the final expression for SGS stress or bring about additional mathematical complexities. For instance, when deciding on a model for the pressure-strain term, the SSG model will introduce non-linearity due to the coefficients of the slow term. Therefore, the need for a non-linear representation for the slow term must first be analysed in order to make the choice for pressure-strain modelling. The assumption of perfect equilibrium between the production and dissipation of SGS kinetic energy provides immense mathematical ease in deriving a model for the SGS stresses. It can, however, limit its applicability to different complex flow cases. In conclusion, for deriving a model that can represent the SGS evolution for strongly rotating flows, the assumptions that are made along the way should be critically questioned.

Chapter 3

Methodology

3.1 DNS code: TurBo

Two sets of DNS are conducted in this work: the first set to generate forced statistically steady-state results with and without rotation for carrying out a priori studies and the second set of simulations of forced isotropic, and rotating and non-rotating decaying cases for a posteriori analysis. In order to carry out DNS for our analyses, the code written by Tiago Pestana (a PhD candidate at Aerodynamics, TU Delft) was used. The rotational form of the NS equations is implemented in this code, which in vector notation reads

$$\frac{\partial \vec{u}}{\partial t} + (\vec{\omega} \times \vec{u}) = -\vec{\nabla} \frac{P}{\rho} + \nu \nabla^2 \vec{v} + \vec{F} \quad (3.1)$$

where \vec{u} is the velocity vector, $\vec{\omega}$ is the vorticity vector given by $(\vec{\nabla} \times \vec{u})$, P/ρ total pressure (head) given by $p/\rho + 1/2 (\vec{u} \cdot \vec{u})$, and \vec{F} is the force vector. The governing equations are solved using pseudo-spectral methods with the non-linear convolutions computed in physical space using the 3/2 de-aliasing technique to remove the errors associated to aliasing. The time integration for the convective term is performed using a 3rd order Runge-Kutta scheme. The viscous and the Coriolis term (in the presence of system rotation) on the other hand are integrated exactly in time using the integration factor technique of Rogallo (1977). The validation of the code was done for canonical cases such as Taylor-Green flow.

3.2 LES code: INCA

All LES in this work are done using the finite volume solver INCA on staggered meshes. In INCA, a conservative form of (filtered) NS equation is implemented, which reads

$$\frac{\partial \langle u_i \rangle}{\partial t} + \frac{\partial \langle u_i \rangle \langle u_j \rangle}{\partial x_j} = -\frac{1}{\rho} \frac{\partial \langle p \rangle}{\partial x_i} + \nu \frac{\partial^2 \langle u_i \rangle}{\partial x_j \partial x_j} - \frac{\partial \tau_{ij}}{\partial x_j} + F_i. \quad (3.2)$$

A 3rd order Runge-Kutta scheme is used for time integration. The convective and the diffusive terms are computed using a second order central difference scheme. At every Runge-Kutta sub-step, a Poisson equation for pressure is solved using a fast Fourier transform based solver which uses modified wavenumbers to obtain the same second order accuracy as the convective and diffusive flux schemes. The code has been validated for a variety of turbulence scenarios some of which are documented in [Hickel et al. \(2010\)](#), [Meyer et al. \(2010\)](#), [Remmler and Hickel \(2012\)](#), [Borchert et al. \(2014\)](#), and [Egerer et al. \(2015\)](#), for example.

3.3 Forcing scheme

Throughout this work, we carry out forced simulations both with and without rotation. In order to do this a three-dimensional homogeneous random forcing scheme developed by [Alvelius \(1999\)](#) is used. The exact determination of the power input is entirely based on the selection of the forcing parameters at the start of the simulation. In the kinetic energy evolution equation, the external forcing has two types of contributions: a force-force correlation (integrated over time) and a force-velocity correlation. The advantage of the current forcing scheme over other schemes developed by [Ghosal et al. \(1995\)](#) and [Eswaran and Pope \(1988\)](#) is that in the forcing scheme of [Alvelius \(1999\)](#), on average, the power input is exclusively due to the contribution from the force-force correlation. The generated force is uncorrelated with velocity and thereby the total contribution due to the force-velocity term to the mean kinetic energy becomes zero. The force is formulated as

$$F_i = A_{ran}(\kappa, t)e1_i(\kappa) + B_{ran}(\kappa, t)e2_i(\kappa), \quad (3.3)$$

where, A_{ran} and B_{ran} are force coefficients, and $e1_i$ and $e2_i$ are basis vectors. We shall discuss a few of the characteristics of the of the generated force in way of which we shall define the different terms in Eq. (3.3). The generated force is divergence free and hence does not modify the pressure directly. This can be achieved from the selection of the basis vectors as follows,

$$\begin{aligned} e1_x &= \frac{\kappa_y}{(\kappa_x^2 + \kappa_y^2)^{1/2}}, & e2_x &= \frac{\kappa_x \kappa_z}{\kappa(\kappa_x + \kappa_y)^{1/2}}, \\ e1_y &= -\frac{\kappa_x}{(\kappa_x^2 + \kappa_y^2)^{1/2}}, & e2_y &= \frac{\kappa_y \kappa_z}{\kappa(\kappa_x + \kappa_y)^{1/2}}, \\ e1_z &= 0, & e2_z &= -\frac{(\kappa_x + \kappa_y)^{1/2}}{\kappa}. \end{aligned}$$

The coefficients A_{ran} and B_{ran} in Eq. (3.3) are expressed as

$$A_{ran} = \left(\frac{F_{sph}}{2\pi\kappa^2} \right)^{1/2} \exp(i\theta_1) g_A(\phi), \quad (3.4)$$

$$B_{ran} = \left(\frac{F_{sph}}{2\pi\kappa^2} \right)^{1/2} \exp(i\theta_2) g_B(\phi). \quad (3.5)$$

where, g_A and g_B are real valued functions defined such that $g_A^2 + g_B^2 = 1$. θ_1 and θ_2 lie within 0 and 2π and ϕ lies within 0 and π . θ_1 , θ_2 , and ϕ are randomly generated real valued numbers. F_{sph} is the force spectrum that is based on the prescribed input parameters.

The input parameters are κ_f which is the modes where the forcing is most concentrated. Another parameter c_f determines the degree of concentration. κ_a and κ_b determine the lower and upper wavenumber bound for the forcing. Finally another parameter A_f determines value of the force spectrum at $\kappa = \kappa_f$. These input parameters are related as

$$F_{sph}(\kappa) = A_f \exp\left(-\frac{(\kappa - \kappa_f)^2}{c_f}\right), \quad (3.6)$$

with A_f determined as

$$A_f = \frac{\mathcal{P}_f}{\Delta_t} \frac{1}{\int_{\kappa_a}^{\kappa_b} \exp\left(-\frac{(\kappa - \kappa_f)^2}{c}\right) d\kappa}. \quad (3.7)$$

In Eq. (3.7), \mathcal{P}_f is the total power input into the system. The functions g_A and g_B in Eq. (3.4) and (3.5) determine the nature of forcing. In this work, force is maintained isotropic by the selection of g_A and g_B as $g_A(\phi) = \sin(2\phi)$ and $g_B(\phi) = \cos(2\phi)$.

The implementation of the forcing scheme is done in spectral space in both INCA and the TurBo. In all our simulations the power input due to forcing \mathcal{P}_f is fixed to unity. Based on the forcing parameters: \mathcal{P}_f and κ_f , one can define a velocity, length, and time scale as follows,

$$U_f \sim \mathcal{P}_f^{1/3} \kappa_f^{-1/3}, \quad L_f \sim \kappa_f^{-1}, \quad \text{and} \quad \tau_f = \mathcal{P}_f^{-1/3} \kappa_f^{-2/3}. \quad (3.8)$$

With velocity and length scaling defined this way, the Reynolds and Rossby number based on forcing parameters can be defined as

$$Re_f = \frac{\mathcal{P}_f^{1/3} \kappa_f^{-4/3}}{\nu}, \quad \text{and} \quad Ro_f = \frac{\mathcal{P}_f^{1/3} \kappa_f^{2/3}}{2\Omega_s}. \quad (3.9)$$

Chapter 4

A Priori Tests

LES require the modelling of the unknown SGS by utilising the knowledge of the resolved quantities. Though we are not primarily interested in the actual magnitudes of the SGS quantities, knowledge of their behaviour is essential in order to accurately solve for the resolved fields. For cases where the solution to the NS equations are available either through DNS or experimental means, the filtered and the SGS quantities can be determined exactly by an explicit filtering operation. This provides the means to compare the actual and the modelled SGS quantities, thereby enabling us to examine the effectiveness of different modelling approaches. These types of a priori tests have already been used in [Lu et al. \(2007\)](#), [da Silva and Pereira \(2007\)](#), [da Silva et al. \(2008\)](#), for example, in the context of turbulence modelling. The current chapter will cover the details of our a priori investigations on forced homogeneous turbulence carried out using DNS data. We examine the level of prediction of the SGS stresses by the linear and the non-linear models that were previously introduced in Sec. 2. The performance of the different models for the terms in the SGS stress and the kinetic energy evolution equations and the validity of some of the (limiting) assumptions in the EASSM of [Marstorp et al. \(2009\)](#) will also be discussed.

4.1 Case description

In order to conduct a priori studies, the solution at steady-state conditions were obtained by running DNS. The behaviour of the resolved and the SGS quantities are examined for three cases, namely, DF: forced with no rotation, DFRw: forced with weak rotation, and DFRs: forced with strong rotation.

The simulations were performed on a cubical box that extends from 0 to 2π with periodic boundary conditions. We have employed a pseudo-spectral method (as mentioned in Sec. 3) with 192^3 grid points. The three dimensional homogeneous random forcing scheme by [Alvelius \(1999\)](#) was used to carry out the simulations with large scale forcing at wavenumber

Case	κ_f	A_f	c_f	Forced modes	Re_f	Ro_f	κ_Ω/κ_c
DF	2	0.8	0.5	0 – 4	88	–	–
DFRw	2	0.8	0.5	0 – 4	88	0.8	0.1
DFRs	2	0.8	0.5	0 – 4	88	0.1	1.7

Table 4.1: Setup of direct numerical simulations conducted for a priori studies.

$\kappa_f = 2$. The simulations were started from a zero-velocity field and run for at least $6\tau_L$ where τ_L is computed from the values at the steady-state¹. In this time, the turbulent kinetic energy reaches a statistical steady-state. The setup of the simulations (and forcing parameters) are provided in Tab. 4.1.

As mentioned in Sec. 2.6.2, as rotation rate increases, it progressively starts to affect the turbulent energy spectrum at larger wavenumbers, until all of the turbulent scales exhibit anisotropy. While conducting the LES on homogeneous turbulence under system rotation, for the cases where the Zeman wavenumber is smaller than the cut-off wavenumber, i.e. $\kappa_\Omega < \kappa_c$, the SGS can be assumed to be relatively unaffected by rotation and so modelling them isotropically does not seem to contradict reality. However, for a rotation rate such that $\kappa_\Omega > \kappa_c$, the SGS also become influenced by the rotation. Therefore, the models employed for the latter case will have to replicate the anisotropic nature of the SGS while also adjusting the dissipation to give the right evolution of the resolved scales. Among the two cases of rotation selected here, DFRw preserves the isotropic nature of the SGS scales, while DFRs renders the SGS anisotropic. This makes DFRs a challenging test case to evaluate the models for the SGS stresses and the different terms in the SGS stress and the kinetic energy evolution equations.

4.2 Results from direct numerical simulation

Before delving into the a priori studies, it is worth taking a moment to look at the DNS results. This will help in illustrating some of the characteristics of rotating turbulence that were previously discussed in Sec. 1.2.

The achievement of steady-state is delayed for the strongly rotating case compared to the isotropic and the weakly rotating cases.

¹ $\tau_L = \langle K_{ss}^{DNS} \rangle_{\mathcal{L}} / \langle \varepsilon_{ss}^{DNS} \rangle_{\mathcal{L}}$, where $\langle K_{ss}^{DNS} \rangle_{\mathcal{L}}$ and $\langle \varepsilon_{ss}^{DNS} \rangle_{\mathcal{L}}$ are the steady-state values of mean turbulent kinetic energy and dissipation, respectively. For all our cases, the mean is same as the volume average.

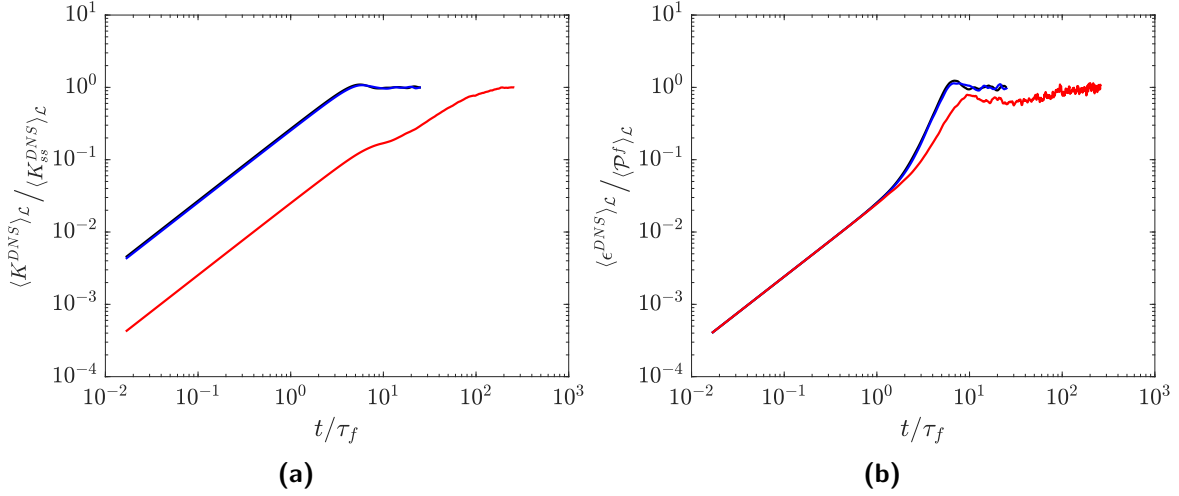


Figure 4.1: Results from direct numerical simulation of forced homogeneous turbulence. Evolution of mean (a) turbulent kinetic energy non-dimensionalised with the value at steady-state and (b) dissipation non-dimensionalised with the power input due to external forcing, plotted against time non-dimensionalised with the forcing time scale. —: DF; —: DFRw; —: DFRs.

Figures 4.1a and 4.1b show the evolution of the mean turbulent kinetic energy $\langle K^{DNS} \rangle_{\mathcal{L}}$ and dissipation $\langle \varepsilon^{DNS} \rangle_{\mathcal{L}}$, respectively for the three cases. The values are plotted against time that is non-dimensionalised with the forcing timescale τ_f as defined in Eq. (3.8). From Fig. 4.1, it can be seen that the evolution of the mean kinetic energy and dissipation are very similar for DF and DFRw, while DFRs shows a highly inhibited growth. It needs to be pointed out that the simulation for DFRs had to be run for ten times longer than DF and DFRw in order to reach a steady state. The suppressed growth of dissipation, which can be clearly seen in Fig. 4.1b causes this delay. As the equilibrium between the power input due to external forcing and the total kinetic energy dissipation is delayed, this reflects as an extended transient for the mean turbulent kinetic energy.

The distribution of energy among the wavenumbers that are parallel and perpendicular to the axis to rotation displays anisotropy.

One of the characteristics of rotating turbulence is that it gives rise to a directional dependence of turbulence, thereby leading to anisotropy. Figure 4.2 shows the one-dimensional energy spectrum as a function of κ_x , κ_y , and κ_z for DF and DFRs. The corresponding spectrum for DFRw is very similar to the DF and hence not shown here. In Fig. 4.2a, we can see that the 1-D energy spectrum is identical for κ_x , κ_y , κ_z , which indicates the isotropic nature of DF. On the other hand, the anisotropic nature of DFRs is evident from Fig. 4.2b where, there is a clear difference in the distribution of energy along the wavenumbers in the direction parallel to the rotation axis, κ_z when compared to the distribution along the wavenumbers that are perpendicular to the rotation axis, κ_x and κ_y . It is also interesting to note that when arranged as a function of $\kappa_{\perp} = (\kappa_x^2 + \kappa_y^2)^{1/2}$, and $\kappa_{\parallel} = \|\kappa_z\|$ modes, we find a scaling of $\hat{E}(\kappa_{\perp})$ with $\kappa_{\perp}^{-5/2}$ for the strongly rotating case as predicted by Galtier (2003).

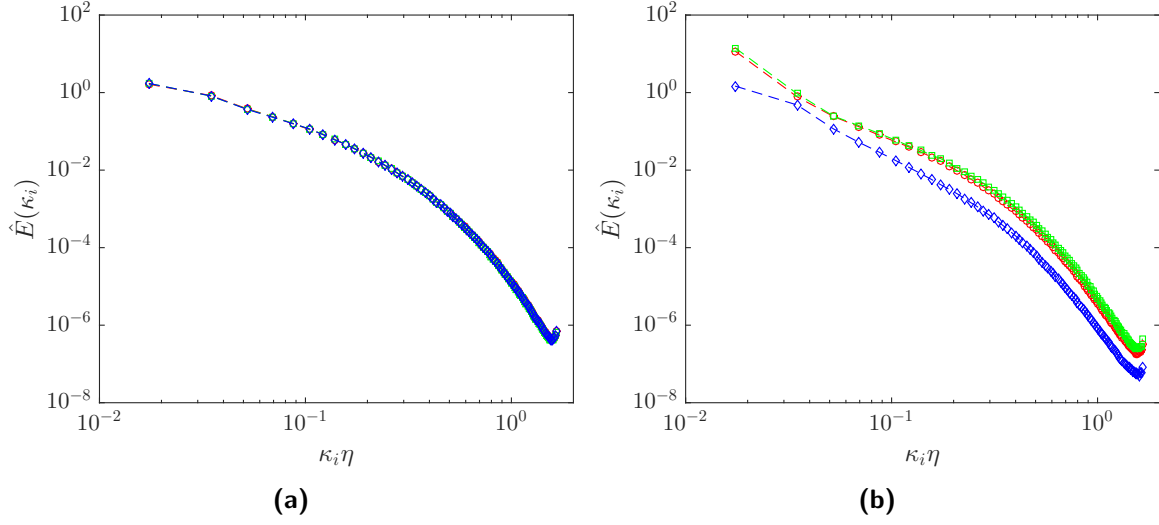


Figure 4.2: Time averaged 1-D spectrum for the (a) DF and (b) DFRs. — $\hat{E}(\kappa_x)$; — $\hat{E}(\kappa_y)$; — $\hat{E}(\kappa_z)$.

The energy spectrum for the strongly rotating case exhibits a scaling that is different from the Kolmogorov scaling law of $\kappa^{-5/3}$ that we observe for the isotropic case.

We observe an alternate scaling of κ^{-2} for the intermediate scales in the strongly rotating case. This can be observed by plotting the compensated energy spectrums as shown in Fig. 4.3. We can clearly see that the time averaged spectrum for DFRs agrees better with a κ^{-2} scaling in Fig. 4.3b than $\kappa^{-5/3}$ scaling in Fig. 4.3a. It is also in-line with the findings in the literature (Baroud et al. (2002), Zhou (1995)). For DF and DFRw, on the other hand, we find that the energy spectrums adhere to the Kolmogorov scaling law showing a better agreement to $\kappa^{-5/3}$ scaling as shown in Fig. 4.2a.

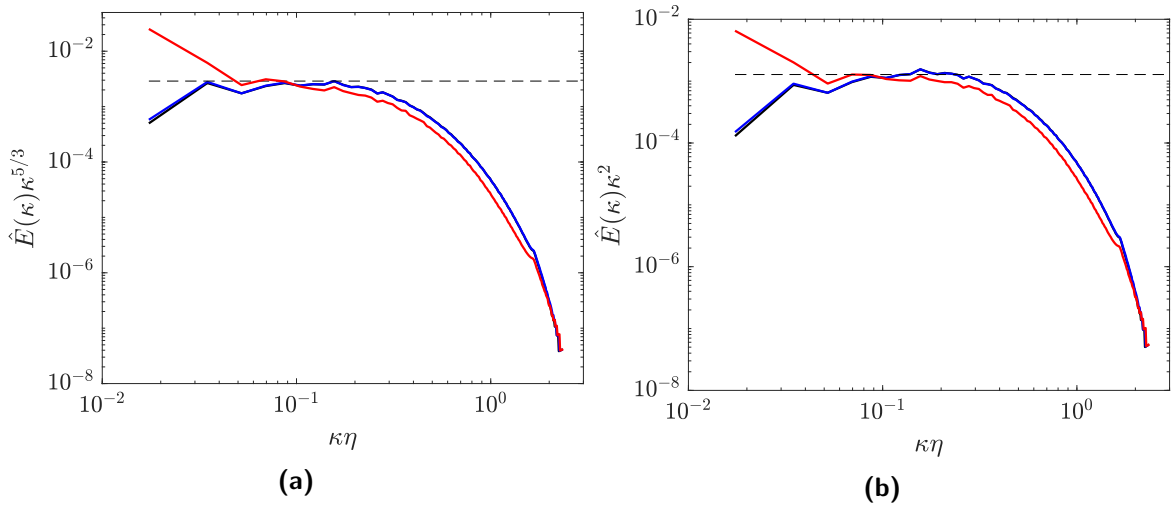


Figure 4.3: Compensated turbulent energy spectrum obtained for DF, DFRw, and DFRs compensated with (a) $\kappa^{5/3}$ and (b) κ^2 . — $\hat{E}(\kappa_x)$; — $\hat{E}(\kappa_y)$; — $\hat{E}(\kappa_z)$.

It needs to be pointed out that the evolution of turbulence in these computations is not free from the effect of the boundary conditions. As rotation stretches the vortices along the axis of rotation, the eddies grow to sizes comparable to the domain size and comes under the its own influence due to the periodic boundary condition. While this will impact the results, the effect of boundary condition and domain size on turbulence evolution will not be a focus of the current thesis as we believe that these would have a similar impact in LES as in DNS.

4.3 Tools for a priori analysis

For the purpose of the a priori analyses, the steady-state solution at the last time step for the three cases are used. The filtered and the SGS quantities were computed using the box filter with cut-off wavenumber $\kappa_c = 10$. Using the filtered values, the different quantities in SGS stress and kinetic energy evolution equations were modelled and compared with the actual SGS fields. One of the tools used for quantifying the modelling performance is the correlation coefficient $\hat{\rho}$. The correlation coefficient between two scalars, say α and β can be computed as

$$\hat{\rho}(\alpha, \beta) = \frac{\sum_{i=1}^n (\alpha_i - \bar{\alpha})(\beta_i - \bar{\beta})}{\sqrt{\sum_{i=1}^n (\alpha_i - \bar{\alpha})^2} \sqrt{\sum_{i=1}^n (\beta_i - \bar{\beta})^2}}, \quad (4.1)$$

where the overbar represents an ensemble average which in our case is the same as volume average $\langle \cdot \rangle_{\mathcal{L}}$, and n denotes the total number of points in the domain. Correlation coefficients measure the level of linear correlation that exists between two quantities that are being compared. A value of $\hat{\rho} = 0$ indicates that there exists no linear relationship between the two variables considered, while a correlation coefficient of +1 would imply a perfect positive linear dependency. Therefore, the effectiveness of a model for an SGS quantity, say α , will be inferred by how close the value of $\hat{\rho}(\alpha_{modelled}, \alpha_{actual})$ is to +1.

In addition to this, we also use n^{th} -moments (Schuster (2016)) to examine the statistics related to (localised) magnitude of the different actual and modelled quantities. The second, the third, and the fourth moments will be used for this purpose. The second moment: variance signifies the extent of deviation of a quantity about the mean, i.e. it can be used to measure the local intensity of the fluctuations (da Silva and Pereira (2007)). It is defined as

$$var(\alpha) = \frac{\sum_{i=1}^n (\alpha_i - \bar{\alpha})^2}{n}. \quad (4.2)$$

The third and the fourth moments are namely, skewness and flatness. These statistics describe the shape of the probability density functions (PDFs). The skewness indicates the lack of symmetry of the PDF while the flatness (or kurtosis) provides a measure of the intermittency in their values. High flatness values indicates that the PDF is heavy-tailed, i.e. presence of high peaks in the signal that are intermittently distributed. For a Gaussian distribution, the skewness is 0 and the kurtosis is 3. Therefore, these two quantities can be also interpreted

as the extent of departure from a Gaussian distribution. For a variable, say α , the skewness and the flatness are normalised using the variance and are defined as

$$skewness(\alpha) = \frac{\frac{1}{n} \sum_{i=1}^n (\alpha_i - \bar{\alpha})^3}{\left(\frac{1}{n} \sum_{i=1}^n (\alpha_i - \bar{\alpha})^2\right)^{3/2}}; \quad flatness(\alpha) = \frac{\frac{1}{n} \sum_{i=1}^n (\alpha_i - \bar{\alpha})^4}{\left(\frac{1}{n} \sum_{i=1}^n (\alpha_i - \bar{\alpha})^2\right)^2}. \quad (4.3)$$

By using these statistical tools, the effectiveness of the DSM, the dynamic and the non-dynamic EASSMs can be tested for the different cases. In addition, the analysis will also be extended to the modelling approaches for the terms in the ‘simplified’ equation for SGS stresses (Eq. (2.12)) and the evolution equation for SGS kinetic energy. Thereby, a better understanding of the weaknesses and the limitations of the modelling approaches for each term can be obtained.

4.4 Performance of the linear and the non-linear models for SGS stresses

The representation of SGS stress by DSM, non-dynamic and dynamic EASSMs will be the starting point of our a priori analysis. We compare the normal SGS stress components τ_{11} and τ_{33} , and the cross terms τ_{12} , and τ_{13} for cases: DF, DFRw, and DFRs. Since rotation is imposed in the z -direction, the SGS stress components in the xy -plane are relatively indifferentiable in the sense that rotation does not affect the wavenumbers κ_x and κ_y differently. Thus the choice of components for analysis is expected to give a holistic picture. Figure 4.4a shows the level of correlation between the actual and the modelled SGS stress anisotropy for DSM. It is to be noted that in order to maintain the value of dynamic constant positive, it is determined by averaging the numerator and denominator in Eq. (2.34) over the entire volume due to homogeneity. Therefore, the values of correlations that are shown in Fig. 4.4a are the same for standard Smagorinsky model as well. It can be seen from Fig. 4.4a that for DF and DFRw, DSM records similar levels of correlation, while for DFRs, the correlation coefficients for all components of τ_{ij}^d drop to less than 20%. This behaviour was expected as the setup of the DFRs is such that the SGS scales are influenced by rotation ($\kappa_\Omega > \kappa_c$). The resulting anisotropic SGS scales are not efficiently captured by the Smagorinsky model.

On the other hand, the dynamic and the non-dynamic EASSMs give a better overall correlation for τ_{ij} when compared to the DSM. The correlation coefficients corresponding to the dynamic and the non-dynamic EASSMs for τ_{ij} are plotted in Fig. 4.4b and 4.4c, respectively. In the case of DF and DFRw, the correlation coefficients are very similar, whereas, for DFRs, it can be seen that although strong rotation deteriorates the modelling of the cross terms, i.e. off-diagonal elements of τ_{ij} , the spatial variation of normal components τ_{ii} are still well predicted. The addition of a non-linear term (tensor $T_{ij}^{(2)}$) in the formulation of τ_{ij} makes the EASSMs better capable of capturing the dynamics of τ_{ij} compared to the DSM. Among the models that are compared here, the dynamic EASSM (shown in Fig. 4.4c) gives the best tensor level correlation for the SGS stresses.

We now move on to examining the modelling of the SGS kinetic energy production by the

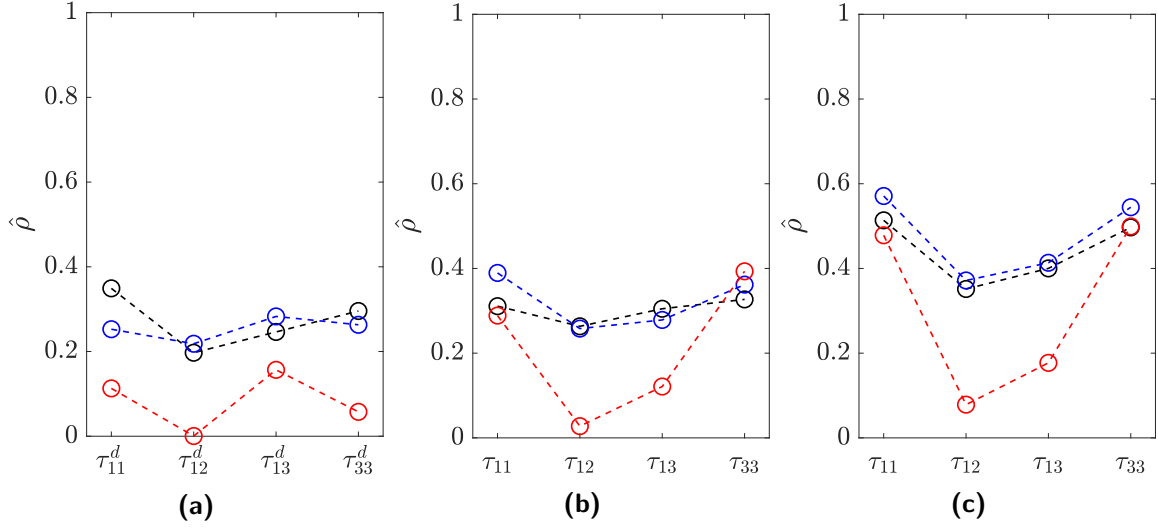


Figure 4.4: Correlation coefficients for the normal and cross terms of the modelled and the actual SGS stress (a) anisotropy for DSM, (b) for non-dynamic EASSM, and (c) for dynamic EASSM. ---○ DF; ---○ DFRw; ---○ DFRs.

different models. The modelled SGS kinetic energy production gives an estimate of the mean energy drained by the models from the resolved scales. The coefficients of the measured correlation between the actual and the modelled \mathcal{P} are shown in Tab. 4.2. DSM records the highest level of correlation for all cases, very comparable with dynamic EASSM. The deterioration of the correlation levels for DFRs is very similar for all models. For the case of strong rotation, all models provide only about 15 ~ 20% correlation with the actual SGS kinetic energy production. In the formulation of EASSM, among the two tensors $T_{ij}^{(1)}$ and $T_{ij}^{(2)}$ used to model the SGS stresses, only $T_{ij}^{(1)}$ contributes to \mathcal{P} , while $T_{ij}^{(2)}$ vanishes as $\left(\langle S_{ik}^* \rangle \langle \Omega_{kj}^* \rangle - \langle \Omega_{ik}^* \rangle \langle S_{kj}^* \rangle\right) \langle S_{ij} \rangle = 0$. Therefore, the difference in the correlation coefficients for production that we observe for the different models, is entirely due to the scalar coefficients of the strain rate tensor, i.e. eddy viscosity in case of DSM and $G^{(1)} k_{sgs}^2 / \varepsilon$ in the case of EASSM. We see that the DSM and the dynamic EASSM give very similar levels of correlation, which are higher than the values for non-dynamic EASSM for all cases. The difference in the correlation values between dynamic and non-dynamic EASSMs for \mathcal{P} can be attributed to the poor modelling of k_{sgs} in the non-dynamic version compared to the dynamic version. These values are also shown in Tab. 4.2 where we see the reduction in the correlation coefficients for SGS kinetic energy for the non-dynamic EASSM compared to the dynamic EASSM for all cases.

In addition to correlation coefficients, we also compare the third moment, i.e. skewness of the PDFs for the modelled and the actual SGS stress and kinetic energy production. This will further emphasize the differences in the evolution of SGS quantities in isotropic and strongly rotating conditions and help us to understand the limitations of the models. As the results we have observed so far for DFw does not differ appreciably from DF, we limit this part of the analysis to cases DF and DFRs only. We compare the only trace elements of the modelled and the actual SGS stress tensor. The corresponding values are tabulated in Tab. 4.3. The

Model	\mathcal{P}			k_{sgs}		
	DF	DFR _w	DFR _s	DF	DFR _w	DFR _s
(Dyn.) Smagorinsky	0.78	0.76	0.18	-	-	-
Non-dyn. EASSM	0.61	0.61	0.13	0.33	0.45	0.34
Dyn. EASSM	0.75	0.74	0.18	0.60	0.67	0.53

Table 4.2: Coefficients of the measured correlation between modelled and actual SGS kinetic energy and production for DSM, non-dynamic, and dynamic EASSMs for cases DF, DFR_w, and DFR_s.

Model	\mathcal{P}		τ_{11}		τ_{22}		τ_{33}	
	DF	DFR _s	DF	DFR _s	DF	DFR _s	DF	DFR _s
DNS	3.65	0.65	3.27	8.16	2.95	10.17	2.75	4.25
Dyn. Smagorinsky	3.39	4.91	-	-	-	-	-	-
Non-dyn. EASSM	4.61	12.07	2.91	3.96	2.81	3.79	3.31	4.01
Dyn. EASSM	3.33	2.41	2.03	2.22	1.91	2.09	2.18	2.19

Table 4.3: Skewness of the modelled and the actual SGS kinetic energy production and normal SGS stresses for DSM, non-dynamic, and dynamic EASSMs for cases DF, DFR_w, and DFR_s.

normal SGS stresses become increasingly positively skewed with rotation. The dynamic and non-dynamic EASSMs, however, do not capture this behaviour well, as we see in Tab. 4.3 that the skewness of the modelled (normal) SGS stresses does not increase appreciably as observed in the DNS.

For the actual SGS kinetic energy production obtained from the DNS, the variation of skewness with rotation is as expected. We see in Tab. 4.3, that the Skewness obtained from DNS reduces from 3.7 in DF to 0.7 in DFR_s. As mentioned earlier, rotation increases the amount of backscatter as a result of which the net production becomes suppressed. The SGS production becomes increasingly negative (locally) and thereby the corresponding PDF tends towards symmetry. In the limit $Ro \rightarrow 0$ we expect the SGS production to become 0. In this limit, the total forward cascade (from resolved to SGS) is expected to balance the total amount of backscatter (SGS to resolved scales) and the resulting PDF for the SGS kinetic energy production would show symmetry, i.e. skewness = 0. For DF, the SGS kinetic energy production modelled with the dynamic EASSM and the DSM shows values of skewness that are very close to the corresponding skewness measured from the DNS. The non-dynamic EASSM however, is (slightly) more positively skewed than the other models. The difference is more

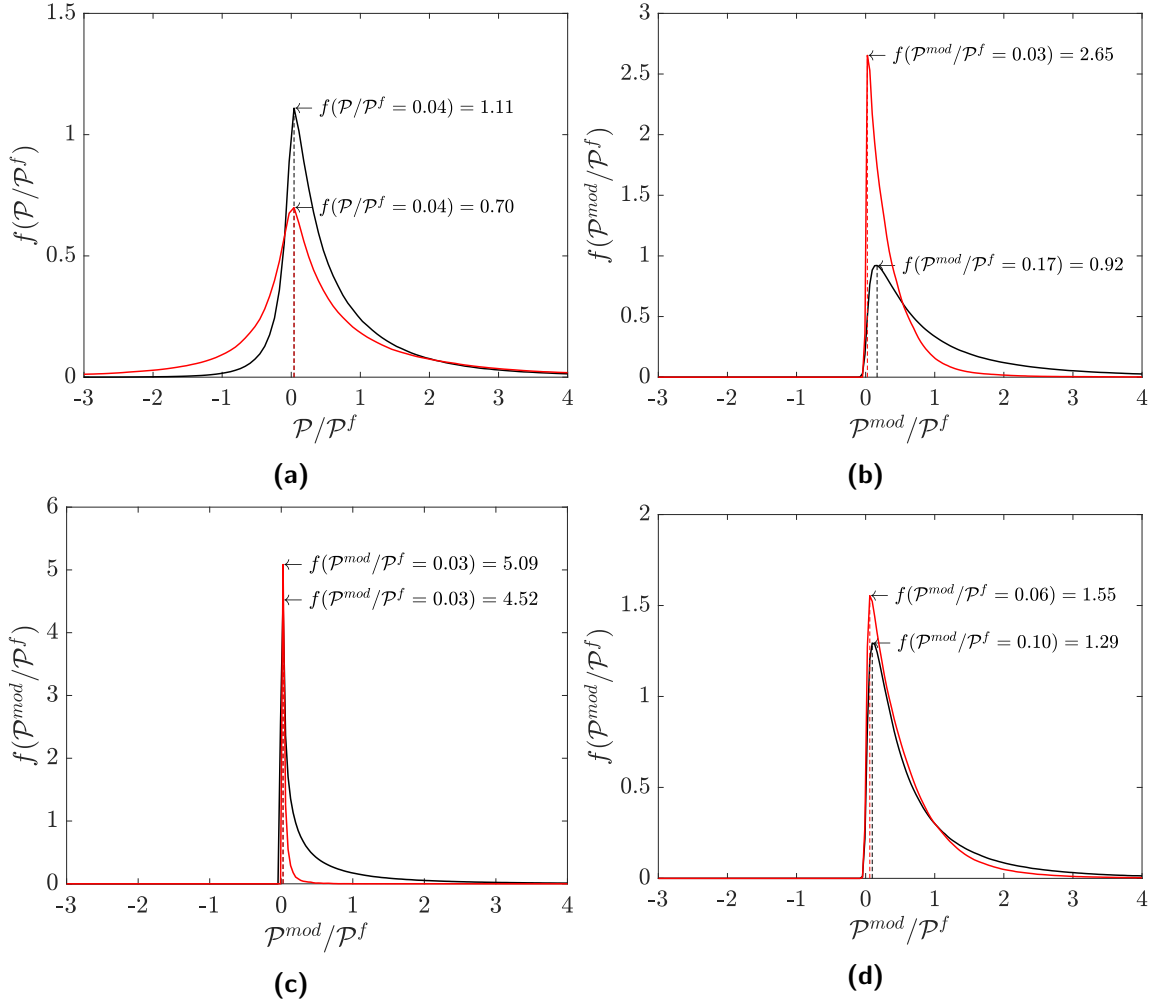


Figure 4.5: Probability density function f of the SGS kinetic energy production. The PDFs correspond to (a) DNS, (b) DSM, (c) non-dynamic EASSM, and (d) dynamic EASSM. — DF; — DFRs.

evident for DFRs, for which all models overpredict the skewness in modelled value of \mathcal{P} , with the non-dynamic EASSM showing the highest level of skewness.

A better understanding of the skewness values for the actual and the modelled SGS kinetic energy production in Tab. 4.3 can be gained by looking at the corresponding PDFs shown in Fig. 4.5. The PDF of the actual SGS kinetic energy production in Fig. 4.5a indicates an increased amount of backscatter for DFRs as the PDF becomes heavy left tailed, i.e. it accumulates more negative values for DFRs when compared to DF. As a result we see that the PDF for \mathcal{P} is more symmetry for DFRs than for DF. On the other hand, the DSM and the EASSMs model SGS kinetic energy production in strictly positive manner, thus having an infimum at zero. As the total (modelled) SGS kinetic energy production is suppressed because of rotation, this consequently leads to a higher peak in the PDF that we see for all models in Fig. 4.5b, 4.5c, and 4.5d. The modification in the EASSMs for rotation (Eq. (2.44)) suppresses the production which is more evident for the non-dynamic version (in Fig. 4.5c)

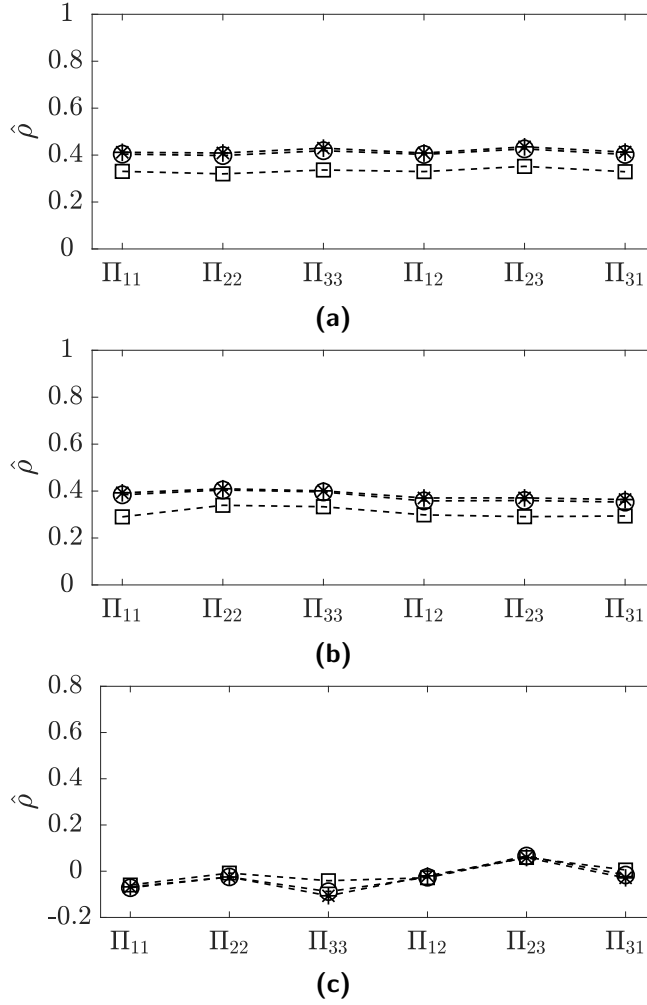


Figure 4.6: Correlation coefficients of the modelled and the actual pressure-strain for the LRR and SSG models obtained for the (a) DF, (b) DFRs, (c) and DFRw. *-LRR-IP; o-LRR-QI; □-SSG

than the dynamic version (in Fig. 4.5d).

4.5 Modelling of the pressure-strain term

As mentioned earlier, the modelling of the pressure-strain term is crucial to an EASSM. Unlike other quantities in the SGS stress evolution equation, the pressure-strain term contains only an anisotropic part and is generally modelled as a function of the anisotropy of SGS kinetic energy production and dissipation. From the discussion thus far, we see that, with EASSMs, while the normal components maintain higher levels of correlation, the cross terms are poorly correlated for the case DFRs. A natural starting point in understanding the behaviour of the EASSM for different cases is the examination of the modelling approaches taken for the constituent elements of the ‘simplified’ SGS equation (Eq. (2.16)).

The correlation coefficients for the (complete) pressure-strain term using the three models, LRR-IP, LRR-QI, and SSG, are plotted in Fig. 4.6 for all cases. Both linear LRR models (QI and IP), behave very much alike. From Fig. 4.6a, and 4.6b, it can be seen that the correlation coefficients for the SSG model is slightly lower than for the LRR models in DF and DFRw. Nevertheless, we can see that all models provide 30 – 40% correlation for DF and DFRw. On the other hand, for DFRs, it can be seen from Fig. 4.6c that all the modelled components (of Π_{ij}) seem to be almost completely uncorrelated with the actual quantities.

The cause for deterioration of pressure-strain models for DFRs can be further investigated by analysing the rapid or slow terms that constitute the total pressure-strain. The modelling of the pressure-strain term has been extensively investigated in the context of RANS (Townsend (1954), Lumley (1979), Speziale et al. (1992), Choi and Kang (2002)). The insights gained through these analyses are then directly applied to LES as well. However, the expressions for the rapid and slow terms, and the effectiveness of the models (for rapid and slow parts) specifically for LES is not found in Literature. Therefore, we first start by deriving the expressions for rapid and slow pressure, from which we can move on to computing the actual slow and rapid pressure-strain terms. The decomposition of pressure into rapid and slow terms can be done using the Poisson equation, which reads

$$\frac{1}{\rho} \frac{\partial^2 p}{\partial x_i \partial x_i} = - \frac{\partial^2 u_i u_j}{\partial x_i \partial x_j}. \quad (4.4)$$

Filtering Eq. (4.4) and assuming that the filter commutes with the differential operator leads to

$$\begin{aligned} \frac{1}{\rho} \frac{\partial^2 \langle p \rangle}{\partial x_i \partial x_i} &= - \frac{\partial^2 \langle u_i u_j \rangle}{\partial x_i \partial x_j} \\ &= - \underbrace{\frac{\partial^2 \langle \langle u_i \rangle \langle u_j \rangle \rangle}{\partial x_i \partial x_j} - \frac{\partial^2 \langle \langle u_i \rangle u'_j \rangle}{\partial x_i \partial x_j} - \frac{\partial^2 \langle u'_i \langle u_j \rangle \rangle}{\partial x_i \partial x_j}}_{\text{Rapid}} - \underbrace{\frac{\partial^2 \langle u'_i u'_j \rangle}{\partial x_i \partial x_j}}_{\text{Slow}}. \end{aligned} \quad (4.5)$$

Equation (4.5) is the Poisson equation for the resolved pressure field, where u'_i is the residual velocity, $u'_i = u_i - \langle u_i \rangle$. The first three terms on the RHS are identified as the ‘rapid’ contribution while the fourth term on the RHS is defined as the ‘slow’ contribution. The nomenclature of rapid and slow follow from the RANS analogy. Terms that contain resolved quantities in its definition are termed as rapid quantities while the quantities that are purely defined by the residual quantities are called the slow terms (Marstorp et al. (2009)). In order to find the corresponding equation for the residual pressure, i.e. p' , Eq. (4.5) is subtracted from Eq. (4.4). This operation results in a Poisson equation for residual pressure, and it is obtained as follows:

$$\frac{1}{\rho} \frac{\partial^2 p}{\partial x_i \partial x_i} - \frac{1}{\rho} \frac{\partial^2 \langle p \rangle}{\partial x_i \partial x_i} = - \frac{\partial^2 u_i u_j}{\partial x_i \partial x_j} + \frac{\partial^2 \langle \langle u_i \rangle \langle u_j \rangle \rangle}{\partial x_i \partial x_j} + \frac{\partial^2 \langle \langle u_i \rangle u'_j \rangle}{\partial x_i \partial x_j} + \frac{\partial^2 \langle u'_i \langle u_j \rangle \rangle}{\partial x_i \partial x_j} + \frac{\partial^2 \langle u'_i u'_j \rangle}{\partial x_i \partial x_j}.$$

Expanding $u = \langle u \rangle + u'$,

$$\begin{aligned}
\frac{1}{\rho} \frac{\partial^2 p'}{\partial x_i \partial x_i} &= -\frac{\partial^2 (\langle u_i \rangle + u'_i) (\langle u_j \rangle + u'_j)}{\partial x_i \partial x_j} + \frac{\partial^2 \langle \langle u_i \rangle \langle u_j \rangle \rangle}{\partial x_i \partial x_j} + \frac{\partial^2 \langle \langle u_i \rangle u'_j \rangle}{\partial x_i \partial x_j} + \frac{\partial^2 \langle u'_i \langle u_j \rangle \rangle}{\partial x_i \partial x_j} \\
&\quad + \frac{\partial^2 \langle u'_i u'_j \rangle}{\partial x_i \partial x_j} \\
&= -\frac{\partial^2 \langle u_i \rangle \langle u_j \rangle}{\partial x_i \partial x_j} - \frac{\partial^2 \langle u_i \rangle u'_j}{\partial x_i \partial x_j} - \frac{\partial^2 u'_i \langle u_j \rangle}{\partial x_i \partial x_j} - \frac{\partial^2 u'_i u'_j}{\partial x_i \partial x_j} + \frac{\partial^2 \langle \langle u_i \rangle \langle u_j \rangle \rangle}{\partial x_i \partial x_j} \\
&\quad + \frac{\partial^2 \langle \langle u_i \rangle u'_j \rangle}{\partial x_i \partial x_j} + \frac{\partial^2 \langle u'_i \langle u_j \rangle \rangle}{\partial x_i \partial x_j} + \frac{\partial^2 \langle u'_i u'_j \rangle}{\partial x_i \partial x_j}
\end{aligned} \tag{4.6}$$

$$\begin{aligned}
&= \left. \begin{aligned} &-\frac{\partial^2 \langle u_i \rangle \langle u_j \rangle}{\partial x_i \partial x_j} - \frac{\partial^2 \langle u_i \rangle u'_j}{\partial x_i \partial x_j} - \frac{\partial^2 u'_i \langle u_j \rangle}{\partial x_i \partial x_j} \\ &+ \frac{\partial^2 \langle \langle u_i \rangle \langle u_j \rangle \rangle}{\partial x_i \partial x_j} + \frac{\partial^2 \langle \langle u_i \rangle u'_j \rangle}{\partial x_i \partial x_j} + \frac{\partial^2 \langle u'_i \langle u_j \rangle \rangle}{\partial x_i \partial x_j} \end{aligned} \right\} \text{Rapid} \\
&\quad + \left. \begin{aligned} &\frac{\partial^2 \langle u'_i u'_j \rangle}{\partial x_i \partial x_j} - \frac{\partial^2 u'_i u'_j}{\partial x_i \partial x_j} \end{aligned} \right\} \text{Slow}
\end{aligned} \tag{4.7}$$

Equation (4.7) is the Poisson equation for the residual pressure that can also be defined as having two contributions. The first six terms on the RHS of Eq. (4.7) are the ‘rapid’ contributions while the last two terms on the RHS represents the ‘slow’ contribution. From Eq. (4.5) and (4.7), we can construct the Poisson equation for the unfiltered pressure in terms of rapid (p^r) and slow (p^s) contributions as

$$\begin{aligned}
\frac{1}{\rho} \frac{\partial^2 p^r}{\partial x_i \partial x_i} &= \frac{1}{\rho} \frac{\partial^2 \langle p^r \rangle}{\partial x_i \partial x_i} + \frac{1}{\rho} \frac{\partial^2 p^{r'}}{\partial x_i \partial x_i} \\
&= -\frac{\partial^2 \langle \langle u_i \rangle \langle u_j \rangle \rangle}{\partial x_i \partial x_j} - \frac{\partial^2 \langle \langle u_i \rangle u'_j \rangle}{\partial x_i \partial x_j} - \frac{\partial^2 \langle u'_i \langle u_j \rangle \rangle}{\partial x_i \partial x_j} - \frac{\partial^2 \langle u_i \rangle \langle u_j \rangle}{\partial x_i \partial x_j} - \frac{\partial^2 \langle u_i \rangle u'_j}{\partial x_i \partial x_j} \\
&\quad - \frac{\partial^2 u'_i \langle u_j \rangle}{\partial x_i \partial x_j} + \frac{\partial^2 \langle \langle u_i \rangle \langle u_j \rangle \rangle}{\partial x_i \partial x_j} + \frac{\partial^2 \langle \langle u_i \rangle u'_j \rangle}{\partial x_i \partial x_j} + \frac{\partial^2 \langle u'_i \langle u_j \rangle \rangle}{\partial x_i \partial x_j} \\
&= -\frac{\partial^2 \langle u_i \rangle \langle u_j \rangle}{\partial x_i \partial x_j} - \frac{\partial^2 \langle u_i \rangle u'_j}{\partial x_i \partial x_j} + \frac{\partial^2 u'_i \langle u_j \rangle}{\partial x_i \partial x_j},
\end{aligned} \tag{4.8}$$

$$\begin{aligned}
\frac{1}{\rho} \frac{\partial^2 p^s}{\partial x_i \partial x_i} &= \frac{1}{\rho} \frac{\partial^2 \langle p^s \rangle}{\partial x_i \partial x_i} + \frac{1}{\rho} \frac{\partial^2 p^{s'}}{\partial x_i \partial x_i} \\
&= -\frac{\partial^2 \langle u'_i u'_j \rangle}{\partial x_i \partial x_j} + \frac{\partial^2 \langle u'_i u'_j \rangle}{\partial x_i \partial x_j} - \frac{\partial^2 u'_i u'_j}{\partial x_i \partial x_j} \\
&= -\frac{\partial^2 u'_i u'_j}{\partial x_i \partial x_j}.
\end{aligned} \tag{4.9}$$

The rapid and slow parts of pressure obtained by solving Eqs. (4.8) and (4.9), respectively, have different contributions to the total pressure strain term. These contributions will form the rapid and slow pressure-strain terms for LES, which are represented as Π_{ij}^r and Π_{ij}^s , respectively. Following our convention, in LES, these quantities read

$$\begin{aligned}\chi\left(\frac{p}{\rho}, \frac{\partial u_i}{\partial x_j}\right) &= \chi\left(\frac{(p_r + p_s)}{\rho}, \frac{\partial u_i}{\partial x_j}\right) \\ &= \chi\left(\frac{p_r}{\rho}, \frac{\partial u_i}{\partial x_j}\right) + \chi\left(\frac{p_s}{\rho}, \frac{\partial u_i}{\partial x_j}\right)\end{aligned}$$

$$\Pi_{ij}^r + \Pi_{ij}^s = \underbrace{\chi\left(\frac{p_r}{\rho}, \frac{\partial u_i}{\partial x_j}\right) + \chi\left(\frac{p_r}{\rho}, \frac{\partial u_j}{\partial x_i}\right)}_{\text{Rapid}} + \underbrace{\chi\left(\frac{p_s}{\rho}, \frac{\partial u_i}{\partial x_j}\right) + \chi\left(\frac{p_s}{\rho}, \frac{\partial u_j}{\partial x_i}\right)}_{\text{Slow}} \quad (4.10)$$

By evaluating the slow and rapid terms in Eq. (4.10) using DNS data, we can effectively assess the separate modelling of these two quantities. Our understanding of the slow and rapid pressure-strain terms in RANS is that the slow term dominates over the rapid term in cases where the mean strain rates are negligible. Conversely, the rapid term dictates the dynamics of the total pressure-strain term in cases where turbulence is subject to rapid distortions. Based on this reasoning, the LRR and SSG models combine the separate models for the slow and rapid terms into their respective final expressions, which when adapted for LES can be expressed as in Eq. (2.19) to (2.21). In order to understand the overall representation of the pressure-strain term, we break them down into their constituting expressions for the rapid and slow terms. In both LRR-IP and QI models, the slow term is modelled in the same way: using Rotta's expression (Eq. (2.17)), while the SSG model introduces additional non-linear terms in the expression. The model for the slow term in the LRR and the SSG models read,

$$\text{LRR (IP and QI)} : \Pi_{ij}^s = -C_R \varepsilon a_{ij}, \quad (4.11)$$

$$\text{SSG} : \Pi_{ij}^s = -\frac{(C_1 \varepsilon + C_1^* \mathcal{P})}{2} a_{ij} + \frac{C_2}{4} \varepsilon \left(a_{ik} a_{kj} - \frac{1}{3} a_{mn} a_{mn} \delta_{ij} \right). \quad (4.12)$$

The IP and QI models of LRR differ in their modelling of the rapid term. The model expression for the rapid term in LRR-QI, IP, and SSG, respectively read,

$$\begin{aligned}\text{LRR-QI} : \Pi_{ij}^r &= \frac{4}{5} k_{sgs} \langle S_{ij} \rangle + \frac{3}{11} (2 + 3C_2) k_{sgs} \left(\langle S_{ik} \rangle a_{kj} + a_{ik} \langle S_{kj} \rangle \right. \\ &\quad \left. - \frac{2}{3} \langle S_{kl} \rangle a_{kl} \delta_{ij} \right) + \frac{1}{11} (10 - 7C_2) k_{sgs} \left(\langle \Omega_{ik} \rangle a_{kj} - a_{ik} \langle \Omega_{kj} \rangle \right),\end{aligned} \quad (4.13)$$

$$\begin{aligned}\text{LRR-IP} : \Pi_{ij}^r &= \frac{4}{3} C_2 k_{sgs} \langle S_{ij} \rangle + C_2 k_{sgs} \left(\langle S_{ik} \rangle a_{kj} + a_{ik} \langle S_{kj} \rangle - \frac{2}{3} \langle S_{kl} \rangle a_{kl} \delta_{ij} \right) \\ &\quad + C_2 k_{sgs} \left(\langle \Omega_{ik} \rangle a_{kj} - a_{ik} \langle \Omega_{kj} \rangle \right),\end{aligned} \quad (4.14)$$

$$\begin{aligned}\text{SSG} : \Pi_{ij}^r &= \frac{(2C_3 - C_3^* I_a^{1/2})}{2} k_{sgs} \langle S_{ij} \rangle + \frac{C_4}{2} k_{sgs} \left(\langle S_{ik} \rangle a_{kj} + a_{ik} \langle S_{kj} \rangle \right. \\ &\quad \left. - \frac{2}{3} \langle S_{kl} \rangle a_{kl} \delta_{ij} \right) + \frac{C_5}{2} k_{sgs} \left(\langle \Omega_{ik} \rangle a_{kj} - a_{ik} \langle \Omega_{kj} \rangle \right).\end{aligned} \quad (4.15)$$

The correlation between the modelled terms in Eq. (4.11) to (4.15) and the actual terms in Eq. (4.10) is shown in Fig. 4.7 for the different components. Since the correlation coefficients of the total pressure-strain models for DFRw (in Fig. 4.6b) are not very different from DF (in Fig. 4.6a), we only compare DF and DFRs in this analysis. In Fig. 4.7a, we can see that the correlation coefficients obtained using different models for the rapid term is very similar to the values obtained for the total pressure-strain term (in Fig. 4.6a and 4.6c). For DF, all models show 30 – 40% correlation for the different components of the rapid term, with the two LRR models showing almost identical values of correlation. On the other hand, for DFRs, all models for rapid pressure-strain become uncorrelated with the actual quantity. In the modelling for the slow term, Fig. 4.7b shows that LRR models gives similar levels of correlation as non-linear SSG model for DF. In addition, although the deterioration of the correlation coefficients under strong rotation is observed for the SSG model, linear LRR models preserves the correlation for the trace elements which are in the range of 10 – 20%. This indicates that under strong rotation the role of slow pressure-strain term in transferring energy between the different components of τ_{ii} is captured better by the LRR models than the SSG model.

At this point, we observe that, if we consider the modelling of the trace elements by the LRR models, in DFRs, the deterioration of correlation coefficients for the rapid term is much more than the corresponding deterioration for the slow stem (as seen in Fig. 4.7). As a result, the (poor) modelling of Π_{ij}^r seems to be the primary cause for the deterioration of correlation values for Π_{ij} in DFRs. Therefore, the modelling of the rapid terms in the pressure-strain model (both LRR and SSG) for strongly rotating cases requires some attention. However, this is not within the scope of this work and hence will not be examined further. Given the choice between the three models in LES, based entirely on the correlation values for the different cases studied, it seems that the linear LRR models are better suited for isotropic and weakly rotating cases than the non-linear SSG model.

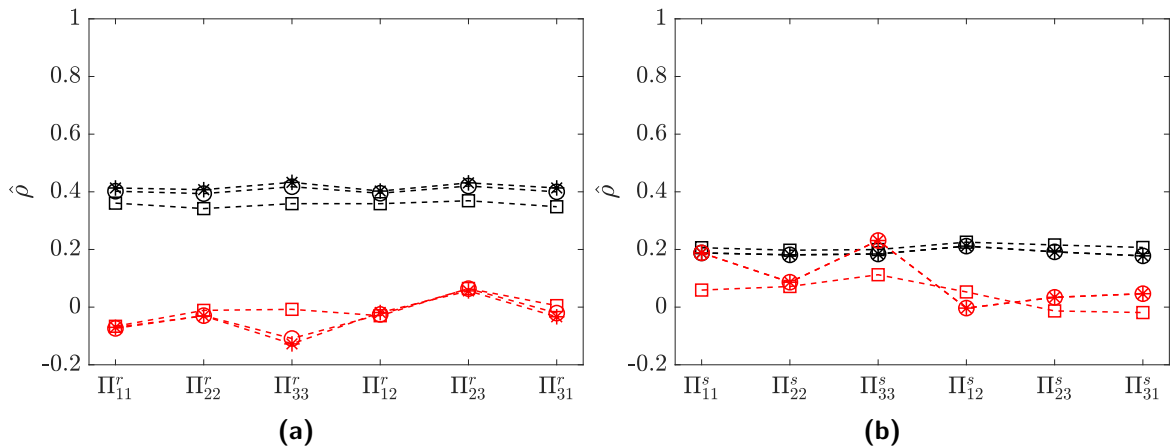


Figure 4.7: Correlation coefficients of the models for (left) rapid and (right) slow pressure-strain terms for the cases: *Black*-DF, *red*-DFRs. *-LRR-IP; o-LRR-QI; □-SSG.

4.6 Modelling of the subgrid-scale kinetic energy equation

The modelling of the SGS stress and the pressure-strain term by different models were discussed so far. Now we move on to analysing the modelling of the terms in SGS kinetic energy evolution equation. For determining k_{sgs} , Marstorp et al. (2009) derive an algebraic expression (Tab. 2.3). The formulation for k_{sgs} shown in Tab. 2.3 rests on the assumption that the SGS kinetic energy production and dissipation are in perfect balance. The validity of this assumption will be examined in the next section. However, if we avoid this assumption, instead of using an algebraic expression for the SGS kinetic energy, its evolution can be traced through a transport equation (Eq. (2.14)). In this approach, the transport and dissipation terms in the evolution equation need to be modelled additionally. The models employed by Yoshizawa and Horiuti (1985) in obtaining a modelled evolution equation for SGS kinetic energy (Eq. (2.40)) and the effectiveness of these models for strongly rotating flows will be the focus of the current section.

4.6.1 Gradient diffusion hypothesis

As mentioned earlier in Sec. 2.5.3, the fundamental assumption that underlies using a single gradient model for both convective and pressure transport quantities is that the pressure transport acts to counter the convective effects. By this hypothesis, Yoshizawa and Horiuti (1985) used the model formulated by Shir (1973) for modelling both the convective and the pressure transport terms in Eq. (2.14)). We re-express the model of Shir (1973) here:

$$\mathcal{T}_{mmk}^{(u+p)} = -C_s \frac{k_{sgs}^2}{\varepsilon} \frac{\partial k_{sgs}}{\partial x_k}.$$

Table 4.4 shows the correlation levels that exist between the divergence of the modelled and the actual transport terms (pressure and convective), and also between the actual convective and pressure transport quantities. Before we discuss the effectiveness of Shir (1973) model for different cases, we first verify the validity of the counter-gradient hypothesis. For this, we simply look at the level of correlation that exists between the divergence of convective and

Case	$\hat{\rho} \left(\frac{\partial \mathcal{T}'_{iik}}{\partial x_k}, \frac{\partial \mathcal{T}'_{iik,mod}}{\partial x_k} \right)$	$\hat{\rho} \left(\frac{\partial \mathcal{T}^{(c)}_{iik}}{\partial x_k}, \frac{\partial \mathcal{T}^{(p)}_{iik}}{\partial x_k} \right)$
DF	0.31	-0.38
DFRw	0.25	-0.45
DFRs	0.10	-0.36

Table 4.4: Correlation coefficients for the modelled and the actual tensor elements of the divergence of turbulent kinetic energy transport tensor, and correlation between convective and pressure transport for forced turbulence with and without system rotation (DF, DFRw, and DFRs).

Model	Variance		Flatness	
	$\frac{\partial \mathcal{T}'_{iik}}{\partial x_k}$	$\frac{\partial \mathcal{T}'_{iik,mod}}{\partial x_k}$	$\frac{\partial \mathcal{T}'_{iik}}{\partial x_k}$	$\frac{\partial \mathcal{T}'_{iik,mod}}{\partial x_k}$
DF	1.66	93.01	14.46	248.90
DFw	2.42	265.60	26.61	1169.00
DFs	12.6	66100.00	184.10	5171.00

Table 4.5: Variance and flatness for the divergence of modelled and actual transport quantities for the three cases.

pressure transport quantities. From Tab. 4.4, it can be seen that these two terms are indeed negatively correlated ($\sim 40\%$) for all cases considered, thereby supporting the application of the hypothesis for rapidly rotating cases as well. Moving on to the performance of the Shir (1973) model, we examine the correlation between the actual and modelled $\frac{\partial}{\partial x_k} \mathcal{T}'_{mmk}^{(u+p)}$ instead of $\mathcal{T}'_{mmk}^{(u+p)}$, because, this gives us a direct understanding of its representation in the k_{sgs} evolution equation (Eq. (2.14)). From Tab. 4.4, it can be seen that correlation coefficients decrease with increase in the system rotation rate. The correlation drops from 31% for DF to 10% for DFRs. In order to represent the localised intensities and the level of intermittency of the terms for the different cases, we also look at their variance and flatness. From Tab. 4.5, we can see that both the variance and the flatness of the quantities computed from DNS increase for DFRs by almost one order of magnitude when compared to the DF and DFRw. While the modelled term captures this trend, the variance and flatness are grossly overpredicted by the model indicating the presence of high fluctuations in the modelled quantity compared to the actual field computed from DNS.

4.6.2 Modelling of the subgrid-scale kinetic energy dissipation

The SGS kinetic energy dissipation plays a part as a sink in the modelled SGS kinetic energy evolution equation (Eq. (2.40)), and as a timescale $\tau^* = k_{sgs}/\varepsilon$ in the explicit formulation for modelled SGS stress (Eq. (2.37)). Through the formulation of timescale, it also controls the SGS kinetic energy production. Recall the expression for the modelled dissipation (Eq. (2.39)):

$$\varepsilon = C_c \frac{k_{sgs}^{3/2}}{\Delta}.$$

The correlation coefficients for the modelled dissipation for the three cases are shown in Tab. 4.6. In DF and DFRw, we obtain similar levels of correlation ($70 \sim 75\%$) while for DFRs, the value of correlation drops to 54%. Tab. 4.6 also shows the variance and flatness of the actual and the modelled dissipation. It is interesting to see that the intensity of the fluctuations about the mean value are of the same order of magnitude in all the cases considered. On

Case	$\hat{\rho}(\mathcal{P}, \mathcal{P}^{mod})$	Variance		Flatness	
		ε	ε^{mod}	ε	ε^{mod}
DF	0.70	0.24	7.32	10.14	23.20
DFRw	0.75	0.45	16.13	17.83	69.62
DFRs	0.54	0.39	303.27	46.68	334.00

Table 4.6: Correlation coefficients, variance, and flatness for the modelled and the actual subgrid-scale kinetic energy dissipation for the three cases: DF, DFRw, and DFRs.

the other hand, the variance of the modelled dissipation shows an increase in the order of magnitude with rotation. It also seems that these variations about the mean of the modelled dissipation occur more intermittently with rotation as is shown by the values of flatness in Tab. 4.6. The flatness of the actual SGS kinetic energy dissipation from the DNS however, indicates a much smoother variation in space even for the rapidly rotating case.

4.7 Perfect equilibrium between the subgrid-scale kinetic energy production and dissipation

From the values of correlation values for the modelled SGS stresses (discussed in Sec. 4.4), it seems that the EASSMs are superior in the representation of the SGS stresses when compared with DSM, in the limit of strongly rotating turbulence. In order to further scrutinise the EASSMs, the assumption that the SGS kinetic energy production and dissipation are in perfect balance locally will be examined in this section. For this purpose, we look at the PDFs of the ratio \mathcal{P}/ε for the three cases.

Figure 4.8 shows the PDFs for \mathcal{P}/ε for the different cases. The PDFs for DF and DFRw closely resemble each other while the PDF for DFRs shows a distribution with heavier tails and lower peak value. Also it can be noticed that \mathcal{P}/ε tends to a symmetric distribution with increase in rotation. This is also captured in skewness of \mathcal{P}/ε which reduces from 2.2 for DF to 0.6 for DFRs. This is not surprising as in the earlier discussion, we also saw that the PDF of production tends towards symmetry with increasing rotation. From the peak values displayed, for the cases DF and DFRw, the value of \mathcal{P}/ε in the neighbourhood of 1 seems to be highly likely while, in the presence of strong rotation, there seems to an offset in the peak towards a lower positive value. The flatness of the distribution increases from 13 for DF to 30 for DFRs, suggesting a higher level of intermittency.

As mentioned earlier, the presence of \mathcal{P}/ε poses a non-linearity in the formulation that hinders the straightforward derivation of an explicit formulation. Avoiding an iterative solution for the non-linear system implies that either the ratio be treated as an extra unknown that needs

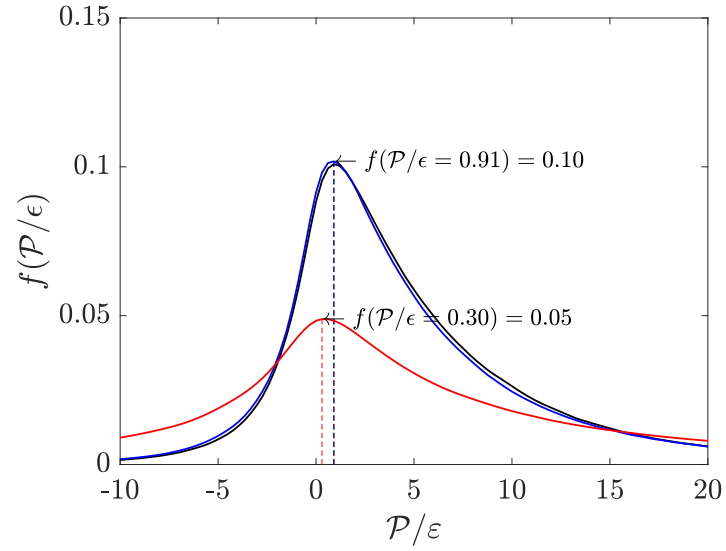


Figure 4.8: Probability density function: f of the ratio of SGS kinetic energy production to dissipation for the three cases. — DF; — DFRw; — DFRs.

to be solved from additional closures or the ratio be calibrated to a prescribed value. The assumption of perfect equilibrium is simply a calibration to 1. While we see that this is indeed a reasonable choice of value for isotropic or weakly rotating turbulence, this assumption seems questionable in rapidly rotating flows. Furthermore, the assumption that \mathcal{P}/ϵ is uniform over the entire domain is nevertheless limiting in terms of the overall generality of the model.

Chapter 5

Formulation of an alternative modelling approach for explicit algebraic subgrid-scale stress model

We have seen in the previous chapter that the EASSMs give good tensor level correlations for the normal SGS stress components in all cases (DF, DFRw, and DFRs). They are in the range of 20 – 40% for the non-dynamic model and 40 – 60% for the dynamic model. While the weak-equilibrium assumption is vital in order to reduce the SGS stress evolution equation to an algebraic form, the assumption of perfect equilibrium between the SGS kinetic energy production and dissipation used by [Marstorp et al. \(2009\)](#) can be improved. It is indeed acknowledged that this assumption does simplify the model drastically ([Marstorp et al. \(2009\)](#)), giving purely algebraic formulations for SGS stress, kinetic energy, and timescale. Nevertheless, this assumptions implies that the temporal evolution of SGS kinetic energy is negligible ($\langle D \rangle k_{sgs} / Dt = 0$). This is of course not true, for instance, in a case of decaying turbulence where k_{sgs} evolves continuously in time. In this chapter, we introduce an alternative way of treating the ratio \mathcal{P}/ε that does not involve a pre-calibration to a fixed value or any additional closures.

5.1 Formulation of an explicit expression for subgrid-scale stress with an additional scalar unknown

As mentioned in Ch. 1, the presence of the ratio of SGS kinetic energy production to dissipation, \mathcal{P}/ε , in the equations for SGS stress makes the resulting closure implicit due to the presence of non-linearity. To circumvent this, we follow the approach that was initially taken by [Girimaji \(1996\)](#), i.e. we treat this ratio as an extra unknown. By doing this, we derive an explicit expression for the SGS stress that retains the ratio \mathcal{P}/ε .

To derive an explicit model, we start from Eq. (2.16), which reads

$$\frac{\tau_{ij}}{k_{sgs}} (\mathcal{P} - \epsilon) = \mathcal{P}_{ij} + \Pi_{ij} - \epsilon_{ij}.$$

We employ the linear LRR-QI model for the pressure-strain term based on the results of isotropic and weakly rotating cases of forced homogeneous turbulence, which were discussed during the a priori studies in Ch. 4. The two variations of the model (QI and IP), provide very similar correlation values, however, since the IP model is derived by further simplifying the QI model (as described in Sec. 2.4.1), we employ the (unsimplified) LRR-QI model shown in Eq. (2.19) for the pressure-strain term in our formulation. For the dissipation term, ϵ_{ij} , an isotropic model is used as in Eq. (2.22). The corresponding expressions for \mathcal{P}_{ij} , and modelled Π_{ij} and ϵ_{ij} , thereby read

$$\begin{aligned} \mathcal{P}_{ij} &= k_{sgs} \left[\frac{-4}{3} \langle S_{ij} \rangle - \left(a_{ik} \langle S_{kj} \rangle + \langle S_{ik} \rangle a_{kj} \right) + \left(a_{ik} \langle \Omega_{kj} \rangle - \langle \Omega_{ik} \rangle a_{kj} \right) \right], \\ \Pi_{ij} &= -C_R \epsilon a_{ij} + \frac{4}{5} k_{sgs} \langle S_{ij} \rangle + \frac{3}{11} (2 + 3C_2) k_{sgs} \left(\langle S_{ik} \rangle a_{kj} + a_{ik} \langle S_{kj} \rangle - \frac{2}{3} \langle S_{kl} \rangle a_{kl} \delta_{ij} \right) \\ &\quad + \frac{1}{11} (10 - 7C_2) k_{sgs} \left(\langle \Omega_{ik} \rangle a_{kj} - a_{ik} \langle \Omega_{kj} \rangle \right), \quad \text{and} \\ \epsilon_{ij} &= \frac{2}{3} \epsilon \delta_{ij}. \end{aligned}$$

Substituting the above expressions into Eq. (2.16) and grouping similar terms, we get

$$\begin{aligned} \frac{\tau_{ij}}{k_{sgs}} (\mathcal{P} - \epsilon) &= -C_R \epsilon a_{ij} - \frac{8}{15} k_{sgs} \langle S_{ij} \rangle + \left(\frac{9C_2 - 5}{11} \right) \left(\langle S_{ik} \rangle a_{kj} + a_{ik} \langle S_{kj} \rangle \right) k_{sgs} \\ &\quad - \left(\frac{18C_2 + 12}{33} \right) k_{sgs} \langle S_{kl} \rangle a_{kl} \delta_{ij} + \left(\frac{1 - 7C_2}{11} \right) \left(a_{ik} \langle \Omega_{kj} \rangle - \langle \Omega_{ik} \rangle a_{kj} \right) k_{sgs} \\ &\quad - \frac{2}{3} \epsilon \delta_{ij}. \end{aligned} \tag{5.1}$$

Dividing the above expression by ϵ and replacing

$$\tau^* = k_{sgs} / \epsilon, \quad \text{and} \quad \frac{\mathcal{P}}{\epsilon} = -\frac{k_{sgs}}{\epsilon} \langle S_{kl} \rangle a_{kl}$$

Eq. (5.1) can be rewritten in terms of normalised SGS stress anisotropy a_{ij} as

$$\begin{aligned} \left(a_{ij} + \frac{2}{3} \delta_{ij} \right) \left(\frac{\mathcal{P}}{\epsilon} - 1 \right) + C_R a_{ij} &= -\frac{8}{15} \tau^* \langle S_{ij} \rangle \\ &\quad + \left(\frac{9C_2 - 5}{11} \right) \left(\langle S_{ik} \rangle a_{kj} + a_{ik} \langle S_{kj} \rangle \right) \tau^* \\ &\quad + \left(\frac{18C_2 + 12}{33} \right) \frac{\mathcal{P}}{\epsilon} \delta_{ij} \\ &\quad + \left(\frac{1 + 7C_2}{11} \right) \left(a_{ik} \langle \Omega_{kj} \rangle - \langle \Omega_{ik} \rangle a_{kj} \right) \tau^* \\ &\quad - \frac{2}{3} \delta_{ij}. \end{aligned} \tag{5.2}$$

At this point, the choice of tensors for expressing the normalised SGS stress anisotropy introduced by Pope (1975) will have to be made. For deriving the final explicit expression, we use the tensors, i.e. $T_{ij}^{(1)}$ and $T_{ij}^{(2)}$ for expressing a_{ij} , in order to maintain the same degree of non-linearity in the final expression as in the EASSMs of Marstorp et al. (2009). This allows us to assess the effects of only avoiding the perfect equilibrium assumption on the EASSM. The normalised anisotropy is therefore expressed in terms of the two tensors and their coefficients as,

$$a_{ij} = \sum_{n=1}^2 G^{(n)} T_{ij}^{(n)}, \quad (5.3)$$

where, the basis tensors (in matrix form) read,

$$\mathbf{T}^{(1)} = \tau^* \mathbf{S}, \quad \text{and} \quad \mathbf{T}^{(2)} = \tau^{*2} (\mathbf{S}\Omega - \Omega\mathbf{S}).$$

First, we substitute Eq. (5.3) for the normalised SGS stress anisotropy in Eq. (5.2). The higher order tensors that result can be simplified using Cayley-Hamilton theorem as shown in Pope (1975) using the identities,

$$\mathbf{c}^2 = \mathbf{c}\{\mathbf{c}\} - \frac{1}{2} \mathbf{I}_2 (\{\mathbf{c}\}^2 - \{\mathbf{c}^2\}) \quad (5.4)$$

$$\mathbf{b}\mathbf{a}\mathbf{b} = \frac{1}{2} (\mathbf{a} - \mathbf{I}_2\{\mathbf{a}\}) (\{\mathbf{b}\}^2 - \{\mathbf{b}^2\}) + \mathbf{b}\{\mathbf{a}\mathbf{b}\}, \quad (5.5)$$

where, \mathbf{a} , \mathbf{b} and \mathbf{c} are two dimensional tensors, $\{\cdot\}$ represents the trace, and \mathbf{I}_2 is an identity matrix. Therefore, the substitution of the bases tensors $\mathbf{T}^{(1)}$ and $\mathbf{T}^{(2)}$ for the terms on the RHS of Eq. (5.2) results in the following:

$$\begin{aligned} \tau^* \mathbf{S} &= \mathbf{T}^{(1)} \\ \mathbf{S}\mathbf{a} + \mathbf{a}\mathbf{S} &= G^{(1)} \tau^* \mathbf{S}\mathbf{S} + G^{(2)} \tau^{*2} \mathbf{S}\mathbf{S}\Omega - G^{(2)} \tau^{*2} \mathbf{S}\Omega\mathbf{S} + G^{(1)} \tau^* \mathbf{S}\mathbf{S}\Omega, \\ &\quad + G^{(2)} \tau^{*2} \mathbf{S}\Omega\mathbf{S} - G^{(2)} \tau^{*2} \Omega\mathbf{S}\mathbf{S} \\ &= \frac{G^{(1)}}{2} \tau^* \mathbf{I}_2 \{\mathbf{S}^2\} + \frac{G^{(2)}}{2} \tau^{*2} \Omega \{\mathbf{S}^2\} + \frac{G^{(1)}}{2} \tau^* \mathbf{I}_2 \{\mathbf{S}^2\} - \frac{G^{(2)}}{2} \tau^{*2} \Omega \{\mathbf{S}^2\} \\ &= G^{(1)} \tau^* \mathbf{I}_2 \{\mathbf{S}^2\}, \\ \mathbf{a}\Omega - \Omega\mathbf{a} &= G^{(1)} \tau^* \mathbf{S}\Omega + G^{(2)} \tau^{*2} \mathbf{S}\Omega\Omega - G^{(2)} \tau^{*2} \Omega\mathbf{S}\Omega - G^{(1)} \tau^* \Omega\mathbf{S} \\ &\quad - G^{(2)} \tau^{*2} \Omega\mathbf{S}\Omega + G^{(2)} \tau^{*2} \Omega\Omega\mathbf{S} \\ &= G^{(1)} \tau^* (\mathbf{S}\Omega - \Omega\mathbf{S}) + \frac{G^{(2)}}{2} \tau^{*2} \mathbf{S}\{\Omega^2\} + \frac{G^{(2)}}{2} \tau^{*2} \mathbf{S}\{\Omega^2\} \\ &\quad + \frac{G^{(2)}}{2} \tau^{*2} \mathbf{S}\{\Omega^2\} + \frac{G^{(2)}}{2} \tau^{*2} \mathbf{S}\{\Omega^2\} \\ &= \frac{G^{(1)}}{\tau^*} \mathbf{T}^{(2)} + 2G^{(2)} \tau^* \{\Omega^2\} \mathbf{T}^{(1)}. \end{aligned} \quad (5.6)$$

Substituting the above expressions for the different terms back into Eq. (5.2), we get,

$$\begin{aligned} \left(\frac{\mathcal{P}}{\varepsilon} - 1 + C_R\right) \mathbf{a} + \frac{2\mathcal{P}}{3\varepsilon} \delta_{ij} = & -\frac{8}{15} \mathbf{T}^{(1)} \\ & + \left(\frac{9C_2 - 5}{11}\right) \left(\tau^{*2} G^{(1)} \mathbf{I}_2\{\mathbf{S}^2\}\right) \\ & + \left(\frac{18C_2 + 12}{33}\right) \frac{\mathcal{P}}{\varepsilon} \delta_{ij} \\ & + \left(\frac{1 + 7C_2}{11}\right) \left(G^{(1)} \mathbf{T}^{(2)} + 2\tau^{*2} G^{(2)} \mathbf{T}^{(1)}\{\Omega^2\}\right). \end{aligned} \quad (5.7)$$

Equating the terms that are not functions of the tensors $\mathbf{T}^{(1)}$ and $\mathbf{T}^{(2)}$,

$$\begin{aligned} \left(\frac{9C_2 - 5}{11}\right) \left(\tau^{*2} G^{(1)} \mathbf{I}_2\{\mathbf{S}^2\}\right) + \left(\frac{18C_2 + 12}{33}\right) \frac{\mathcal{P}}{\varepsilon} \delta_{ij} - \frac{2\mathcal{P}}{3\varepsilon} \delta_{ij} = 0, \\ \left(\frac{9C_2 - 5}{11}\right) \left(\tau^{*2} G^{(1)} \mathbf{I}_2\{\mathbf{S}^2\}\right) + \left(\frac{18C_2 - 10}{33}\right) \frac{\mathcal{P}}{\varepsilon} \delta_{ij} = 0. \end{aligned} \quad (5.8)$$

Choosing the value of the constant $C_2 = 5/9$ satisfies Eq. (5.8). Substituting this value of C_2 in Eq. (5.7) results in,

$$\begin{aligned} \left(\frac{\mathcal{P}}{\varepsilon} - 1 + C_R\right) \mathbf{a} = & \left(-\frac{8}{15} + \frac{4}{9} 2\tau^{*2} G^{(2)}\{\Omega^2\}\right) \mathbf{T}^{(1)} + \frac{4}{9} G^{(1)} \mathbf{T}^{(2)}, \\ \mathbf{a} = & \frac{1}{\left(\frac{\mathcal{P}}{\varepsilon} - 1 + C_R\right)} \left(-\frac{8}{15} + \frac{4}{9} 2\tau^{*2} G^{(2)}\{\Omega^2\}\right) \mathbf{T}^{(1)} \\ & + \frac{1}{\left(\frac{\mathcal{P}}{\varepsilon} - 1 + C_R\right)} \frac{4}{9} G^{(1)} \mathbf{T}^{(2)}. \end{aligned} \quad (5.9)$$

Comparing the above expression with that in Eq. (5.3), we can equate,

$$\begin{aligned} G^{(1)} = & \frac{1}{\left(\frac{\mathcal{P}}{\varepsilon} - 1 + C_R\right)} \left(-\frac{8}{15} + \frac{4}{9} 2\tau^{*2} G^{(2)}\{\Omega^2\}\right), \\ G^{(2)} = & \frac{1}{\left(\frac{\mathcal{P}}{\varepsilon} - 1 + C_R\right)} \frac{4}{9} G^{(1)}. \end{aligned} \quad (5.10)$$

Solving the above equations to find the value of $G^{(1)}$ and $G^{(2)}$, we first obtain

$$G^{(2)} = \frac{4}{9\eta} G^{(1)}, \quad (5.11)$$

where $\eta = \frac{\mathcal{P}}{\varepsilon} - 1 + C_R$.

$$\begin{aligned}\eta G^{(1)} &= -\frac{8}{15} + \left(\frac{4}{9}\right)^2 \frac{1}{\eta} G^{(1)} \tau^{*2} \{\Omega^2\}, \\ G^{(1)} &= -\frac{8}{15\eta} + \left(\frac{4}{9\eta}\right)^2 G^{(1)} \tau^{*2} \{\Omega^2\}, \\ G^{(1)} \left[1 - \frac{2\tau^{*2} \{\Omega^2\}}{\left(\frac{9\eta}{4}\right)^2} \right] &= -\frac{8}{15\eta}, \\ G^{(1)} \left[\frac{\left(\frac{9\eta}{4}\right)^2 - 2\tau^{*2} \{\Omega^2\}}{\left(\frac{9\eta}{4}\right)^2} \right] &= -\frac{8}{15\eta}, \\ G^{(1)} &= -\frac{18}{15} \left[\frac{\left(\frac{9\eta}{4}\right)}{\left(\frac{9\eta}{4}\right)^2 - 2\tau^{*2} \{\Omega^2\}} \right].\end{aligned}$$

In the final expression for τ_{ij} , we replace the Rotta's constant C_R with another arbitrary constant C_1 for generality. The explicit expression for the SGS stresses now reads,

$$\tau_{ij} = k_{sgs} \left[G^{(1)} \tau^* \langle S_{ij} \rangle + G^{(2)} \tau^{*2} \left(\langle S_{ik} \rangle \langle \Omega_{kj} \rangle - \langle \Omega_{ik} \rangle \langle S_{kj} \rangle \right) + \frac{2}{3} \delta_{ij} \right], \quad (5.12)$$

where,

$$G^{(1)} = -\frac{18}{15} \left[\frac{\left(\frac{9\eta}{4}\right)}{\left(\frac{9\eta}{4}\right)^2 - 2\tau^{*2} \langle \Omega_{ik} \rangle \langle \Omega_{ki} \rangle} \right], \quad (5.13)$$

$$G^{(2)} = \frac{4}{9\eta} G^{(1)}, \quad (5.14)$$

$$\eta = \frac{\mathcal{P}}{\varepsilon} - 1 + C_1. \quad (5.15)$$

We still use the value of $C_1 = 1.5$ that was suggested by [Rotta \(1951\)](#). The methodology behind deriving the formulation in Eq. (5.12) is summarized below.

- i Choose the original LRR-QI model for pressure-strain term and the isotropic model for dissipation term.
- ii The difference between the original model used here and the modified version used by [Marstorp et al. \(2009\)](#) lies in the selection of C_1 and the coefficient of the term $k_{sgs} \langle S_{ij} \rangle$ in the LRR model.

- iii After substituting the tensors $\mathbf{T}^{(1)}$ and $\mathbf{T}^{(2)}$ for normalised SGS stress anisotropy, simplify the expression using Cayley-Hamilton theorem. This will result in Eq. (5.7).
- iv Equate the coefficients of the tensorial bases and solve the resulting system to find expressions for the coefficients.

5.2 Additional closures

The weak-equilibrium assumption was initially introduced by Rodi (1972) purely from a mathematical standpoint to reduce the steady-state transport equation for Reynolds stresses which contains spatial derivatives. A more physical reasoning for this was provided in Sec. 2.3, we briefly reiterate that the transient nature (growth or decay of the SGS quantities) due to an imbalance between SGS kinetic energy production and dissipation can be captured by solving an evolution equation for k_{sgs} while the corresponding evolution of SGS stress anisotropy can be treated to be negligible in comparison. All the formulations of explicit algebraic (Reynolds) models in RANS therefore include solving a transport/evolution equation for turbulent kinetic energy. We also believe that solving an evolution equation for SGS kinetic energy for the EASSM in LES would improve the capability of the model to capture more efficiently the transient nature of the SGS and consequently the resolves scales as well. For this purpose, we use the modelled evolution equation of k_{sgs} introduced by Yoshizawa and Horiuti (1985), which reads

$$\frac{\langle D \rangle k_{sgs}}{Dt} = -\tau_{ij} \frac{\partial \langle u_i \rangle}{\partial x_j} + \frac{\partial}{\partial x_j} \left[(\nu_k + \nu) \frac{\partial k_{sgs}}{\partial x_j} \right] - C_c \frac{k_{sgs}^{3/2}}{\Delta},$$

where, $\nu_k = C_k \sqrt{k_{sgs}} \Delta$. Finally, the timescale is simply given by

$$\begin{aligned} \tau^* &= \frac{k_{sgs}}{\varepsilon} \\ &= \frac{\Delta}{C_c \sqrt{k_{sgs}}}. \end{aligned} \tag{5.16}$$

For the constants in the k_{sgs} equation, the value of $C_k = 0.1$ is used as suggested originally by Yoshizawa and Horiuti (1985). The value for the constant C_c in the expression for ε and τ^* (Eq. (5.16)) as suggested by Yoshizawa and Horiuti (1985) was 1. However, we find from DNS data by analysing the mean k_{sgs} and ε that a value of 5/2 gives a better agreement. As we will demonstrate in the next chapter, for isotropic cases, we find that this choice for the constant C_2 results in a very good prediction of the mean resolved kinetic energy.

At this point, we introduce a way to treat the ratio of \mathcal{P}/ε in Eq. (5.15). This ratio can be treated as an unknown scalar that gives an indication of the localised deviation from equilibrium between SGS kinetic energy production and dissipation. In order to treat this ratio, we introduce another assumption in addition to the weak equilibrium that the evolution

of the ratio of \mathcal{P}/ε occurs slowly in time. A point to note about this assumption is that it does add additional restrictions to the spatial variation of \mathcal{P}/ε . The need for such an assumption is not to reduce any temporal derivatives, but instead this assumption is made so that in LES the value of \mathcal{P}/ε computed at a time t_i (during the i^{th} step) can be used at the next timestep at t_{i+1} . Thereby we assume that the evolution of local imbalances between \mathcal{P} and ε evolve slowly in time.

The alternative, new formulation of EASSM which involves treating the ratio of \mathcal{P}/ε in the way explained here and solving a transport equation for k_{sgs} will henceforth be referred to as the non-equilibrium EASSM. The performance of the new model in comparison with the other SGS models will be the subject of the discussion in the subsequent chapter.

Chapter 6

A Posteriori Tests

The case of strong rotation is challenging for LES, for which, we see an overall deterioration of model performance for SGS stresses, pressure-strain, and the different (transport and dissipation) terms in the SGS kinetic energy evolution equation. So far, we have drawn conclusions based on the DNS data by means of a priori analysis. The current chapter will cover the details of a posteriori LES that were carried out using DSM, dynamic, non-dynamic and the new non-equilibrium EASSMs. The validation of the results are performed using DNS by computing different filtered and SGS quantities according to the corresponding LES grid dimensions. In this way, the performance of the ‘new’ model in comparison with the other SGS models that were previously discussed will be established.

6.1 Test cases

In the current analysis, LES of forced and decaying turbulence were carried out using four SGS models model, which are DSM, dynamic, non-dynamic, and non-equilibrium EASSMs. We primarily examine the evolution of the mean¹ resolved and SGS quantities obtained for different simulations. For each case of turbulence, we conduct LES on three computational grids with total number of nodes, $N = 32^3$, 40^3 , and 64^3 , in order to see the effect of grid refinement on the model performance. For the purpose of validating the LES results in each case, DNS was carried out on a grid of size 512^3 . The computational domain for both LES and DNS is a cubical box that spans from 0 to 2π in each direction with periodic boundary condition.

We first study forced isotropic turbulence, simulated using the same forcing scheme and parameters as used for a priori studies, shown in Tab. 4.1. It needs to be pointed out that the forced simulations that will be discussed in the current chapter has a higher Re_f (~ 496) compared to the forced isotropic case discussed during the a priori studies (~ 88) in Ch. 4.

¹or all our cases, the mean value is the volume averaged value represented as $\langle \cdot \rangle_{\mathcal{L}}$.

This allows us to evaluate the model performance for varying levels of grid refinement.

As a second case, we study isotropically decaying turbulence. The steady-state solution of the forced isotropic DNS was used as the initial condition from which turbulence was allowed to decay with the external forcing turned off. The initial condition in case of LES is the steady-state solution from DNS, filtered to the corresponding LES grid dimension using a spectral cut-off filter.

As a final case, in order to study the effect of system rotation on the performance of SGS models, we also conducted LES of decaying turbulence under strong rotation with $Ro_f = 0.08$ fixed at the initial state. For all cases, the simulations (both LES and DNS) were run for six large eddy turnover times computed as

$$\tau_L = \frac{\langle K^{DNS} \rangle_{\mathcal{L}}}{\langle \varepsilon^{DNS} \rangle_{\mathcal{L}}}. \quad (6.1)$$

For forced simulations, $\langle K^{DNS} \rangle_{\mathcal{L}}$ and $\langle \varepsilon^{DNS} \rangle_{\mathcal{L}}$ are chosen as the time averaged steady-state values of mean turbulent kinetic energy and dissipation, respectively. For decaying cases, $\langle K^{DNS} \rangle_{\mathcal{L}}$ and $\langle \varepsilon^{DNS} \rangle_{\mathcal{L}}$ are the total turbulent kinetic energy and dissipation, respectively, computed at the initial state.

6.2 Forced isotropic turbulence

We start the forced isotropic simulations from a zero-velocity state with the modelled evolution equation for SGS kinetic energy (Eq. 2.40) initialised to 1×10^{-3} . The reason for not initialised k_{sgs} in the non-equilibrium EASSM to zero as done for velocity fields is because, there is no external forcing term present in Eq. (2.40). Therefore, initialising it to zero everywhere will make the modelled k_{sgs} evolution equation and consequently the non-equilibrium EASSM inactive. With regard to time marching, as we start the simulations from an initial zero velocity state, during the first time marching loop, the dynamic time step determined based on the Courant-Friedrichs-Lewy (CFL) number was too high. Therefore, in order to prevent this jump, we use a fixed timestep for all forced LES, chosen such that the CFL number for the simulations stay under ~ 0.5 .

6.2.1 Resolved quantities

The evolution of the mean resolved kinetic energy $\langle K^r \rangle_{\mathcal{L}} = \frac{1}{2} \langle \langle u_i \rangle \langle u_i \rangle \rangle_{\mathcal{L}}$, obtained from LES with different SGS models and grid sizes are shown on the left in Fig. 6.1. Alongside LES results on grids with $N = 32^3$, 40^3 , and 64^3 , the corresponding values from DNS, filtered with $\kappa_c = 16$, 20, and 32, respectively, using a spectral cut-off filter are also plotted in Fig. 6.1. The DNS datapoints very clearly indicate the presence of a peak in the evolution of $\langle K^r \rangle_{\mathcal{L}}$ at $t/\tau_L \sim 1.2$. In the case of LES, for the coarse meshes with $N = 32^3$ and 40^3 , it can be

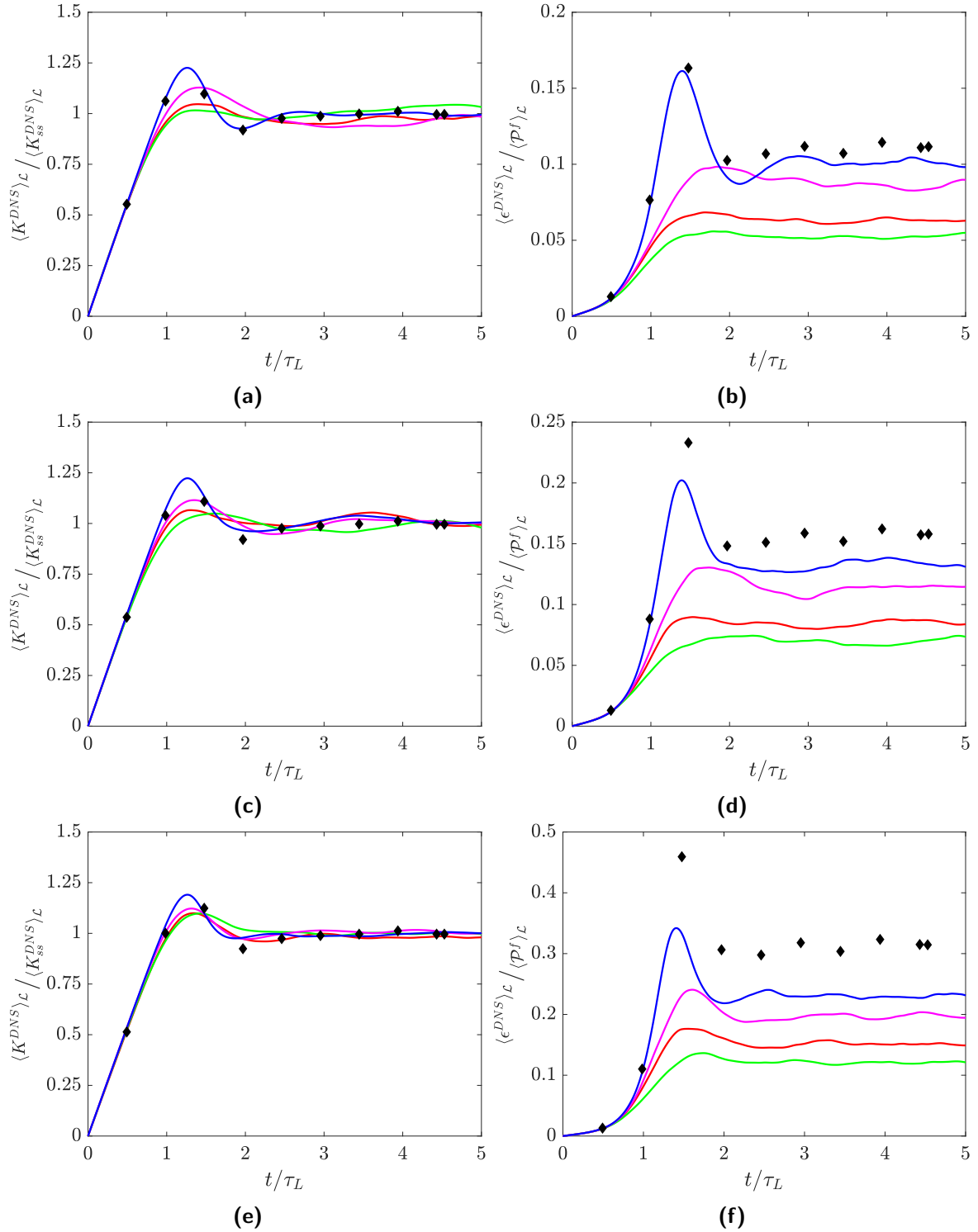


Figure 6.1: Evolution of (left) mean resolved kinetic energy, non-dimensionalised with the steady-state value and (right) dissipation, non-dimensionalised with the power input due to external forcing, for forced isotropic case obtained using different SGS model in LES plotted alongside the corresponding filtered DNS datapoints. From top to bottom are the results of LES run on a computation mesh with $N = 32^3$, 40^3 , and 64^3 . — DSM; — dynamic EASSM; — non-dynamic EASSM; — non-equilibrium EASSM; ◆ filtered DNS.

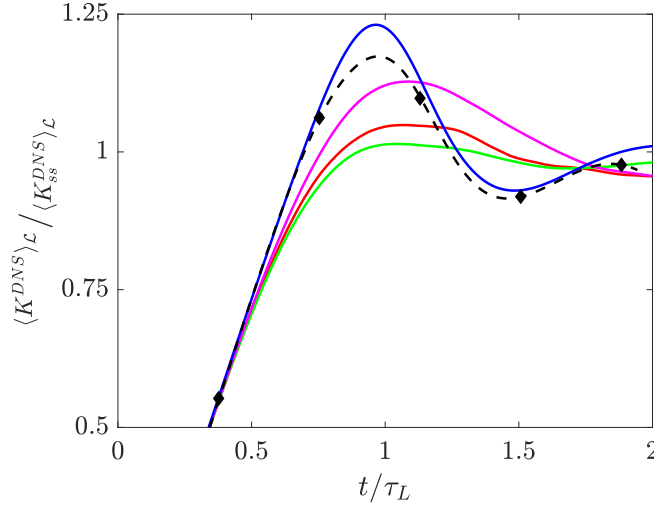


Figure 6.2: Evolution of the mean resolved kinetic energy for forced isotropic case in the neighbourhood of the peak value plotted alongside filtered DNS interpolated to obtain an estimate of the peak value. The plots correspond to LES conducted on a grid with $N = 32^3$. — DSM — dynamic EASSM; — non-dynamic EASSM; — non-equilibrium EASSM; ◆ filtered DNS; --- interpolated DNS.

seen from Fig. 6.1a, and 6.1c that the dynamic models (DSM and dynamic EASSM) do not show any indication of a peak in the initial growth of the mean resolved kinetic energy. These models show a smooth attainment of steady-state. Only for the finest mesh ($N = 64^3$ in Fig. 6.1e) do the dynamic models indicate the presence of an overshoot in the growth of $\langle K^r \rangle_{\mathcal{L}}$. Nevertheless, the peak values predicted by the dynamic models on the finest mesh are still lower than DNS. In comparison with dynamic models, non-dynamic EASSM gives a closer match with DNS. However, in Fig. 6.1 (left) we do not see any appreciable improvement in the prediction of the peak value with grid refinement. On the other hand, non-equilibrium EASSM predicts the growth of mean resolved kinetic energy very well. Even for the coarsest mesh, $N = 32^3$ in Fig. 6.1a, non-equilibrium model shows a very close match for mean resolved kinetic energy from DNS, especially in the neighbourhood of the peak.

In the evolution of $\langle K^r \rangle_{\mathcal{L}}$, as we do not have the DNS datapoint at the time instant corresponding to the peak value, we cannot properly assess if the peak value shown by the non-equilibrium EASSM in Fig. 6.1 (left) is in fact the right value obtained in DNS. Therefore, in order to get an estimation of the peak value in DNS, we compute the ratio of mean turbulent kinetic energy to mean resolved kinetic energy, i.e. $\langle K^{DNS} \rangle_{\mathcal{L}} / \langle K^r \rangle_{\mathcal{L}}$. This ratio can be interpolated to any intermediate point and since the evolution of $\langle K^{DNS} \rangle_{\mathcal{L}}$ is available at every timestep for DNS, we use this interpolated ratio to get an estimate of the peak value. The corresponding plot for $N = 32^3$ is shown in Fig. 6.2. Non-equilibrium EASSM seems to overpredict the peak slightly. Nevertheless, given the randomness in external forcing and in comparison with other SGS models, non-equilibrium model gives the closest match to DNS.

We now move on to analysing the evolution of the mean kinetic energy dissipation² $\langle \varepsilon^r \rangle_{\mathcal{L}}$

² $\varepsilon^r = \nu \langle \frac{\partial u_i}{\partial x_j} \rangle \langle \frac{\partial u_i}{\partial x_j} \rangle$.

Model	$\langle K_{ss}^r \rangle_{\mathcal{L}}$			$\langle \varepsilon_{ss}^r \rangle_{\mathcal{L}}$		
	N = 32	N = 40	N = 64	N = 32	N = 40	N = 64
DSM	2.23	2.27	2.38	0.06	0.08	0.15
Dyn. EASSM	2.19	2.26	2.34	0.05	0.07	0.12
Non-dyn. EASSM	2.22	2.24	2.32	0.08	0.11	0.20
Non-eq. EASSM	2.23	2.25	2.34	0.10	0.13	0.23
Filtered DNS	2.25	2.31	2.42	0.11	0.16	0.31

Table 6.1: Time averaged steady-state values of the mean resolved kinetic energy and dissipation obtained for the forced isotropic turbulence using different SGS models and mesh sizes along with the corresponding values from DNS.

obtained using different SGS models. The corresponding plots for different grids are shown on the right side of Fig. 6.1. The total resolved dissipation also indicates the net amount of energy transferred from resolved to SGS. The total energy leaving the resolved spectrum, excluding numerical dissipation, is equal to the sum of resolved dissipation and the net energy transferred from resolved to SGS as a result of energy cascade, i.e. the total SGS kinetic energy production. Therefore, at steady-state, the total energy removed from the resolved scales must be equal to the energy input due to the external forcing, i.e. \mathcal{P}^f . Based on this reasoning, from Fig. 6.1 (right), it can be inferred that the mean energy cascade or transfer of energy from resolved to SGS permitted by non-equilibrium EASSM is the lowest compared to other SGS models. As a result, the mean resolved dissipation for the non-equilibrium EASSM is more than other models at all grid resolutions. Just as observed for the evolution of the mean resolved kinetic energy, for the coarsest grid (in Fig. 6.1b), non-equilibrium EASSM predicts the evolution of the mean resolved kinetic energy dissipation very well. Furthermore, it also captures the peak in the growth of $\langle \varepsilon^r \rangle_{\mathcal{L}}$. With grid refinement, we resolve more wavenumbers in the energy spectrum, and therefore, we expect $\langle \varepsilon \rangle_{\mathcal{L}}$ to reduce. Consequently, grid refinement increases the mean resolved dissipation, which we clearly see in Fig. 6.1 (right). We see the increase of $\langle \varepsilon^r \rangle_{\mathcal{L}}$ with grid refinement in LES as well, however, the deviation of the LES values from DNS becomes more pronounced. For the finest mesh, $N = 64^3$, all SGS models drain more energy from resolved scales compared to DNS. This is seen in Fig. 6.1f, where all models show lower levels of $\langle \varepsilon^r \rangle_{\mathcal{L}}$ compared to DNS, with the non-equilibrium EASSM showing the least amount of deviation from DNS values.

As a final assessment of resolved quantities obtained using different SGS models, time averaged values of mean resolved kinetic energy and dissipation are computed at steady-state. These values are shown in Tab. 6.1. All models predict fairly accurately the steady-state value of mean resolved kinetic energy. On the other hand, as is also evident from Fig. 6.1 (right),

all models underpredict the value of mean resolved kinetic energy dissipation, with the non-equilibrium EASSM giving the closest match to DNS.

6.2.2 Resolved spectrum

In addition to examining the mean resolved kinetic energy and dissipation, we also plot the time averaged LES and filtered DNS energy spectrum in Fig. 6.3. The filtered DNS spectrum for different grid sizes (or κ_c) are obtained using a spectral cut-off filter. We can see from Fig. 6.3 that the resolved spectrums corresponding to non-equilibrium and non-dynamic EASSMs give very good agreement with filtered DNS at all grid resolutions. On the other hand, all dynamic models deviate from the filtered DNS as κ approaches κ_c . This deviation is a result of the dynamic models draining energy excessively from the resolved scales when compared to DNS, non-equilibrium and non-dynamic EASSMs.

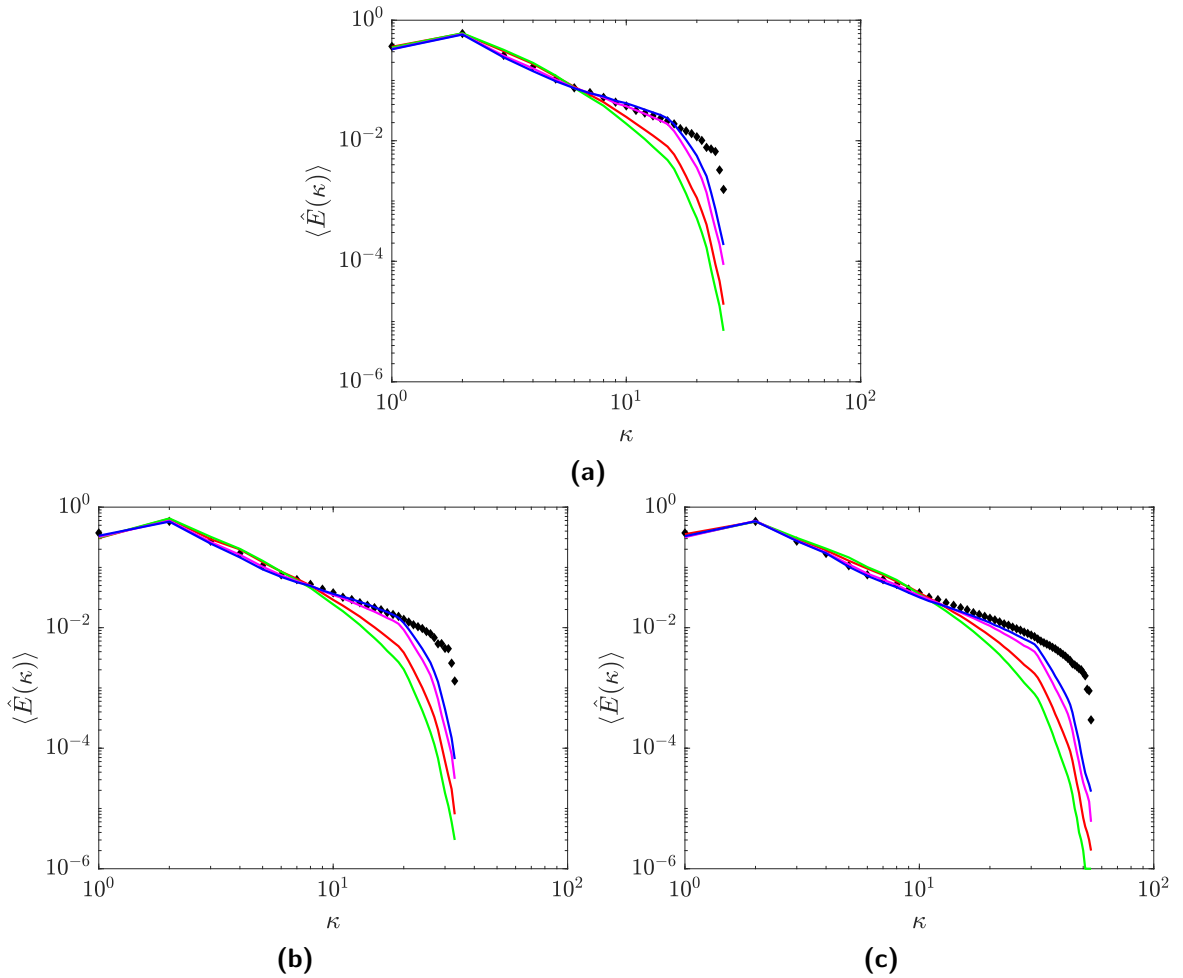


Figure 6.3: Time averaged resolved spectrum for the forced isotropic case obtained for LES and filtered DNS. (a) $N = 32^3$, (b) 40^3 , and (c) 64^3 . — DSM; — dynamic EASSM; — non-dynamic EASSM; — non-equilibrium EASSM; ◆ filtered DNS.

6.2.3 Subgrid-scale quantities

The purpose of SGS models in LES is to provide the right characteristics of the SGS, such that their effect on the resolved quantities are accurately represented. In the discussion so far, we have seen that the mean resolved kinetic energy and dissipation obtained using the non-equilibrium EASSM bare closer resemblance to DNS, when compared to the other models. In order to gain more insight into the functioning of the models, we examine the evolution of the mean SGS kinetic energy. This part of the analysis will be limited to EASSMs.

The evolution of the mean SGS kinetic energy, $\langle k_{sgs} \rangle_{\mathcal{L}}$, estimated by the three EASSMs are plotted alongside DNS results in Fig. 6.4. For all grid resolutions, dynamic EASSM does not

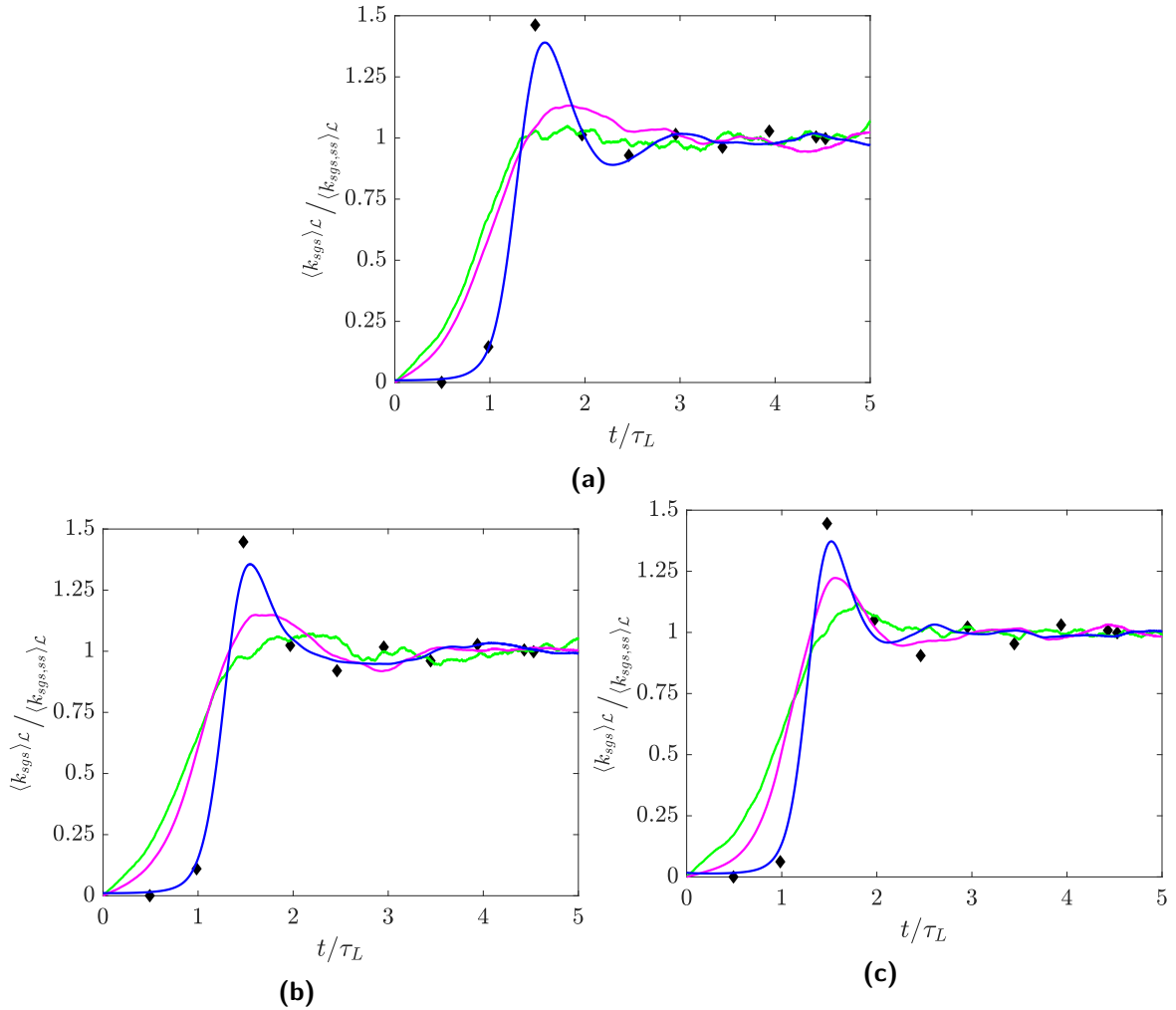


Figure 6.4: Evolution of mean subgrid-scale kinetic energy for forced isotropic case obtained for LES and filtered DNS. (a) $N = 32^3$, (b) 40^3 , and (c) 64^3 . — dynamic EASSM; — non-dynamic EASSM; — non-equilibrium EASSM; ◆ filtered DNS.

predict the peak in the evolution of $\langle k_{sgs} \rangle_{\mathcal{L}}$ and tends towards steady-state earlier than the other EASSMs. On the other hand, non-dynamic and non-equilibrium EASSMs, both capture the overshoot in the evolution of $\langle k_{sgs} \rangle_{\mathcal{L}}$. For non-dynamic EASSM, this is prominent only for the finer meshes, $N = 40^3$, and 64^3 (shown in Fig. 6.4b, and 6.4c) for which the peak value is still under-predicted compared to DNS. Non-equilibrium model, on the other hand shows a prominent peak even for the coarsest mesh, $N = 32^3$ (shown in Fig. 6.4a) which matches with DNS more closely than other models.

Another point to note is that, dynamic and non-dynamic EASSMs predict a growth in mean SGS kinetic energy from the start of the simulation. This is a result of using an algebraic expression to determine k_{sgs} , which in-turn is a consequence of the perfect equilibrium assumption ($\mathcal{P} = \varepsilon$). When k_{sgs} is modelled only as a function of $\langle S_{ij} \rangle$ and $\langle \Omega_{ij} \rangle$, it implies that k_{sgs} adapts instantaneously to the resolved scales. Therefore, as the resolved scales start to grow at the start of the simulation, SGS kinetic energy modelled by non-dynamic and dynamic EASSMs also starts to grow proportionately. This behaviour is recorded for all grids in Fig. 6.4. On the other hand, for non-equilibrium EASSM, it can be clearly seen from Fig. 6.4 that at all grid resolutions, SGS kinetic energy starts to grow only after $t/\tau_L \sim 0.5$. This matches better with the DNS results as well. As the external forcing adds energy to the resolved scales, the turbulent energy spectrum starts to grow and the SGS scales are formed only after spectrum grows past the cut-off wavenumber κ_c , which occurs at $t/\tau_L \sim 0.5$, in our case. The success of the non-equilibrium EASSM in capturing this delayed growth of $\langle k_{sgs} \rangle_{\mathcal{L}}$ is mainly attributed to solving the modelled evolution equation, Eq. (2.40).

6.3 Isotropic decaying turbulence

Now that we have established the performance of the different SGS models in forced isotropic turbulence, we study their behaviour for the case of isotropic decaying turbulence. The velocity fields were initialised using the filtered steady-state solution obtained from DNS, down-sampled to the corresponding LES grid size using a spectral cut-off filter. Since the spectral cut-off filter does not ensure realisable values for SGS stresses and kinetic energy, for non-equilibrium EASSM, SGS kinetic energy was initialised to a uniform field equal to the mean value of SGS kinetic energy, $\langle k_{sgs} \rangle_{\mathcal{L}}$, computed from DNS at the initial state. Both LES and DNS were performed using a dynamic time-stepping based on the CFL number, fixed to 0.3.

6.3.1 Resolved quantities

The decay of mean resolved kinetic energy, $\langle K^r \rangle_{\mathcal{L}}$, obtained using the different SGS models is shown on the left in Fig. 6.5, plotted against the number of large eddy turnover times. The corresponding values from DNS are also plotted alongside. It can be seen that the dynamic models (DSM and dynamic EASSM) give almost identical values for $\langle K^r \rangle_{\mathcal{L}}$ throughout the decay. Similarly, the decay of $\langle K^r \rangle_{\mathcal{L}}$ in non-equilibrium and non-dynamic EASSMs are very similar. When compared to DNS, all SGS models employed here provide a fairly close pre-

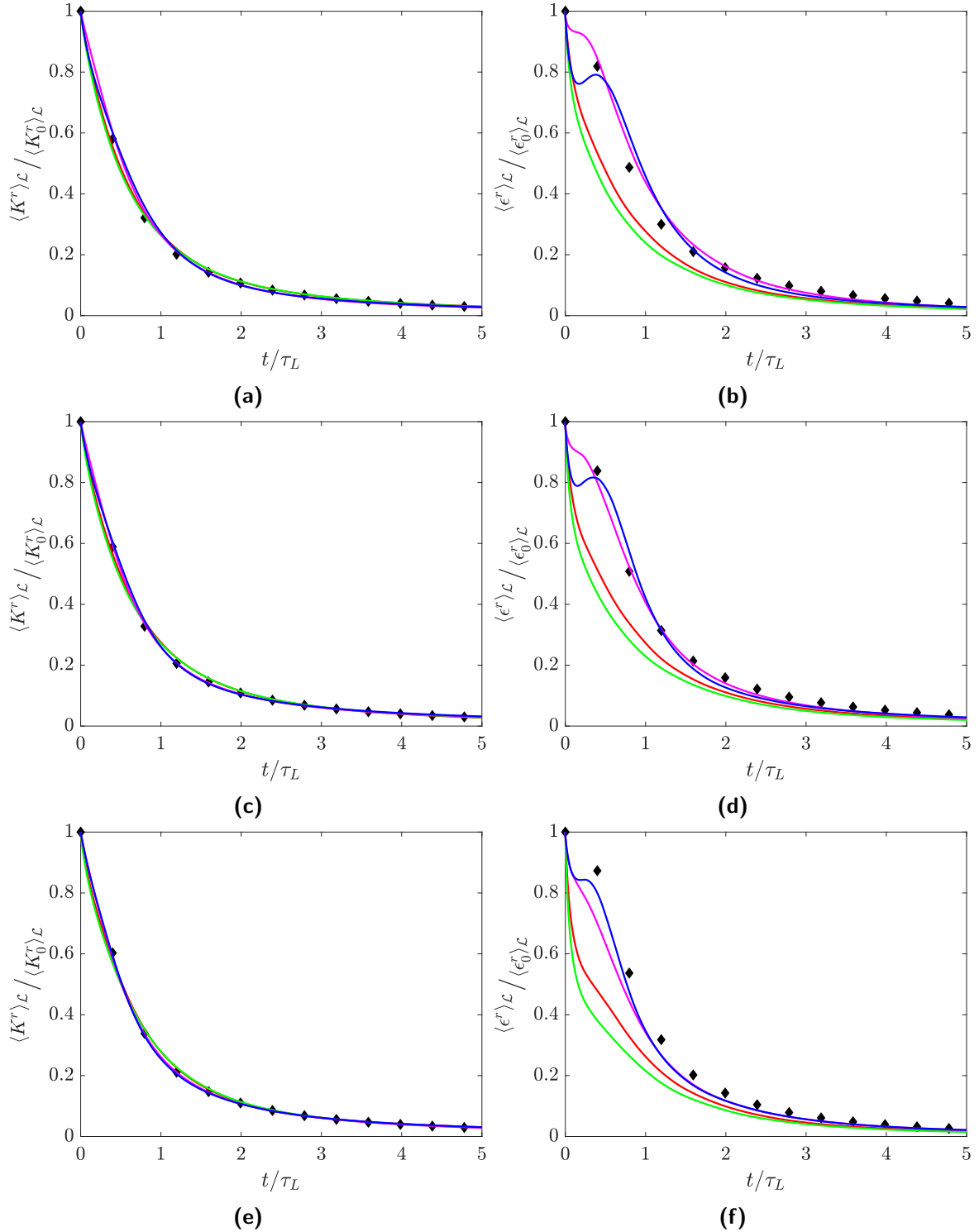


Figure 6.5: Evolution of (left) mean resolved kinetic energy, and (right) dissipation, non-dimensionalised with the corresponding initial value for decaying isotropic case obtained using different SGS model in LES plotted alongside the corresponding filtered DNS datapoints. From top to bottom are the results of LES run on a computation mesh with $N = 32^3$, 40^3 , and 64^3 . — DSM; — dynamic EASSM; — non-dynamic EASSM; — non-equilibrium EASSM; ◆ filtered DNS.

diction of resolved kinetic energy decay with DNS. Furthermore, we can also see from Fig. 6.5 (left) that, for all models, grid refinement does not to alter the prediction of the mean resolved kinetic energy decay appreciably.

The difference in the functioning of the different SGS models is more clearly captured in the evolution of the mean resolved kinetic energy dissipation, $\langle \varepsilon^r \rangle_{\mathcal{L}}$, plotted on the right in Fig. 6.5. Non-equilibrium and non-dynamic EASSMs record higher $\langle \varepsilon^r \rangle_{\mathcal{L}}$ than dynamic models throughout the simulation. For the coarser grids, i.e. $N = 32^3$ (Fig. 6.5b) and 40^3 (Fig. 6.5d), the non-dynamic EASSM captures the right level of $\langle \varepsilon^r \rangle_{\mathcal{L}}$ as the values show a good match with DNS. On these grids, the non-equilibrium model also shows close resemblance to DNS. A peculiarity in the decay of $\langle \varepsilon^r \rangle_{\mathcal{L}}$ for the non-equilibrium EASSM is the presence of a bump during the decay, when $t/\tau_L < 0.5$, that we see for all grids (see plots on right in Fig. 6.5). The reason for this lies in the formulation of k_{sgs} in non-equilibrium EASSM. From the initial value, as k_{sgs} in Eq. (2.40) starts to decay, when $t/\tau_L < 0.5$, it decays at a slightly faster rate compared the later part of transient ($t/\tau_L > 0.5$). As k_{sgs} drops rapidly, the SGS kinetic energy production \mathcal{P} also reduces in proportion. This results in a small increase in the energy of the modes closer to the cut-off wavenumber, or in other words, leads to a temporary accumulation of energy in the neighbourhood of κ_c . The energy accumulation is in turn reflected as a momentary increase in the resolved dissipation. With grid refinement, we see that the extent of the bump in the evolution of $\langle \varepsilon^r \rangle_{\mathcal{L}}$ reduces.

The dynamic models in Fig. 6.5 (right) record lower levels of $\langle \varepsilon^r \rangle_{\mathcal{L}}$ when compared to DNS. Just as observed for the forced isotropic case, for the decaying isotropic case as well, $\langle \varepsilon^r \rangle_{\mathcal{L}}$ obtained using dynamic EASSM is the lowest compared to other SGS models for all grid resolutions. Furthermore, with grid refinement, $\langle \varepsilon^r \rangle_{\mathcal{L}}$ for dynamic models deviate away from the corresponding DNS values.

6.3.2 Subgrid-scale quantities

The decay of mean SGS kinetic energy, $\langle k_{sgs} \rangle_{\mathcal{L}}$, estimated by the three EASSMs are plotted alongside the corresponding DNS values in Fig. 6.6. For the coarser meshes with $N = 32^3$, and 40^3 in Fig. 6.6a and 6.6b, non-dynamic EASSM gives better agreement with DNS than dynamic and non-equilibrium EASSMs. Non-equilibrium and dynamic EASSMs promote a faster decay of SGS kinetic energy compared to DNS, with the non-equilibrium model showing the highest rate of initial decay during $t/\tau_L < 0.7$ compared to DNS and other EASSMs. However, for non-equilibrium EASSM, with grid refinement, the duration of the accelerated decay phase (of $\langle k_{sgs} \rangle_{\mathcal{L}}$) reduces, as a result of which, the deviation of the modelled $\langle k_{sgs} \rangle_{\mathcal{L}}$ from DNS also becomes lower. On the other hand, dynamic EASSM seems to be relatively insensitive to grid refinement.

In Fig. 6.6, for non-equilibrium EASSM, the rapid decay of the SGS kinetic energy is followed by a readjustment of the decay rate to better resemble the DNS values. This transition or readjustment can be seen as a small bump in the evolution of $\langle k_{sgs} \rangle_{\mathcal{L}}$ in Fig. 6.6 for all grids. As mentioned in the previous section, this transition is also the reason for the abnormality in the evolution of the mean resolved kinetic energy dissipation in Fig. 6.5 (right). In order

to show the effect of this on SGS kinetic energy production and the resolved kinetic energy dissipation, we plot $\langle k_{sgs} \rangle_{\mathcal{L}}$, $\langle \mathcal{P} \rangle_{\mathcal{L}}$, and $\langle \varepsilon^r \rangle_{\mathcal{L}}$ obtained using non-equilibrium models for the grid with $N = 32^3$ in Fig. 6.7. We can clearly see that as the mean SGS kinetic energy drops rapidly, so does the mean SGS kinetic energy production. When the model readjusts itself to correct the rate of decay, the resolved dissipation increases momentarily until the energy that is accumulated in the neighbourhood of κ_c is dissipated. The region where this occurs is highlighted in grey in Fig. 6.7.

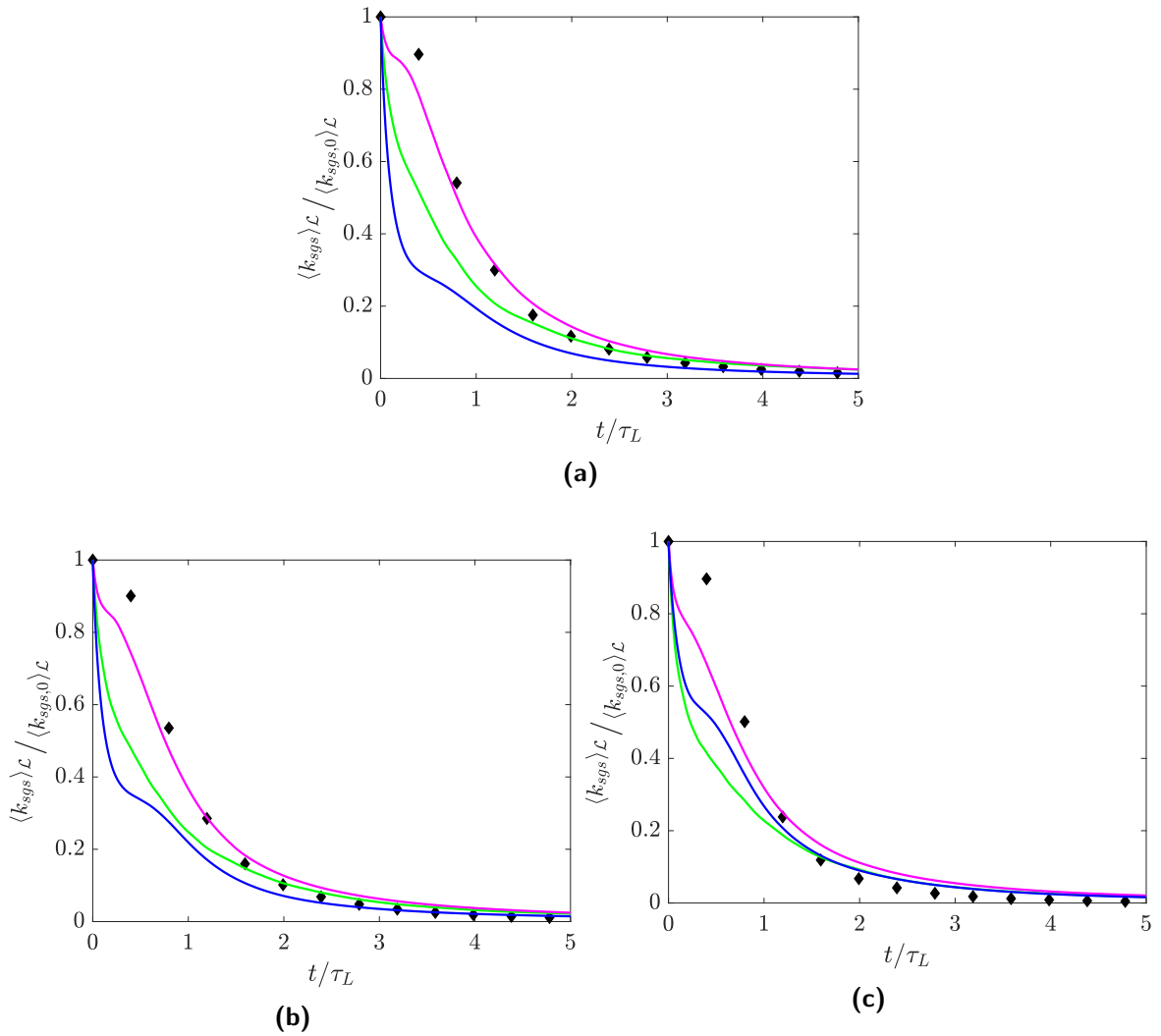


Figure 6.6: Isotropic decay of mean subgrid-scale kinetic energy obtained for LES and filtered DNS. (a) $N = 32^3$, (b) 40^3 , and (c) 64^3 . — dynamic EASSM; — non-dynamic EASSM; — non-equilibrium EASSM; ◆ filtered DNS.

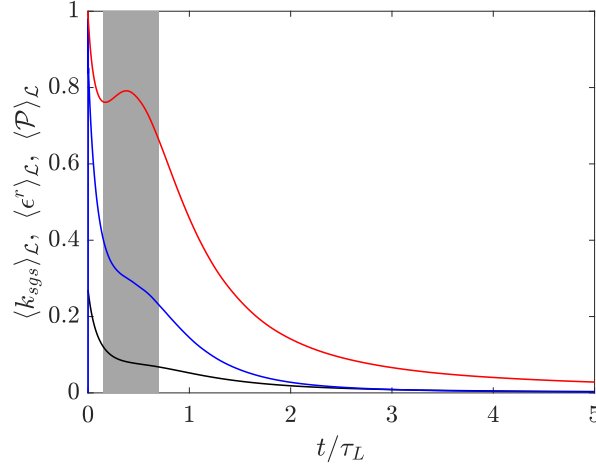


Figure 6.7: The decay of resolved kinetic energy dissipation, SGS kinetic energy and production for LES with non-equilibrium EASSM on grid $N = 32^3$. —SGS kinetic energy; —SGS kinetic energy production; —resolved dissipation.

6.4 Homogeneously decaying rotating turbulence

So far in this chapter, we have only considered isotropic cases in the absence of system rotation. To study the behaviour of the models under rotation, we simulate homogeneous decaying turbulence under strong rotation, with Ω_s chosen such that $\kappa_\Omega = 32$. The corresponding value of Ro (Eq. (2.45)) for the simulations, computed based on the initial solution state from DNS is 0.02. For the dynamic and non-dynamic EASSMs, the effect of the modifications suggested by Marstorp et al. (2009) in the presence of system rotation (Eq. 2.44) are also examined.

6.4.1 Resolved quantities

Before we move on to analysing the evolution of the mean resolved kinetic energy and dissipation obtained using the different SGS models, we first demonstrate the effect of the rotation modification (Eq. (2.44)) for dynamic and non-dynamic EASSM. For this purpose, we perform LES using both modified and unmodified dynamic and non-dynamic EASSMs on the computational grid with $N = 32^3$. The decay of $\langle K^r \rangle_{\mathcal{L}}$ and $\langle \varepsilon^r \rangle_{\mathcal{L}}$ obtained for the models are shown in Fig. 6.8. The modification is intended to suppress SGS kinetic energy production, thereby reducing the rate of resolved kinetic energy decay. In Fig. 6.8a, we see that, for non-dynamic EASSM, the modification leads to a very highly inhibited decay of resolved kinetic energy. In order to gain an understanding of the extent of inhibition induced by the modification, Fig. 6.8a also shows the decay of $\langle K^r \rangle_{\mathcal{L}}$ for LES with no SGS model. The modification, when applied to non-dynamic EASSM makes the model inactive, and as a result, we see that decay rate for modified non-dynamic EASSM is identical to the decay rate obtained when no SGS model is used. The effect of modification for non-dynamic EASSM is also clearly captured in the evolution of resolved kinetic energy dissipation in Fig. 6.8b. The surge in the resolved

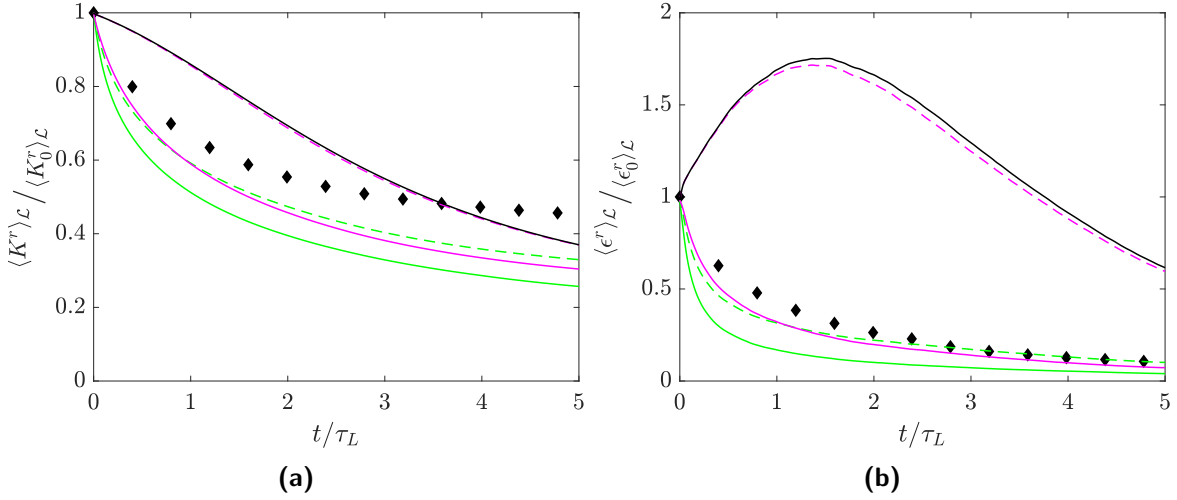


Figure 6.8: The evolution of the (a) mean resolved kinetic energy and (b) dissipation for the case of decaying turbulence under strong system rotation predicted by the differences SGS models with and without modifications. The LES are performed on a grid with $N = 32^3$. — dynamic EASSM; - - - modified dynamic EASSM; — non-dynamic EASSM; - - - modified non-dynamic EASSM; — no model; \blacklozenge filtered DNS.

kinetic energy dissipation during the initial phase also indicates that the transfer of kinetic energy from the resolved to the SGS (or \mathcal{P}) provided by the modified non-dynamic EASSM is highly suppressed. As a result, kinetic energy accumulates in the wavenumbers close to the edge of the resolved spectrum leading to an increase in the resolved dissipation.

For the dynamic EASSM, the modification does not induce the right level of inhibition required in order to reproduce the decay rate of $\langle K^r \rangle_{\mathcal{L}}$ obtained in DNS. Nevertheless, from Fig. 6.8, it can be seen that the modified dynamic EASSM shows a closer agreement with DNS in Fig. 6.8 than the unmodified version. The difference between the dynamic and the non-dynamic EASSMs lies in the determination of k_{sgs} , τ^* , and C_1 . In the case of dynamic EASSM, the modification does not affect any of these variables directly. It only has a direct effect on the coefficients, $G^{(1)}$ and $G^{(2)}$ in the equation for τ_{ij} (Eq. (2.37)). On the other hand, for the non-dynamic EASSM, the modification directly affects k_{sgs} and C_1 as well, suppressing them drastically. Therefore, based on the results in Fig. 6.8, for comparing the decay of mean resolved quantities, we will only use

- dynamic Smagorinsky model,
- modified dynamic EASSM (will just be called dynamic EASSM for the remainder of this section),
- unmodified non-dynamic EASSM (will just be called non-dynamic EASSM for the remainder of this section), and
- non-equilibrium EASSM.

The evolution of the mean resolved kinetic energy obtained for the different models are shown

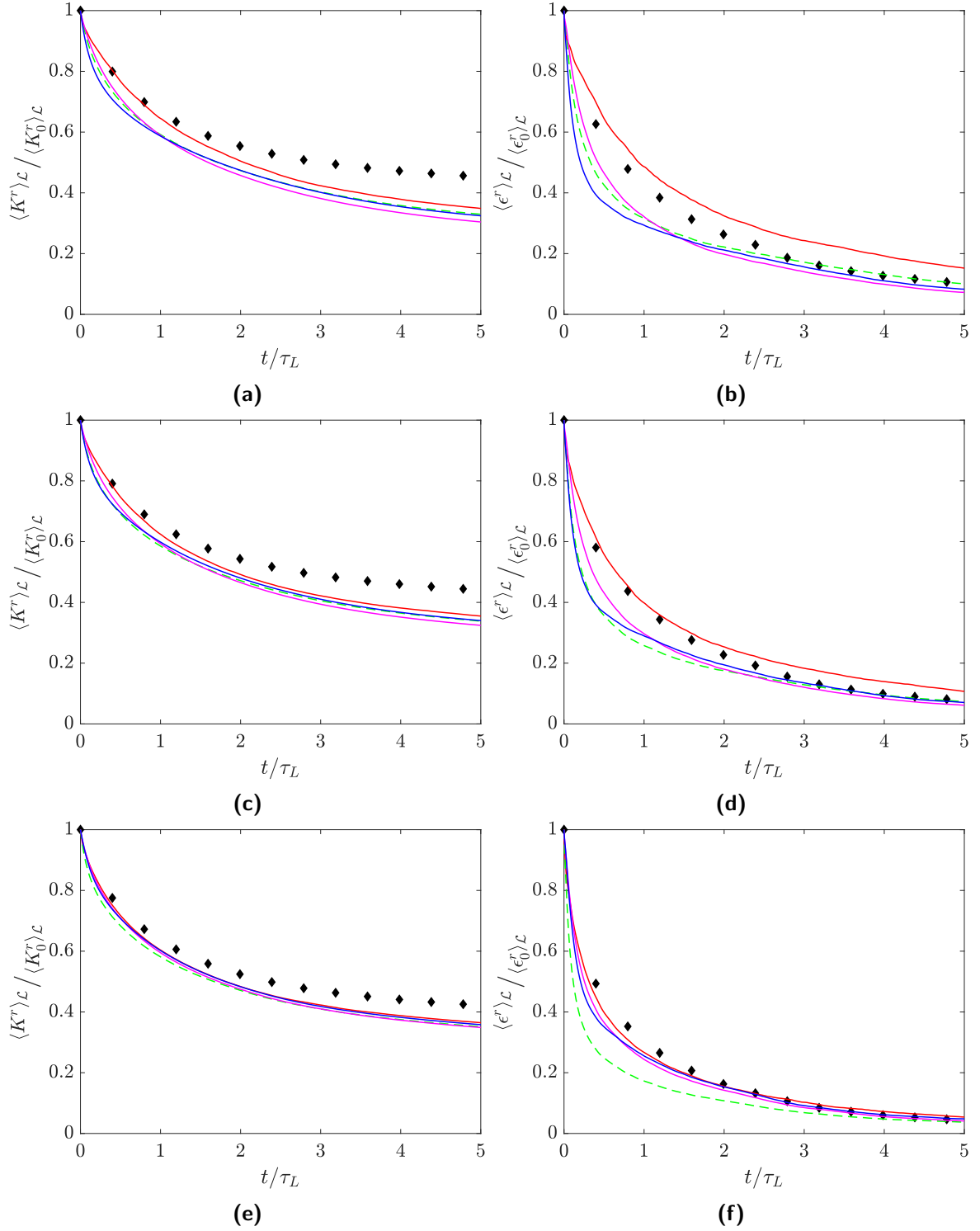


Figure 6.9: Evolution of (left) mean resolved kinetic energy, and (right) dissipation, non-dimensionalised with the corresponding initial value for decaying case under strong rotation, obtained using different SGS model in LES plotted alongside the corresponding filtered DNS datapoints. From top to bottom are the results of LES run on a computation mesh with $N = 32^3$, 40^3 , and 64^3 . — DSM; - - - modified dynamic EASSM; — non-dynamic EASSM; — non-equilibrium EASSM; ◆ filtered DNS.

on the left in Fig. 6.9. Compared to the results for the isotropic cases, strong rotation makes all the models behave poorly. During the initial phase of decay, during $t/\tau_L < 1$, we see in Fig. 6.9a, and 6.9b that DSM gives a good match with DNS for $N = 32^3$ and 40^3 . After $t/\tau_L \sim 1$, DSM dissipates excessively compared to DNS, and as a result, $\langle K^r \rangle_{\mathcal{L}}$ does not saturate at the right value (DNS) but instead decays further. For the coarser meshes, the EASSMs predict a faster rate of decay, at the initial phase $t/\tau_L < 1$ when compared to DSM and DNS. During this phase, non-equilibrium EASSM shows the highest rate of decay of $\langle K^r \rangle_{\mathcal{L}}$. The difference between the different models in terms of evolution of $\langle K^r \rangle_{\mathcal{L}}$ becomes less prominent with grid refinement. In Fig. 6.9e (for $N = 64^3$), we see that all SGS models provide an almost similar rate of decay for the mean resolved kinetic energy.

The corresponding plots for mean resolved dissipation are shown on the right in Fig. 6.9. It can be seen in Fig. 6.9b and 6.9d that using DSM results in a higher level of dissipation than DNS on coarser meshes with $N = 32^3$, and 40^3 . The values for EASSMs are lower than DNS at all grid resolutions. Also from Fig. 6.9b and 6.9d, we see that non-equilibrium model shows the least amount of $\langle \varepsilon^r \rangle_{\mathcal{L}}$ in the initial phase until $t/\tau_L \sim 1$ (for $N = 32^3$ and 40^3). With grid refinement, the values of $\langle \varepsilon^r \rangle_{\mathcal{L}}$ for non-equilibrium model surpasses dynamic EASSM to give closer resemblance to DNS.

6.4.2 Subgrid-scale quantities

We briefly discuss the effect of the modification on the mean SGS kinetic energy evolution for dynamic and non-dynamic EASSMs. Figure 6.10 shows the evolution of $\langle k_{sgs} \rangle_{\mathcal{L}}$ for $N = 32^3$, obtained with modified and unmodified EASSMs. As mentioned earlier, the modifications do

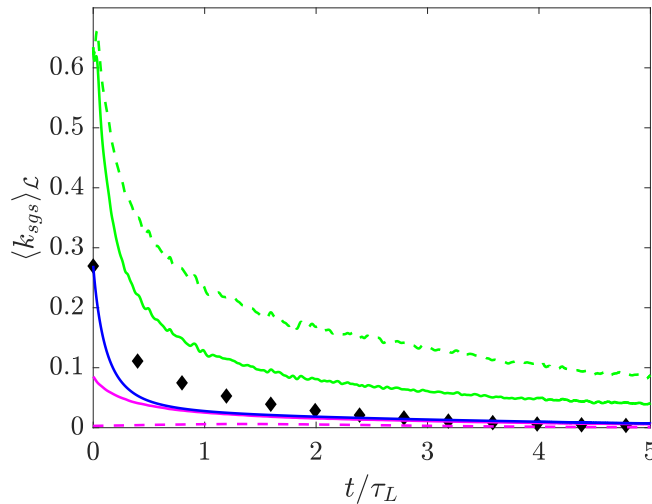


Figure 6.10: The evolution of the mean SGS kinetic energy for EASSMs for the case of turbulence decaying with strong system rotation predicted by the different SGS models with and without any modifications. The LES are performed on a grid with $N = 32^3$. — dynamic EASSM; --- modified dynamic EASSM; — non-dynamic EASSM; --- modified non-dynamic EASSM; — no model; ◆ filtered DNS.

not directly affect the determination of SGS kinetic energy for the dynamic case, while for the non-dynamic version, k_{sgs} has an explicit dependence of $G^{(1)}$ that lowers its value. It becomes clear from Fig. 6.10 that the modification for non-dynamic EASSM suppresses the $\langle k_{sgs} \rangle_{\mathcal{L}}$ to almost negligible values compared to other models and DNS. This also explains the close resemblance between LES with no model and the modified non-dynamic EASSM seen in Fig. 6.8. The same modification has an opposite effect on k_{sgs} evolution for the dynamic EASSM as it reduces the rate of decay of $\langle k_{sgs} \rangle_{\mathcal{L}}$ or in other words provides an increased level $\langle k_{sgs} \rangle_{\mathcal{L}}$. This is a result of the dynamic procedure. Suppressing the value of $G^{(1)}$ results in reducing the SGS kinetic energy production, which consequently lowers the rate of decay of $\langle K^r \rangle_{\mathcal{L}}$. Since the dynamic procedure creates a dependence of k_{sgs} on the resolved energy spectrum through the determination of the dynamic constant, we see the increase in the level of $\langle k_{sgs} \rangle_{\mathcal{L}}$ for modified dynamic EASSM.

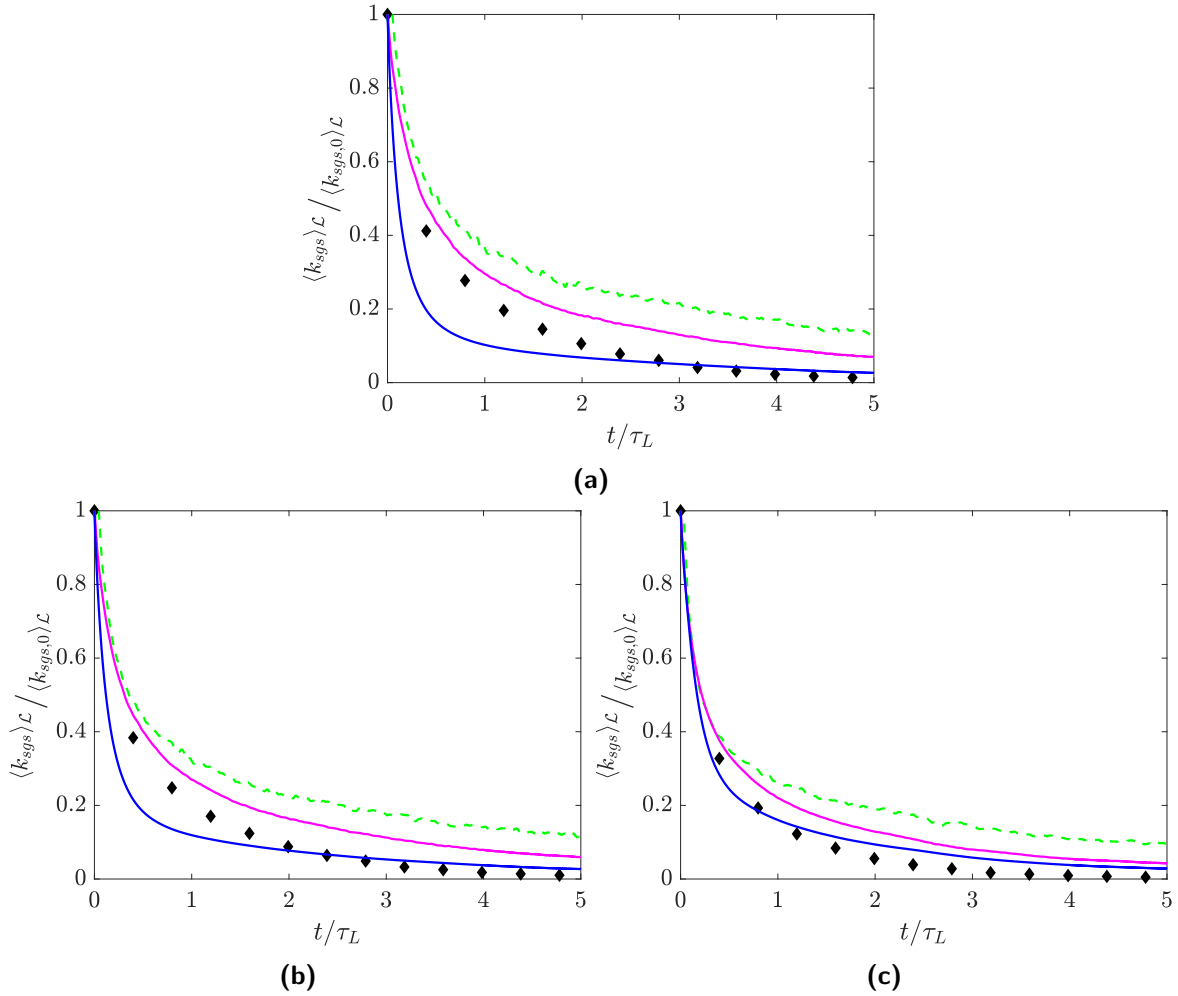


Figure 6.11: Decay of mean subgrid-scale kinetic energy under strong rotation obtained for LES and filtered DNS. (a) $N = 32^3$, (b) 40^3 , and (c) 64^3 . --- dynamic EASSM; — non-dynamic EASSM; — non-equilibrium EASSM; ◆ filtered DNS.

We now move on to examining the evolution of $\langle k_{sgs} \rangle_{\mathcal{L}}$ on different grids for LES performed using (modified) dynamic EASSM, (unmodified) non-dynamic EASSM and non-equilibrium EASSM. The corresponding values are plotted in Fig. 6.11. The decay rates from DNS are not matched by any of the models. Dynamic and non-dynamic EASSMs predict a slower initial rate of decay of SGS kinetic energy while the non-equilibrium model seems to overpredict the initial rate of decay. With grid refinement, dynamic and non-dynamic EASSMs do not show any appreciable improvement in the values of mean k_{sgs} . For grid with $N = 64^3$, the non-equilibrium model gives a closer prediction of the initial rate of decay that we observe in DNS. Another consequence of using purely algebraic closures for k_{sgs} in non-dynamic and dynamic EASSMs is that k_{sgs} becomes zero only when all the resolved scales have decayed completely (see k_{sgs} formulation in Tab. 2.3). This is also shown in Fig. 6.11 where we see that at the end of transient, the values of $\langle k_{sgs} \rangle_{\mathcal{L}}$ predicted by dynamic and non-dynamic EASSMs are much higher than DNS for all grids.

6.5 Special attention to subgrid-scale evolution in homogeneously decaying rotating turbulence

From the discussion so far, it is evident that non-equilibrium EASSM gives fairly good predictions of resolved and SGS quantities for forced and decaying cases when turbulence is isotropic. However, under anisotropic conditions, the presence of strong rotation deteriorates the model behaviour severely. In order to understand the reason for deterioration, in the current section we examine the behaviour of the SGS in homogeneously decaying turbulence under rapid rotation. In this way we state the possible reason behind the poor performance of the non-equilibrium model seen in the previous section. This analysis will be done using DNS results for the decaying cases.

Firstly, we start by providing a direct comparison between the two cases of decaying turbulence: with and without system rotation. The evolution of the mean SGS kinetic energy and dissipation are shown in Fig. 6.12. The values shown are computed from DNS using a spectral cut-off filter of dimension $\kappa_c = 16$.

From Fig. 6.12, we see that rotation accelerates the initial decay of mean SGS kinetic energy and dissipation. The rate of decay of SGS kinetic is directly dictated by the difference in SGS kinetic energy production and dissipation. It is well known that rotation suppresses the rate of decay of the total turbulent kinetic energy (Traugott (1958)), which is brought about by a suppressed total turbulent kinetic energy dissipation (Bardina et al. (1985)). As the SGS are primary considered to be dissipative in nature, it is reasonable to expect the dissipation in the SGS to also reduce with rotation. This is in-fact the reason why the total dissipation becomes reduced. We see this effect in Fig. 6.12b, where the SGS kinetic energy dissipation for the rotating case is lower than for the non-rotating case. Therefore, from an LES standpoint, both resolved (Fig. 6.9, and 6.5) and SGS kinetic energy dissipation reduces with increase in rotation. This leads to an overall decrease in the total dissipation of decaying rotating turbulence.

As mentioned earlier, rotation brings about a reduced rate of decay of total turbulent kinetic energy. However, from Fig. 6.12a, the mean SGS kinetic energy seems to record a faster initial rate of decay with rotation. Given that the total SGS kinetic energy dissipation becomes suppressed with rotation, this seems rather counter-intuitive. An explanation for this lies in the evolution of the SGS kinetic energy production. Rotation suppresses the energy cascade leading to a reduced transfer of energy from the resolved to the SGS, or in other words a lower net SGS kinetic energy production. The evolution of this quantity for rotating and non-rotating case is shown in Fig. 6.13a. It is evident that the rotating case records a lower level of mean SGS kinetic energy production when compared to the non-rotating case. The increased initial rate of decay of mean k_{sgs} is indeed a result of suppressed SGS kinetic energy production. Since the total mean \mathcal{P} acts as a source in the evolution equation for k_{sgs} , the suppression of this quantity results in an increase in the rate of decay of $\langle k_{sgs} \rangle_{\mathcal{L}}$ during the initial phase of decay as also seen in Fig. 6.13b.

The suppression of the total energy cascade during rotation is closely related to the increase in the amount of backscatter of energy from small scales to the larger scales. In LES, the cascade of energy (both forward and backward) that happens within the resolved scales does not require any special attention. On the other hand, when this energy transfer happens across κ_c , the SGS models must be capable of capturing the resulting dynamics. Figure 6.14 show the transfer of energy across κ_c . It is obtained by collecting the positive and negative values of \mathcal{P} obtained over the domain and averaging them over the entire volume. The positive values (\mathcal{P}^+) indicate the net transfer of energy from the resolved scales to the SGS while the negative values (\mathcal{P}^-) suggest the backscatter of energy from the SGS to the resolved scales. During the initial phase of decay, it can be seen that the mean value of \mathcal{P}^+ reduces for the rotating case when compared to the non-rotating case. Also, we see that the amount of backscatter during this initial phase is lower for rotating case when compared to the non-rotating case. In order to understand this behaviour, we have to first look at how rotation

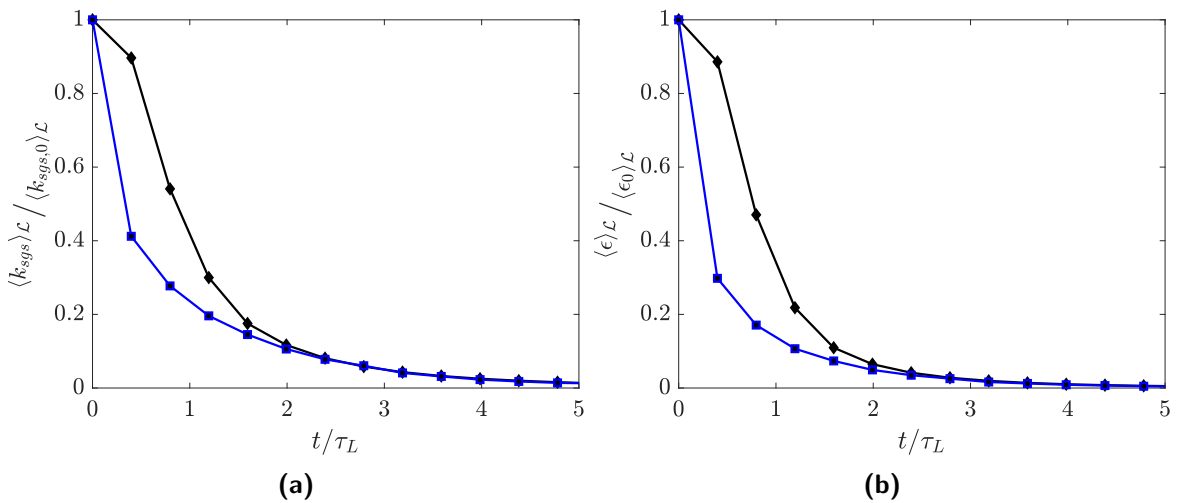


Figure 6.12: The evolution of the (a) mean SGS kinetic energy and (b) dissipation for the case of turbulence decaying with and without strong system rotation obtained from filtering DNS using a spectral cut-off filter with $\kappa_c = 16$. \blacklozenge isotropic; \blacksquare with rotation.

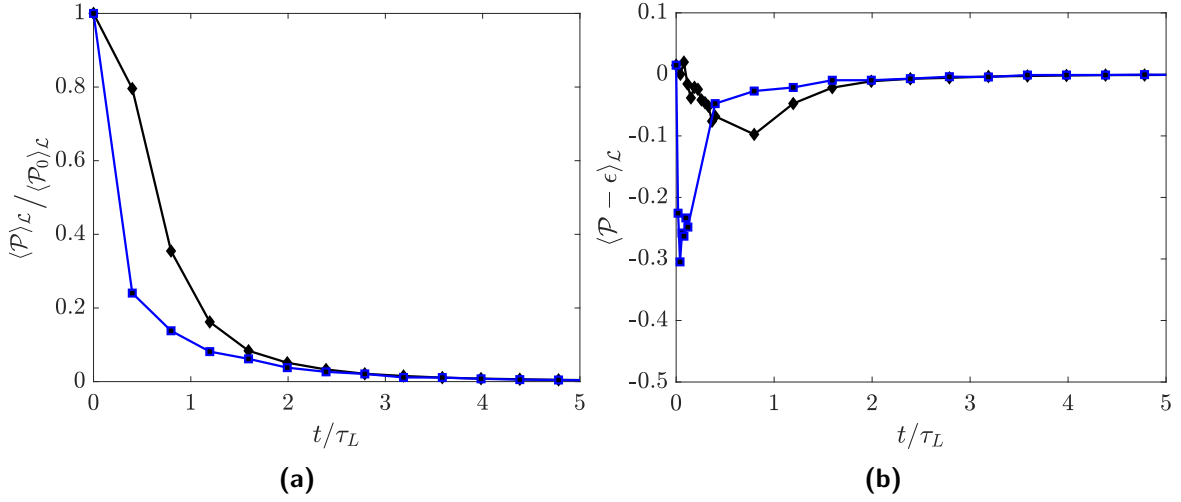


Figure 6.13: The evolution of the (a) mean SGS kinetic energy production and (b) decay rate for decaying turbulence with and without strong system rotation obtained from filtering DNS using a spectral cut-off filter with $\kappa_c = 16$. \blacklozenge isotropic; \blacksquare with rotation.

affects the different modes of turbulence for our case. When a initially homogeneous isotropic turbulence is imparted with system rotation and allowed to decay, the Zeman wavenumber that indicates the highest wavenumber affected by rotation increases as the total dissipation reduces during decay. Furthermore, this is accompanied by an increase of the Kolmogorov length scale. These characteristics are shown in Fig. 6.15. As a result, the proportion of the SGS affected by rotation increases with time. However, during the initial phase, rotation has a stronger effect on the resolved scales than the SGS. The inverse transfer of energy within the different mode of the resolved spectrum increases, leading to a reduced forward transfer

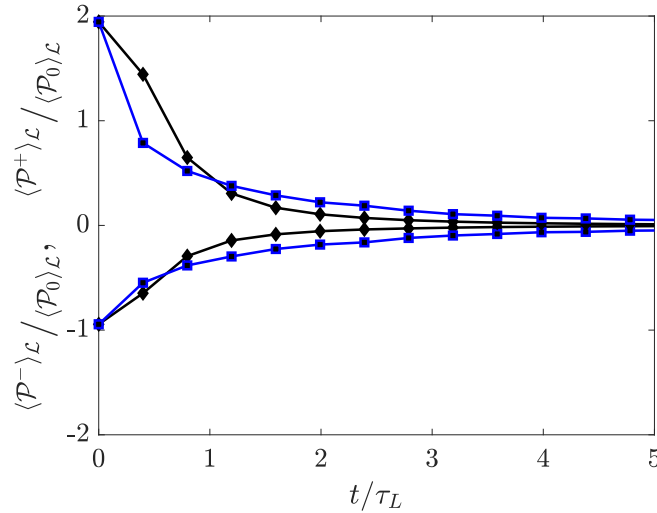


Figure 6.14: The evolution of the mean forward (resolved to SGS) and backward (SGS to resolved scales) transfer of kinetic energy for decaying turbulence with and without strong system rotation obtained from filtering DNS using a spectral cut-off filter with $\kappa_c = 16$. \blacklozenge isotropic; \blacksquare with rotation.

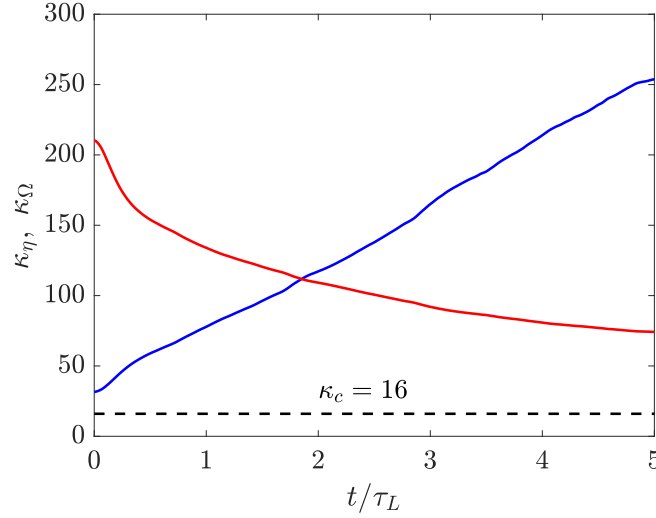


Figure 6.15: The evolution of the Zeman wavenumber κ_Ω and the wavenumber corresponding the Kolomogorov length scale κ_η in decaying turbulence with rotation, computed from DNS. — κ_η , — κ_Ω .

of energy to the SGS. As the turbulence decays, rotation increases the transfer of energy from the SGS to the resolved thereby eventually showing higher levels of backscatter when compared to the non-rotating case.

6.5.1 Alternative scaling for SGS kinetic energy dissipation

Under the framework of non-equilibrium EASSM, the evolution of k_{sgs} can be controlled by the modelling of the SGS kinetic energy dissipation. This term also has an effect on the SGS kinetic energy production through the formulation of τ^* (in Eq. (5.16)). The two phases of decay of k_{sgs} : the initial rapid decay and the subsequent reduction in the rate of decay are not well captured by the current scaling that we used for modelling the SGS kinetic energy dissipation. Therefore we suggest exploring other modelling approaches for ε that can include the rate of system rotation explicitly into the formulation, i.e.

$$\varepsilon^{mod} \sim \Omega_s^a \Delta^b k_{sgs}^c. \quad (6.2)$$

As we require ε to increase the rate of decay of k_{sgs} with increase in the rotation rate of the system, we require a direct proportionality between these two terms. Hence we fix positive values of a . Some scaling laws which fulfil this criteria are listed in Tab. 6.2

Table 6.2 covers a limited range of models for the SGS kinetic energy dissipation. We recommend that these models to be used in combination to Eq. (2.39), that we current use. Thereby, as Ω_s becomes zero, we recover the isotropic modelling. However, more extensive investigation into the modelling of the SGS kinetic energy dissipation in rapidly rotating flows in required is order to make the right choice of model.

a	b	c	ε^{mod}
1/3	-2/3	4/3	$\Omega_s^{1/3} \Delta^{-2/3} k_{sgs}^{4/3}$
1/2	-1.2	5/4	$\Omega_s^{1/2} \Delta^{-1/2} k_{sgs}^{5/4}$
1	0	1	$k_{sgs} \Omega_s$
2	1	1/2	$\Omega_s^2 \Delta k_{sgs}^{1/2}$
0	-1	1.5	$k_{sgs}^{3/2} \Delta^{-1}$ (isotropic scaling)

Table 6.2: A few suggestions for different scaling laws that could be applicable to rotating homogeneous turbulence for modelling the SGS kinetic energy dissipation.

Chapter 7

Conclusions And Recommendations

The characteristic features of turbulence energy spectrum such as, $\kappa^{-5/3}$ scaling of the inertial range and the isotropic nature of the small scales do not apply when turbulence is subject to strong rotation. As intriguing as rotating turbulence is to study, it is also equally challenging to develop SGS stress models for LES, that can accurately capture the ensuing dynamics of the SGS. In this thesis, we studied the performance of (linear) DSM, (non-linear) dynamic, and non-dynamic EASSMs for both rotating and non-rotating cases of homogeneous turbulence. Based on observations in a priori investigations, we proposed a new formulation of EASSM, which we believe gives a more physical description of SGS in homogeneous flows. The new model is subsequently tested in comparison with other models for different rotating and non-rotating cases of turbulence. The main conclusions derived along the way and the recommendations for future work are discussed in the current chapter.

7.1 Conclusions

7.1.1 A priori studies

We first started by performed a priori investigations on the performance of different models. DNS were conducted on forced homogeneous turbulence for three cases, which were without rotation, with weak, and strong rotation. The rotation setting for the weakly and strongly rotating cases were such that the $\kappa_{\Omega} < \kappa_c$ and $\kappa_{\Omega} > \kappa_c$, respectively. We observed that strong rotation leads to a suppressed evolution of turbulent kinetic energy as a result of reduction in the total kinetic energy dissipation. The one-dimensional energy spectrum showed an altered wavenumber scaling of energy distributed among parallel and perpendicular modes (to the rotation vector). Furthermore, the three-dimensional energy spectrum showed a κ^{-2} scaling of the intermediate modes for the rotating case which differs from the $\kappa^{-5/3}$ scaling observed for the isotropic case.

The forced simulations were run until turbulent kinetic energy exhibited steady-state behaviour, at which point the solution was filtered using a box filter to the LES grid dimensions ($\kappa_c = 10$) in order to examine the different modelling approaches. For EASSMs, the inclusion of the non-linear term in the formulation of SGS stresses lead to an increase in the overall correlation between the modelled and the actual SGS stress tensor, when compared to the corresponding correlations observed for DSM. This became more evident for strongly rotating case, where the DSM gave low values of correlation for the SGS stress anisotropy. The EASSMs on the other hand, preserved the same level of correlation for the normal SGS stress components as for the non-rotating case. In addition, we also examined the modelling of SGS kinetic energy production. The non-linearity in EASSM does not contribute to the modelling of the SGS kinetic energy production, \mathcal{P} . As a result, we observed more or less similar levels of correlation between the modelled and the actual \mathcal{P} for the dynamic SGS models. For the non-dynamic EASSM, the poor modelling of the SGS kinetic energy when compared to the dynamic version lead to a deterioration in the correlation for the modelled SGS kinetic energy production.

As the pressure-strain term is crucial in an EASSM, the performance of LRR-IP, QI, and SSG models were tested a priori on the basis of the correlation coefficients. The linear LRR models showed better levels of correlation when compared to the non-linear SSG model in the isotropic and the weakly rotating cases. However, under strong rotation, the correlation between the modelled and the actual pressure-strain became almost completely non-existent for all the models. It was found that the main cause for deterioration of the correlation coefficients under strong rotation is due to poor modelling of the rapid pressure-strain term. The rapid terms modelled using the LRR and the SSG models were uncorrelated with the terms computed from DNS for the strongly rotating case. For the modelled slow pressure-strain term, on the other hand, the correlation coefficients, despite being low ($\sim 20\%$) even in the isotropic case were more or less maintained for the normal components in strongly rotating case as well.

Finally, in order to test the validity of the perfect equilibrium assumption between the SGS kinetic energy production and dissipation that is used in the development of the dynamic and the non-dynamic EASSMs (Marstorp et al. (2009)), the corresponding PDFs for the different cases were examined. For the isotropic case, the calibration of \mathcal{P}/ε to 1 is acceptable as the peak in the PDF was observed at ~ 0.9 . On the other hand, for the non-rotating case, the peak in the PDF for \mathcal{P}/ε was found to be at ~ 0.3 . For strongly rotating case, the PDFs also indicated the presence of heavier tails. This indicates that \mathcal{P}/ε for the strongly rotating case is more intermittent when compared to the non-rotating case. The use of the perfect equilibrium assumption, although simplifies the EASSM, poses as a limitation, as it assumes that all SGS instantly adapt to the resolved quantities. Therefore, a formulation of EASSM that does not involve the prior calibration of \mathcal{P}/ε to 1 were sought out.

7.1.2 A new formulation of explicitly algebraic subgrid-scale stress model

The ratio of SGS kinetic energy production to dissipation, \mathcal{P}/ε , can be treated as a scalar parameter that gives an indication of the local imbalance between between \mathcal{P} and ε . If we

assume that this imbalance evolves slowly in time, at a given time step t_i the value of \mathcal{P}/ε computed at the previous time step t_{i-1} can be used. In other words, the ratio \mathcal{P}/ε is ‘calibrated’ with its value at the previous time step. Based on this reasoning, we derived an expression for modelled SGS stress tensor where the ratio of \mathcal{P}/ε is retained in the formulation. Furthermore, avoiding the assumption that $\mathcal{P} = \varepsilon$ also enabled us to solve a modelled evolution equation for determining the SGS kinetic energy. This new formulation of EASSM was termed as the non-equilibrium EASSM and was subsequently tested in comparison with DSM, dynamic, and non-dynamic EASSMs for different homogeneous cases of turbulence.

7.1.3 A posteriori studies

LES were carried out using DSM, dynamic, non-dynamic, and non-equilibrium EASSMs. Forced (isotropic) and decaying (with and without rotation) cases were studied at different grid resolutions and the evolution of different quantities in the LES were compared with the corresponding values computed from the DNS. For the forced isotropic case, the use of the evolution equation for k_{sgs} and not assuming that $\mathcal{P} = \varepsilon$, resulted in a very good prediction of the transient nature of the mean resolved and SGS quantities. The other models, though they predicted the right steady state value of mean resolved kinetic energy, did not bare good resemblance of transient evolution of the mean resolved kinetic energy and dissipation as in the DNS. Furthermore, for the mean SGS kinetic energy evolution, the algebraic formulation of k_{sgs} for the dynamic and the non-dynamic EASSMs lead to an immediate growth of the SGS from the start of the simulation, while delayed growth of the SGS kinetic energy observed from DNS was very well captured by the non-equilibrium EASSM.

For the isotropic decaying case, in the evolution of the mean resolved kinetic energy, all the models more or less gave good resemblance to the DNS. The difference in the performance of the models became evident when comparing the values of the mean resolved kinetic energy dissipation. The non-dynamic EASSM showed good resemblance to DNS while for the non-equilibrium EASSM, we observed a bump in the transient. This is attributed to the rapid decay of the SGS kinetic energy. The accelerated decay of the modelled SGS kinetic energy at the initial phase of the simulation leads to a sudden drop in the value of SGS kinetic energy production. This in-turn leads to an accumulation of energy in the modes close to κ_c in the resolved spectrum, which is reflected as a momentary increase in the resolved dissipation. The dynamic models showed lower levels of mean resolved kinetic energy dissipation throughout the simulation and did not improve with grid resolution.

Finally, we examined the performance of the different modelling approaches for the case of decaying turbulence under strong rotation. The modification for the system rotation reduces the SGS kinetic energy for the non-dynamic EASSM to very low values, and therefore, the results obtained were similar to the LES performed without any SGS models. For the dynamic EASSM, the modification suppresses the decay of mean resolved kinetic energy, however, compared to DNS, the decay rate was still found to be higher than DNS for the dynamic EASSM. Also, the non-equilibrium EASSM captured a very similar evolution of mean resolved kinetic energy as obtained from the other SGS models. With regard to the mean SGS kinetic energy evolution, the non-equilibrium EASSM predicted a higher rate of initial decay than

observed from the DNS. The prediction of the non-equilibrium model improved with grid refinement. For the dynamic and non-dynamic EASSMs, the initial rate of decay was found to be lower than DNS. Also, these models did not show any improvement with grid refinement.

7.1.4 Behaviour of SGS in decaying turbulence with and without rotation

The SGS models perform do not perform as well in the decaying case with rotation as they do for the non-rotating case. In order to understand the cause for the deterioration, the evolution of the actual SGS quantities, computed from DNS, were analysed. It became evident that the SGS kinetic energy shows an accelerated initial rate of decay in the rotating case, when compared to the non-rotating case. It was also seen that the SGS kinetic energy dissipation is drastically reduced under rotation. The accelerated rate of decay of mean SGS kinetic energy is an effect of a quick drop in the level of SGS kinetic energy production. As the mean SGS kinetic energy production acts as a source term in the evolution of mean SGS kinetic energy, a strong suppression in its value causes SGS kinetic energy to decay quickly. Furthermore, it was found that the increase in the transfer of energy from the SGS to the resolved scales due to rotation does not occur right from the start (for the rotation setting chosen here). As the system decays, the Zeman wavenumber for the flow increases and the wavenumber computed based on the Kolmogorov wavenumber decreases. As a result, the effect of rotation on the SGS becomes stronger with time. Therefore, only as the simulation proceeds does the increased amount of backscatter from the SGS to the resolved scales become evident. Within the framework of non-equilibrium EASSM, a way to control the decay rate of the SGS and the resolved kinetic energy is by controlling the SGS kinetic energy dissipation. For rotating flows, a second term (in addition to the isotropic scaling used) in the modelling of SGS kinetic energy dissipation that has an explicit dependence of the system rotation rate was suggested to provide a desirable improvement for the non-equilibrium EASSM.

7.2 Recommendations

The modelling of the pressure-strain term in an EASSM is very crucial. While the LRR and the SSG models preserve a good level of correlation with the actual pressure-strain term for isotropic and the weakly rotating cases, we see their performance severely deteriorating for the strongly rotating cases. Therefore, more attention has to be given to the modelling of the pressure-strain, especially for the rapid term, such that it is more suited for strongly rotating flows.

In the evolution equation for k_{sgs} , the turbulent and the pressure transport terms are often (also as done here) modelled using a single gradient diffusion model. The counter-gradient hypothesis that underlies this approach seems to be valid even in strongly rotating flows. However, preliminary investigations from [Demuren et al. \(1994\)](#) from DNS on boundary layer flows indicate the need for separate modelling of the two quantities. In case of application of the current non-equilibrium models to such flow cases, for instance, we believe an additional model for pressure transport could improve the predictions.

The modelling of the SGS kinetic energy dissipation has a significant effect on the evolution of both the resolved and the SGS quantities. One could, in addition to solving the evolution equation for k_{sgs} , also solve an (empirical) evolution equation for ε . If a significant improvement is found in the results for the rotating cases, then this would motivate more extensive analyses in order to come up with the right scaling for the SGS kinetic energy dissipation by examining the DNS data for strongly rotating cases at different Rossby numbers.

Bibliography

- K. Akselvoll and P. Moin. Large-eddy simulation of turbulent confined coannular jets. *Journal of Fluid Mechanics*, 315:387–411, 1996.
- K. Alvelius. Random forcing of three-dimensional homogeneous turbulence. *Physics of Fluids*, 11(7):1880–1889, 1999.
- A. Asnagli. *Developing computational methods for detailed assessment of cavitation on marine propellers*. PhD thesis, Department of Shipping and Marine Technology, Chalmers University of Technology, 2015.
- J. S. Baggett, J. Jimenez, and A. G. Kravchenko. Resolution requirements in large-eddy simulations of shear flows. *Annual research briefs*, pages 51–66, 1997.
- J. Bardina, J. H. Ferziger, and W. C. Reynolds. *Improved turbulence models based on large eddy simulation of homogeneous, incompressible turbulent flows*. Stanford University, Report TF-19, 1983.
- J. Bardina, J. H. Ferziger, and R. S. Rogallo. Effect of rotation on isotropic turbulence: computation and modelling. *Journal of Fluid Mechanics*, 154:321–336, 1985.
- C. N. Baroud, B. B. Plapp, Z. She, and H. L. Swinney. Anomalous self-similarity in a turbulent rapidly rotating fluid. *Physical Review Letters*, 88(11):114501, 2002.
- S. Borchert, U. Achatz, S. Remmler, S. Hickel, U. Harlander, M. Vincze, K. D. Alexandrov, F. Rieper, T. Heppelmann, and S. I. Dolaptchiev. Finite-volume models with implicit subgrid-scale parameterization for the differentially heated rotating annulus. *Meteorologische Zeitschrift*, 2014.
- K. Choi and J. L. Lumley. The return to isotropy of homogeneous turbulence. *Journal of Fluid Mechanics*, 436:59–84, 2001.
- S. Choi and H. Kang. Numerical tests of Reynolds stress models in the computations of open-channel flows. In *Advances in fluid modeling and turbulence measurements*, pages 71–78. World Scientific, 2002.
- P. Y. Chou. On velocity correlations and the solutions of the equations of turbulent fluctuation. *Quarterly of Applied Mathematics*, 3(1):38–54, 1945.

- R. A. Clark, J. H. Ferziger, and W. C. Reynolds. Evaluation of subgrid-scale models using an accurately simulated turbulent flow. *Journal of Fluid Mechanics*, 91(1):1–16, 1979.
- C. B. da Silva and J. C. F. Pereira. Analysis of the gradient-diffusion hypothesis in large-eddy simulations based on transport equations. *Physics of Fluids*, 19(3):035106, 2007.
- C. B. da Silva, S. Rego, and J. C. F. Pereira. Analysis of the viscous/molecular subgrid-scale dissipation terms in LES based on transport equations: A priori tests. *Journal of Turbulence*, (9):N25, 2008.
- P. Davidson. *Turbulence: an introduction for scientists and engineers*. Oxford University Press, USA, 2004.
- A. O. Demuren, S. K. Lele, and P. Durbin. Role of pressure diffusion in non-homogeneous shear flows. *Proceedings of the 1994 Summer Program*, pages 313–321, 1994.
- C. Egerer, S. Hickel, S. Schmidt, and N. A. Adams. Les of temporally evolving turbulent cavitating shear layers. In *High Performance Computing in Science and Engineering 14*, pages 367–378. Springer, 2015.
- V. Eswaran and S. B. Pope. An examination of forcing in direct numerical simulations of turbulence. *Computers & Fluids*, 16(3):257–278, 1988.
- C. Fureby, N. Alin, N. Wikström, S. Menon, N. Svanstedt, and L. Persson. Large eddy simulation of high-Reynolds-number wall bounded flows. *AIAA Journal*, 42(3):457–468, 2004.
- S. Galtier. Weak inertial-wave turbulence theory. *Physical Review E*, 68(1):015301, 2003.
- T. B. Gatski and C. G. Speziale. On explicit algebraic stress models for complex turbulent flows. *Journal of Fluid Mechanics*, 254:59–78, 1993.
- M. Germano. Turbulence: the filtering approach. *Journal of Fluid Mechanics*, 238:325–336, 1992.
- M. Germano, U. Piomelli, P. Moin, and W. H. Cabot. A dynamic subgrid-scale eddy viscosity model. *Physics of Fluids A: Fluid Dynamics*, 3(7):1760–1765, 1991.
- S. Ghosal and M. M. Rogers. A numerical study of self-similarity in a turbulent plane wake using large-eddy simulation. *Physics of Fluids*, 9(6):1729–1739, 1997.
- S. Ghosal, T. S. Lund, P. Moin, and K. Akselvoll. A dynamic localization model for large-eddy simulation of turbulent flows. *Journal of Fluid Mechanics*, 286:229–255, 1995.
- S. S. Girimaji. Fully explicit and self-consistent algebraic Reynolds stress model. *Theoretical and Computational Fluid Dynamics*, 8(6):387–402, 1996.
- F. S. Godeferd and F. Moisy. Structure and dynamics of rotating turbulence: a review of recent experimental and numerical results. *Applied Mechanics Reviews*, 67(3):030802–030802–13, 2015.
- H. P. Greenspan. *The theory of rotating fluids*. Cambridge University Press, 1968.

- S. Hickel, N. A. Adams, and J. A. Domaradzki. Letter to the editor: On the evolution of dissipation rate and resolved kinetic energy in ALDM simulations of the Taylor–Green flow. *Journal of Computational Physics*, 229(6):2422–2423, 2010.
- E. J. Hopfinger, F. K. Browand, and Y. Gagne. Turbulence and waves in a rotating tank. *Journal of Fluid Mechanics*, 125:505–534, 1982.
- K. Horiuti. Roles of non-aligned eigenvectors of strain-rate and subgrid-scale stress tensors in turbulence generation. *Journal of Fluid Mechanics*, 491:65–100, 2003.
- H. Kobayashi and Y. Shimomura. The performance of dynamic subgrid-scale models in the large eddy simulation of rotating homogeneous turbulence. *Physics of Fluids*, 13(8):2350–2360, 2001.
- R. Kristoffersen and H. I. Andersson. Direct simulations of low-Reynolds-number turbulent flow in a rotating channel. *Journal of Fluid Mechanics*, 256:163–197, 1993.
- B. E. Launder, G. J. Reece, and W. Rodi. Progress in the development of a Reynolds-stress turbulence closure. *Journal of Fluid Mechanics*, 68(03):537–566, 1975.
- D. K. Lilly. A proposed modification of the Germano subgrid-scale closure method. *Physics of Fluids A: Fluid Dynamics*, 4(3):633–635, 1992.
- H. Lu, C. J. Rutland, and L. M. Smith. A priori tests of one-equation LES modeling of rotating turbulence. *Journal of Turbulence*, (8):N37, 2007.
- N. Lu, R. E. Bensow, and G. Bark. LES of unsteady cavitation on the delft twisted foil. *Journal of Hydrodynamics, Ser. B*, 22(5):784–791, 2010.
- J. L. Lumley. Computational modeling of turbulent flows. *Advances in Applied Mechanics*, 18:123–176, 1979.
- J. L. Lumley and G. R. Newman. The return to isotropy of homogeneous turbulence. *Journal of Fluid Mechanics*, 82(1):161–178, 1977.
- E. Manoha, B. Troff, and P. Sagaut. Trailing-edge noise prediction using large-eddy simulation and acoustic analogy. *AIAA Journal*, 38(4):575–583, 2000.
- N. N. Mansour, J. Kim, and P. Moin. Reynolds-stress and dissipation-rate budgets in a turbulent channel flow. *Journal of Fluid Mechanics*, 194:15–44, 1988.
- L. Marstorp, G. Brethouwer, O. Grundestam, and A. V. Johansson. Explicit algebraic subgrid stress models with application to rotating channel flow. *Journal of Fluid Mechanics*, 639:403–432, 2009.
- A. D. McEwan. Angular momentum diffusion and the initiation of cyclones. *Nature*, 260(5547):126, 1976.
- M. Meyer, A. Devesa, S. Hickel, X. Y. Hu, and N. A. Adams. A conservative immersed interface method for large-eddy simulation of incompressible flows. *Journal of Computational Physics*, 229(18):6300–6317, 2010.

- M. Montecchia, G. Brethouwer, A. V. Johansson, and S. Wallin. Taking large-eddy simulation of wall-bounded flows to higher Reynolds numbers by use of anisotropy-resolving subgrid models. *Physical Review Fluids*, 2(3):034601, 2017.
- C. Morize, F. Moisy, and M. Rabaud. Decaying grid-generated turbulence in a rotating tank. *Physics of Fluids*, 17(9):095105, 2005.
- D. Naot, A. Shavit, and M. Wolfshtein. Interactions between components of the turbulent velocity correlation tensor due to pressure fluctuations. *Israel Journal of Technology*, 8(3): 259–269, 1970.
- A. Naso. Cyclone-anticyclone asymmetry and alignment statistics in homogeneous rotating turbulence. *Physics of Fluids*, 27(3):035108, 2015.
- M. Oberlack, W. Cabot, B. A. P. Reif, and T. Weller. Group analysis, direct numerical simulation and modelling of a turbulent channel flow with streamwise rotation. *Journal of Fluid Mechanics*, 562:383–403, 2006.
- U. Piomelli. High Reynolds number calculations using the dynamic subgrid-scale stress model. *Physics of Fluids A: Fluid Dynamics*, 5(6):1484–1490, 1993.
- S. B. Pope. A more general effective-viscosity hypothesis. *Journal of Fluid Mechanics*, 72 (02):331–340, 1975.
- S. B. Pope. *Turbulent flows*. Cambridge University Press, 2001.
- S. Remmler and S. Hickel. Direct and large eddy simulation of stratified turbulence. *International Journal of Heat and Fluid Flow*, 35:13–24, 2012.
- W. C. Reynolds. Computation of turbulent flows-state-of-the-art, 1970. 1972.
- W. Rodi. *The prediction of free turbulent boundary layers by use of a two-equation model of turbulence*. University of London, 1972.
- R. S. Rogallo. An ILLIAC program for the numerical simulation of homogeneous incompressible turbulence. *NASA STI/Recon Technical Report*, N78:13367, 1977.
- J. C. Rotta. Statistische theorie nichthomogener turbulenz. *Zeitschrift für Physik A Hadrons and Nuclei*, 129(6):547–572, 1951.
- P. Sagaut. *Large eddy simulation for incompressible flows: an introduction*. Springer Science & Business Media, 2006.
- P. Schuster. Stochasticity in processes. *Fundamentals and Applications to Chemistry and Biology*, Springer, 2016.
- T. Shih and J. L. Lumley. *Modeling of pressure correlation terms in Reynolds stress and scalar flux equations*. Sibley School of Mechanical and Equations Aerospace Engineering, Cornell University, 1985.
- Y. Shimomura. A family of dynamic subgrid-scale models consistent with asymptotic material frame indifference. *Journal of the Physical Society of Japan*, 68(8):2483–2486, 1999.

- C. C. Shir. A preliminary numerical study of atmospheric turbulent flows in the idealized planetary boundary layer. *Journal of the Atmospheric Sciences*, 30(7):1327–1339, 1973.
- T. Sjögren and A. V. Johansson. Development and calibration of algebraic nonlinear models for terms in the Reynolds stress transport equations. *Physics of Fluids*, 12(6):1554–1572, 2000.
- J. Smagorinsky. General circulation experiments with the primitive equations: I. the basic experiment. *Monthly Weather Review*, 91(3):99–164, 1963.
- L. M. Smith and F. Waleffe. Transfer of energy to two-dimensional large scales in forced, rotating three-dimensional turbulence. *Physics of Fluids*, 11(6):1608–1622, 1999.
- L. M. Smith, J. R. Chasnov, and F. Waleffe. Crossover from two-to three-dimensional turbulence. *Physical Review Letters*, 77(12):2467, 1996.
- P. R. Spalart. Direct simulation of a turbulent boundary layer up to $R_\theta = 1410$. *Journal of Fluid Mechanics*, 187:61–98, 1988.
- C. G. Speziale. Subgrid scale stress models for the large-eddy simulation of rotating turbulent flows. *Geophysical & Astrophysical Fluid Dynamics*, 33(1-4):199–222, 1985.
- C. G. Speziale, S. Sarkar, and T. B. Gatski. Modelling the pressure–strain correlation of turbulence: an invariant dynamical systems approach. *Journal of Fluid Mechanics*, 227: 245–272, 1991.
- C. G. Speziale, T. B. Gatski, and S. Sarkar. On testing models for the pressure–strain correlation of turbulence using direct simulations. *Physics of Fluids A: Fluid Dynamics*, 4 (12):2887–2899, 1992.
- P. J. Staplehurst, P. A. Davidson, and S. B. Dalziel. Structure formation in homogeneous freely decaying rotating turbulence. *Journal of Fluid Mechanics*, 598:81–105, 2008.
- B. Tao, J. Katz, and C. Meneveau. Geometry and scale relationships in high Reynolds number turbulence determined from three-dimensional holographic velocimetry. *Physics of Fluids*, 12(5):941–944, 2000.
- D. B. Taulbee. An improved algebraic Reynolds stress model and corresponding nonlinear stress model. *Physics of Fluids A: Fluid Dynamics*, 4(11):2555–2561, 1992.
- A. A. Townsend. The uniform distortion of homogeneous turbulence. *The Quarterly Journal of Mechanics and Applied Mathematics*, 7(1):104–127, 1954.
- S. C. Traugott. Influence of solid-body rotation on screen-produced turbulence. *NACA Technical Note 4135*, 1958.
- M. S. Uberoi. Equipartition of energy and local isotropy in turbulent flows. *Journal of Applied Physics*, 28(10):1165–1170, 1957.
- B. Vreman, B. Geurts, and H. Kuerten. On the formulation of the dynamic mixed subgrid-scale model. *Physics of Fluids*, 6(12):4057–4059, 1994.

- B. Vreman, B. Geurts, and H. Kuerten. Large-eddy simulation of the temporal mixing layer using the Clark model. *Theoretical and Computational Fluid Dynamics*, 8(4):309–324, 1996.
- S. Wallin. *Engineering turbulence modelling for CFD with focus on explicit algebraic Reynolds stress models*. Royal Institute of Technology, Department of Mechanics, 2000.
- S. Wallin and A. V. Johansson. An explicit algebraic Reynolds stress model for incompressible and compressible turbulent flows. *Journal of Fluid Mechanics*, 403:89–132, 2000.
- A. Yoshizawa and K. Horiuti. A statistically-derived subgrid-scale kinetic energy model for the large-eddy simulation of turbulent flows. *Journal of the Physical Society of Japan*, 54(8):2834–2839, 1985.
- Y. Zang, R. L. Street, and J. R. Koseff. A dynamic mixed subgrid-scale model and its application to turbulent recirculating flows. *Physics of Fluids A: Fluid Dynamics*, 5(12):3186–3196, 1993.
- O. Zeman. A note on the spectra and decay of rotating homogeneous turbulence. *Physics of Fluids*, 6(10):3221–3223, 1994.
- Y. Zhou. A phenomenological treatment of rotating turbulence. *Physics of Fluids*, 7(8):2092–2094, 1995.

Appendix A

Derivation of the transport equations for subgrid stress

Deriving the evolution equation for SGS stress can be done starting from the NS equations. In index notation, the incompressible NS equations without any body forces read,

$$\frac{\partial u_i}{\partial t} + \frac{\partial u_i u_k}{\partial x_k} = -\frac{1}{\rho} \frac{\partial p}{\partial x_i} + \nu \frac{\partial^2 u_i}{\partial x_k \partial x_k}. \quad (\text{A.1})$$

Multiplying with u_j gives,

$$u_j \frac{\partial u_i}{\partial t} + u_j \frac{\partial u_i u_k}{\partial x_k} = -\frac{u_j}{\rho} \frac{\partial p}{\partial x_i} + \nu u_j \frac{\partial^2 u_i}{\partial x_k \partial x_k}. \quad (\text{A.2})$$

Interchanging the indices i and j gives,

$$u_i \frac{\partial u_j}{\partial t} + u_i \frac{\partial u_j u_k}{\partial x_k} = -\frac{u_i}{\rho} \frac{\partial p}{\partial x_j} + \nu u_i \frac{\partial^2 u_j}{\partial x_k \partial x_k}. \quad (\text{A.3})$$

Adding Eq. (A.2) and (A.3),

$$\frac{\partial u_i u_j}{\partial t} + \frac{\partial u_i u_j u_k}{\partial x_k} = -\left(\frac{u_i}{\rho} \frac{\partial p}{\partial x_j} + \frac{u_j}{\rho} \frac{\partial p}{\partial x_i} \right) + \nu \frac{\partial^2 u_i u_j}{\partial x_k \partial x_k} - 2\nu \frac{\partial u_i}{\partial x_k} \frac{\partial u_j}{\partial x_k}. \quad (\text{A.4})$$

Filtering the above equation and rearranging the terms gives,

$$\frac{\partial \langle u_i u_j \rangle}{\partial t} + \frac{\partial \langle u_i u_j u_k \rangle}{\partial x_k} + \left(\left\langle \frac{u_i}{\rho} \frac{\partial p}{\partial x_j} \right\rangle + \left\langle \frac{u_j}{\rho} \frac{\partial p}{\partial x_i} \right\rangle \right) - \nu \frac{\partial^2 \langle u_i u_j \rangle}{\partial x_k \partial x_k} = -2\nu \left\langle \frac{\partial u_i}{\partial x_k} \frac{\partial u_j}{\partial x_k} \right\rangle, \quad (\text{A.5})$$

$$\begin{aligned} \frac{\partial \langle u_i u_j \rangle}{\partial t} + \frac{\partial \langle u_i u_j u_k \rangle}{\partial x_k} + \left(\frac{1}{\rho} \frac{\partial \langle p u_i \rangle}{\partial x_j} + \frac{1}{\rho} \frac{\partial \langle p u_j \rangle}{\partial x_i} \right) - \nu \frac{\partial^2 \langle u_i u_j \rangle}{\partial x_k \partial x_k} = \\ \left(\left\langle \frac{p}{\rho} \frac{\partial u_i}{\partial x_j} \right\rangle + \left\langle \frac{p}{\rho} \frac{\partial u_j}{\partial x_i} \right\rangle \right) - 2\nu \left\langle \frac{\partial u_i}{\partial x_k} \frac{\partial u_j}{\partial x_k} \right\rangle. \end{aligned} \quad (\text{A.6})$$

Grouping the transport terms on the LHS results in

$$\begin{aligned} \frac{\partial \langle u_i u_j \rangle}{\partial t} + \frac{\partial}{\partial x_k} \left(\langle u_i u_j u_k \rangle + \frac{1}{\rho} \langle p u_i \rangle \delta_{jk} + \frac{1}{\rho} \langle p u_j \rangle \delta_{ik} - \nu \frac{\partial \langle u_i u_j \rangle}{\partial x_k} \right) = \\ \left(\left\langle \frac{p}{\rho} \frac{\partial u_i}{\partial x_j} \right\rangle + \left\langle \frac{p}{\rho} \frac{\partial u_j}{\partial x_i} \right\rangle \right) - 2\nu \left\langle \frac{\partial u_i}{\partial x_k} \frac{\partial u_j}{\partial x_k} \right\rangle. \end{aligned} \quad (\text{A.7})$$

We shall now repeat a similar procedure starting with filtered NS equations,

$$\begin{aligned} \frac{\partial \langle u_i \rangle}{\partial t} + \frac{\partial \langle u_i u_k \rangle}{\partial x_k} &= -\frac{1}{\rho} \frac{\partial \langle p \rangle}{\partial x_i} + \nu \frac{\partial^2 \langle u_i \rangle}{\partial x_k \partial x_k}, \\ \frac{\partial \langle u_i \rangle}{\partial t} + \frac{\partial \langle u_i \rangle \langle u_k \rangle}{\partial x_k} &= -\frac{1}{\rho} \frac{\partial \langle p \rangle}{\partial x_i} + \nu \frac{\partial^2 \langle u_i \rangle}{\partial x_k \partial x_k} - \frac{\partial \tau_{ik}}{\partial x_k}. \end{aligned}$$

where $\tau_{ik} = \langle u_i u_k \rangle - \langle u_i \rangle \langle u_k \rangle$.

Multiplying the above equation with $\langle u_j \rangle$,

$$\langle u_j \rangle \frac{\partial \langle u_i \rangle}{\partial t} + \langle u_j \rangle \frac{\partial \langle u_i \rangle \langle u_k \rangle}{\partial x_k} = -\frac{\langle u_j \rangle}{\rho} \frac{\partial \langle p \rangle}{\partial x_i} + \nu \langle u_j \rangle \frac{\partial^2 \langle u_i \rangle}{\partial x_k \partial x_k} - \langle u_j \rangle \frac{\partial \tau_{ik}}{\partial x_k}. \quad (\text{A.8})$$

Interchanging the indices i and j in Eq. (A.8) and summing it up with Eq. (A.8),

$$\begin{aligned} \frac{\partial \langle u_i \rangle \langle u_j \rangle}{\partial t} + \frac{\partial \langle u_i \rangle \langle u_j \rangle \langle u_k \rangle}{\partial x_k} + \left(\frac{\langle u_i \rangle}{\rho} \frac{\partial \langle p \rangle}{\partial x_j} + \frac{\langle u_j \rangle}{\rho} \frac{\partial \langle p \rangle}{\partial x_i} \right) - \nu \frac{\partial^2 \langle u_i \rangle \langle u_j \rangle}{\partial x_k \partial x_k} = \\ -2\nu \frac{\partial \langle u_i \rangle}{\partial x_k} \frac{\partial \langle u_j \rangle}{\partial x_k} - \langle u_i \rangle \frac{\partial \tau_{jk}}{\partial x_k} - \langle u_j \rangle \frac{\partial \tau_{ik}}{\partial x_k}. \end{aligned} \quad (\text{A.9})$$

The above equation can be rewritten as,

$$\begin{aligned} \frac{\partial \langle u_i \rangle \langle u_j \rangle}{\partial t} + \frac{\partial}{\partial x_k} \left(\langle u_i \rangle \langle u_j \rangle \langle u_k \rangle + \frac{\langle u_i \rangle \langle p \rangle}{\rho} \delta_{jk} + \frac{\langle u_j \rangle \langle p \rangle}{\rho} \delta_{ik} - \nu \frac{\partial \langle u_i \rangle \langle u_j \rangle}{\partial x_k} \right) = \\ \left(\frac{\langle p \rangle}{\rho} \frac{\partial \langle u_i \rangle}{\partial x_j} + \frac{\langle p \rangle}{\rho} \frac{\partial \langle u_j \rangle}{\partial x_i} \right) - 2\nu \frac{\partial \langle u_i \rangle}{\partial x_k} \frac{\partial \langle u_j \rangle}{\partial x_k} - \langle u_i \rangle \frac{\partial \tau_{jk}}{\partial x_k} - \langle u_j \rangle \frac{\partial \tau_{ik}}{\partial x_k}, \\ \frac{\partial \langle u_i \rangle \langle u_j \rangle}{\partial t} + \frac{\partial}{\partial x_k} \left(\langle u_i \rangle \langle u_j \rangle \langle u_k \rangle + \langle u_i \rangle \tau_{jk} + \langle u_j \rangle \tau_{ik} + \frac{\langle u_i \rangle \langle p \rangle}{\rho} \delta_{jk} + \frac{\langle u_j \rangle \langle p \rangle}{\rho} \delta_{ik} \right. \\ \left. - \nu \frac{\partial \langle u_i \rangle \langle u_j \rangle}{\partial x_k} \right) = \\ \left(\frac{\langle p \rangle}{\rho} \frac{\partial \langle u_i \rangle}{\partial x_j} + \frac{\langle p \rangle}{\rho} \frac{\partial \langle u_j \rangle}{\partial x_i} \right) - 2\nu \frac{\partial \langle u_i \rangle}{\partial x_k} \frac{\partial \langle u_j \rangle}{\partial x_k} + \tau_{jk} \frac{\partial \langle u_i \rangle}{\partial x_k} + \tau_{ik} \frac{\partial \langle u_j \rangle}{\partial x_k}. \end{aligned} \quad (\text{A.10})$$

Subtracting Eq. (A.10) from (A.7),

$$\begin{aligned}
& \frac{\partial \tau_{ij}}{\partial t} + \frac{\partial}{\partial x_k} \left(\langle u_i u_j u_k \rangle - \langle u_i \rangle \langle u_j \rangle \langle u_k \rangle - \langle u_i \rangle \tau_{jk} - \langle u_j \rangle \tau_{ik} \right. \\
& \quad \left. + \chi \left(u_i, \frac{p}{\rho} \right) \delta_{jk} + \chi \left(u_j, \frac{p}{\rho} \right) \delta_{ik} - \nu \frac{\partial \chi(u_i, u_j)}{\partial x_k} \right) = \\
& \left(\chi \left(\frac{p}{\rho}, \frac{\partial u_i}{\partial x_j} \right) + \chi \left(\frac{p}{\rho}, \frac{\partial u_j}{\partial x_i} \right) \right) - 2\nu \chi \left(\frac{\partial u_i}{\partial x_k}, \frac{\partial u_j}{\partial x_k} \right) - \tau_{jk} \frac{\partial \langle u_i \rangle}{\partial x_k} - \tau_{ik} \frac{\partial \langle u_j \rangle}{\partial x_k}, \\
& \frac{\partial \tau_{ij}}{\partial t} + \langle u_k \rangle \frac{\partial \tau_{ij}}{\partial x_k} + \frac{\partial}{\partial x_k} \left(\chi(u_i, u_j, u_k) + \chi \left(u_i, \frac{p}{\rho} \right) \delta_{jk} + \chi \left(u_j, \frac{p}{\rho} \right) \delta_{ik} - \nu \frac{\partial \chi(u_i, u_j)}{\partial x_k} \right) = \\
& \quad - \tau_{jk} \frac{\partial \langle u_i \rangle}{\partial x_k} - \tau_{ik} \frac{\partial \langle u_j \rangle}{\partial x_k} + \left(\chi \left(\frac{p}{\rho}, \frac{\partial u_i}{\partial x_j} \right) + \chi \left(\frac{p}{\rho}, \frac{\partial u_j}{\partial x_i} \right) \right) - 2\nu \chi \left(\frac{\partial u_i}{\partial x_k}, \frac{\partial u_j}{\partial x_k} \right), \\
& \tag{A.11}
\end{aligned}$$

where $\chi(\cdot)$ are the central moments defined in Eq. (2.5) and (2.6). Equation (A.11) can be rewritten in terms of material derivative and generalised central moments as,

$$\begin{aligned}
& \frac{\langle D \rangle \chi(u_i, u_j)}{Dt} + \frac{\partial}{\partial x_k} \left[\chi(u_i, u_j, u_k) + \frac{1}{\rho} \chi(p, u_j) \delta_{ik} + \frac{1}{\rho} \chi(p, u_i) \delta_{jk} - \nu \frac{\partial \chi(u_i, u_j)}{\partial x_k} \right] = \\
& - \chi(u_j, u_k) \frac{\partial \langle u_i \rangle}{\partial x_k} - \chi(u_i, u_k) \frac{\partial \langle u_j \rangle}{\partial x_k} + \chi \left(\frac{p}{\rho}, \frac{\partial u_j}{\partial x_i} \right) + \chi \left(\frac{p}{\rho}, \frac{\partial u_i}{\partial x_j} \right) - 2\nu \chi \left(\frac{\partial u_i}{\partial x_k}, \frac{\partial u_j}{\partial x_k} \right).
\end{aligned}$$

Appendix B

Derivation of the explicit algebraic stress model by Marstorp et al.

The EASSM of Marstorp et al. (2009) starts with the simplification that $\mathcal{P} = \epsilon$ that reduces the simplified equation for SGS stresses in Eq. (2.16) to

$$\mathcal{P}_{ij} + \Pi_{ij} - \epsilon_{ij} = 0. \quad (\text{B.1})$$

The expression for the production term can be written as,

$$\begin{aligned} \mathcal{P}_{ij} &= -\tau_{ik} \frac{\partial \langle u_j \rangle}{\partial x_k} - \tau_{jk} \frac{\partial \langle u_i \rangle}{\partial x_k} \\ &= -\tau_{ik} \left(\langle S_{jk} \rangle + \langle \Omega_{jk} \rangle \right) - \tau_{jk} \left(\langle S_{ik} \rangle + \langle \Omega_{ik} \rangle \right) \\ &= -\left(\tau_{ik} \langle S_{kj} \rangle + \langle S_{ik} \rangle \tau_{kj} \right) - \left(-\tau_{ik} \langle \Omega_{kj} \rangle + \langle \Omega_{ik} \rangle \tau_{kj} \right) \\ &= \left(-k_{sgs} a_{ik} \langle S_{kj} \rangle - k_{sgs} \langle S_{ik} \rangle a_{kj} - \frac{2}{3} \delta_{ik} \langle S_{jk} \rangle k_{sgs} - \frac{2}{3} \delta_{jk} \langle S_{ik} \rangle k_{sgs} \right) \\ &\quad + \left(k_{sgs} a_{ik} \langle \Omega_{jk} \rangle - k_{sgs} \langle \Omega_{ik} \rangle a_{kj} - \frac{2}{3} \delta_{ik} \langle \Omega_{jk} \rangle k_{sgs} - \frac{2}{3} \delta_{jk} \langle \Omega_{ik} \rangle k_{sgs} \right) \\ \mathcal{P}_{ij} &= k_{sgs} \left[\frac{-4}{3} \langle S_{ij} \rangle - \left(a_{ik} \langle S_{kj} \rangle + \langle S_{ik} \rangle a_{kj} \right) + \left(a_{ik} \langle \Omega_{kj} \rangle - \langle \Omega_{ik} \rangle a_{kj} \right) \right] \end{aligned} \quad (\text{B.2})$$

A modified LRR-QI model and an isotropic model were used for the pressure-strain and the dissipation terms respectively. Accordingly, substituting the expressions for the terms in Eq. (B.1) results in,

$$\begin{array}{l}
\text{Production tensor} \\
\text{Modified LRR model} \\
\text{Isotropic dissipation model}
\end{array}
\left\{ \begin{array}{l}
k_{sgs} \left[\frac{-4}{3} \langle S_{ij} \rangle - \left(a_{ik} \langle S_{kj} \rangle + \langle S_{ik} \rangle a_{kj} \right) \right. \\
\left. + \left(a_{ik} \langle \Omega_{kj} \rangle - \langle \Omega_{ik} \rangle a_{kj} \right) \right] \\
-C_1 \epsilon a_{ij} \\
+k_{sgs} \left[\frac{3}{5} \langle S_{ij} \rangle \right. \\
\left. + \frac{9C_2+6}{11} \left(a_{ik} \langle S_{kj} \rangle + \langle S_{ik} \rangle a_{kj} - \frac{2}{3} a_{mn} \langle S_{mn} \rangle \delta_{ij} \right) \right. \\
\left. + \frac{7C_2-10}{11} \left(a_{ik} \langle \Omega_{kj} \rangle - \langle \Omega_{ik} \rangle a_{kj} \right) \right] \\
-\frac{2}{3} \epsilon \delta_{ij}
\end{array} \right. = 0.$$

Grouping the terms together and substituting the value of C_2 as $\frac{5}{9}$, and dividing the whole expression by ϵ ,

$$\begin{aligned}
C_1 a_{ij} &= \frac{k_{sgs}}{\epsilon} \left[\frac{-11}{15} \langle S_{ij} \rangle + \frac{9C_2 - 5}{11} \left(a_{ik} \langle S_{kj} \rangle + \langle S_{ik} \rangle a_{kj} \right) - \frac{18C_2 + 12}{33} a_{mn} \langle S_{mn} \rangle \delta_{ij} \right. \\
&\quad \left. + \frac{7C_2 + 1}{11} \left(a_{ik} \langle \Omega_{kj} \rangle - \langle \Omega_{ik} \rangle a_{kj} \right) \right] - \frac{2}{3} \delta_{ij} \\
&= \tau^* \left[\frac{-11}{15} \langle S_{ij} \rangle + \frac{4}{9} \left(a_{ik} \langle \Omega_{kj} \rangle - \langle \Omega_{ik} \rangle a_{kj} \right) \right] + \frac{2}{3} \frac{\mathcal{P}}{\epsilon} \delta_{ij} - \frac{2}{3} \delta_{ij}.
\end{aligned}$$

Since the an assumption of perfect equilibrium was made, $\mathcal{P} = \epsilon$. Therefore,

$$C_1 a_{ij} = \tau^* \left[\frac{-11}{15} \langle S_{ij} \rangle + \frac{4}{9} \left(a_{ik} \langle \Omega_{kj} \rangle - \langle \Omega_{ik} \rangle a_{kj} \right) \right] \quad (\text{B.3})$$

Equation (B.3), although linear, is implicit in terms of \mathbf{a} and in order to find the explicit form in terms of tensorial bases as formulated by Pope (1975). The general form of this solution is shown in Eq. (2.24) and consists of ten bases tensors. To simplify the mathematical complexity, Pope (1975) reduced this for statistically two dimensional flows where three tensors are constructed (in matrix form):

$$\mathbf{T}^0 = \frac{1}{3} \mathbf{I}_3 - \frac{1}{2} \mathbf{I}_2, \quad \mathbf{T}^1 = \tau^* \mathbf{S}, \quad \text{and} \quad \mathbf{T}^2 = \tau^{*2} (\mathbf{S} \mathbf{\Omega} - \mathbf{\Omega} \mathbf{S}). \quad (\text{B.4})$$

\mathbf{S} and $\mathbf{\Omega}$ in the above expression represent the resolved strain rate and rotation rate tensors in matrix form, and \mathbf{I}_2 and \mathbf{I}_3 are given by the following relation.

$$\mathbf{I}_3 = \delta_{ij}^{(3)} \begin{cases} = 1, & i = j \\ = 0, & i \neq j \end{cases}$$

$$\mathbf{I}_2 = \delta_{ij}^{(2)} \begin{cases} = 1, & i = j \neq 3 \\ = 0, & i \neq j \\ = 0, & i = j = 3 \end{cases}$$

In the momentum equation, the subgrid stress tensor appears with a divergence operator. Taking a look at the tensor $\mathbf{T}^{(0)}$, it is clear due to the presence of δ_{ij} , the corresponding term appears with a gradient operator. Hence it can be added to the pressure term and does not alter the velocity fields. So for the explicit formulation, Marstorp et al. (2009) remove this tensor and only used $\mathbf{T}^{(1)}$ and $\mathbf{T}^{(2)}$. Substituting these bases tensors in Eq. (B.3),

$$C_1 \sum_{n=1}^2 G^{(n)} T_{ij}^{(n)} = \tau^* \left(-\frac{11}{15} \mathbf{S} + \frac{4}{9} \left(G^{(1)} \mathbf{T}^{(1)} \mathbf{\Omega} - \mathbf{\Omega} G^{(1)} \mathbf{T}^{(1)} + G^{(2)} \mathbf{T}^{(2)} \mathbf{\Omega} - \mathbf{\Omega} G^{(2)} \mathbf{T}^{(2)} \right) \right) \quad (\text{B.5})$$

Simplifying the above expression term by term, tensor $\mathbf{T}^{(1)}$ (2nd and 3rd term of R.H.S) :

$$\begin{aligned} \mathbf{T}^{(1)} \mathbf{\Omega} - \mathbf{\Omega} \mathbf{T}^{(1)} &= \tau^* (\mathbf{S} \mathbf{\Omega} - \mathbf{\Omega} \mathbf{S}), \\ &= \frac{1}{\tau^*} \mathbf{T}^{(2)}. \end{aligned} \quad (\text{B.6})$$

Tensor $\mathbf{T}^{(2)}$ (4th and 5th term of R.H.S) :

$$\mathbf{T}^{(2)} \mathbf{\Omega} - \mathbf{\Omega} \mathbf{T}^{(2)} = \tau^{*2} (\mathbf{S} \mathbf{\Omega}^2 - \mathbf{\Omega} \mathbf{S} \mathbf{\Omega} - \mathbf{\Omega} \mathbf{S} \mathbf{\Omega} + \mathbf{\Omega}^2 \mathbf{S}). \quad (\text{B.7})$$

The higher order tensors in Eq. (B.7) can be reduced using Caley-Hamilton theorem as shown in Pope (1975) using the identities,

$$\mathbf{c}^2 = \mathbf{c} \{ \mathbf{c} \} - \frac{1}{2} \mathbf{I}_2 (\{ \mathbf{c} \}^2 - \{ \mathbf{c}^2 \}) \quad (\text{B.8})$$

$$\mathbf{bab} = \frac{1}{2} (\mathbf{a} - \mathbf{I}_2 \{ \mathbf{a} \}) (\{ \mathbf{b} \}^2 - \{ \mathbf{b}^2 \}) + \mathbf{b} \{ \mathbf{ab} \} \quad (\text{B.9})$$

Here, c , a and b are two dimensional second order tensors, and $\{.\}$ represents the trace. By using Eqs. (B.8) and (B.9),

$$\boldsymbol{\Omega}^2 = \frac{1}{2} \mathbf{I}_2 \{\boldsymbol{\Omega}^2\} \quad (\text{B.10})$$

$$\boldsymbol{\Omega} \mathbf{S} \boldsymbol{\Omega} = -\frac{\mathbf{S}}{2} \{\boldsymbol{\Omega}^2\} \quad (\text{B.11})$$

Substituting Eqs. (B.10) and (B.11) into Eq. (B.7), we obtain

$$\begin{aligned} \mathbf{T}^{(2)} \boldsymbol{\Omega} - \boldsymbol{\Omega} \mathbf{T}^{(2)} &= \tau^{*2} \left(\frac{\mathbf{S}}{2} \{\boldsymbol{\Omega}^2\} + \mathbf{S} \{\boldsymbol{\Omega}^2\} + \frac{\mathbf{S}}{2} \{\boldsymbol{\Omega}^2\} \right) \\ &= 2\tau^{*2} \mathbf{S} \{\boldsymbol{\Omega}^2\} \\ &= 2\tau^* \{\boldsymbol{\Omega}^2\} \mathbf{T}^{(1)} \end{aligned} \quad (\text{B.12})$$

Substituting Eqs. (B.6) and (B.12) into Eq. (B.5),

$$C_1 \sum_{n=1}^2 G^{(n)} \mathbf{T}^{(n)} = \left(-\frac{11}{15} + \frac{4}{9} G^{(2)} (2\tau^{*2} \{\boldsymbol{\Omega}^2\}) \right) \mathbf{T}^{(1)} + \left(\frac{4}{9} G^{(1)} \right) \mathbf{T}^{(2)} \quad (\text{B.13})$$

$$(\text{B.14})$$

Equating the coefficients of the bases tensors,

$$\begin{aligned} C_1 G^{(2)} &= \frac{4}{9} G^{(1)} \\ G^{(2)} &= \frac{4}{9C_1} G^{(1)} \end{aligned} \quad (\text{B.15})$$

$$\begin{aligned} C_1 G^{(1)} &= -\frac{11}{15} + \frac{4}{9} G^{(2)} (2\tau^{*2} \{\boldsymbol{\Omega}^2\}) \\ C_1 G^{(1)} - \frac{4}{9} G^{(2)} (2\tau^{*2} \{\boldsymbol{\Omega}^2\}) &= -\frac{11}{15} \end{aligned} \quad (\text{B.16})$$

Substituting Eq. (B.15) into Eq. (B.16),

$$\begin{aligned} C_1 G^{(1)} - \frac{16}{81C_1} G^{(1)} (2\tau^{*2} \{\boldsymbol{\Omega}^2\}) &= -\frac{11}{15} \\ \frac{4}{9} G^{(1)} \left(\frac{9}{4} C_1 - \frac{2\tau^{*2} \{\boldsymbol{\Omega}^2\}}{\frac{9}{4} C_1} \right) &= -\frac{11}{15} \\ G^{(1)} &= -\frac{33}{20} \left(\frac{1}{\frac{9}{4} C_1 - \frac{2\tau^{*2} \{\boldsymbol{\Omega}^2\}}{\frac{9}{4} C_1}} \right) \\ &= -\frac{33}{20} \frac{\frac{9}{4} C_1}{\left(\frac{9}{4} C_1 \right)^2 - 2\tau^{*2} \{\boldsymbol{\Omega}^2\}}, \quad \text{and} \end{aligned} \quad (\text{B.17})$$

$$G^{(2)} = -\frac{33}{20} \frac{1}{\left(\frac{9}{4} C_1 \right)^2 - 2\tau^{*2} \{\boldsymbol{\Omega}^2\}}. \quad (\text{B.18})$$

Thus, τ_{ij} can be given by,

$$\tau_{ij} = k_{sgs} \left(\frac{2}{3} \delta_{ij} + G^{(1)} \tau^* \langle S_{ij} \rangle + G^{(2)} \tau^{*2} (\langle S_{ik} \rangle \langle \Omega_{kj} \rangle - \langle \Omega_{ik} \rangle \langle S_{kj} \rangle) \right) \quad (\text{B.19})$$

To summarise the methodology behind deriving the formulation in Eq. (B.19),

- Simplify the L.H.S in Eq. (2.16) by using the identity $\mathcal{P}/\epsilon = 1$.
- Substitute linear LRR-QI model for pressure-strain term and isotropic model for dissipation.
- Simplify the expression by substituting the constant in LRR-IP model, $C_2 = 5/9$.
- At this point, we arrive at Eq. (B.3). Substitute the first two tensorial bases in Tab. 2.2 to get the Eq. (B.5).
- Use Cayley-Hamilton theorem to simplify the higher order tensors. (Eq. (B.10) and (B.11)).
- Equate the coefficients of the tensorial bases and solve the resulting system to find expressions for the coefficients.

The expressions for additions SGS quantities k_{sgs} and τ^* were given in Tab. 2.3. The values of the constants in the expression for k_{sgs} and τ^* are as follows,

$$C_S = 0.10, \quad C_K = 1.50, \quad c_k = 0.40, \quad c_3 = 2.20, \quad \text{and} \quad c'_3 = 2.40.$$

The constant C_1 in the expression for tensor coefficients (Eq. (B.17), and (B.18)) is given in Tab. B.1, where $c'_d = 4.20$. The expression for Φ reads,

$$\Phi = \frac{II_\Omega}{2II_S} \frac{(c'_3 1.5 C_K^{1.5})^2}{c'_{nd}}, \quad (\text{B.20})$$

where, $c'_{nd} = 0.60$ and $c''_3 = 0.40$.

	Dynamic version	Non-dynamic version
C_1	$c'_d \sqrt{c'_3} \frac{c^{1.25}}{(2C_S)^{2.5}}$	$-\Phi + \sqrt{\Phi^2 + c'_{nd} \frac{33}{40} \frac{c_k^2}{(2C_S)^2}}$

Table B.1: Expressions for C_1 in the model of Marstorp et al. (2009).

Implementation of models into INCA

The dynamic, non-dynamic, and non-equilibrium EASSMs are implemented into INCA discretised on staggered meshes. The interpolations necessary in order to compute non-linear terms are not so straight-forward. Furthermore, the type of interpolation affects the final solution noticeably. The different ways of computing non-linear terms was found by trial and error. The procedure adopted for the current implementation of the models is provided here.

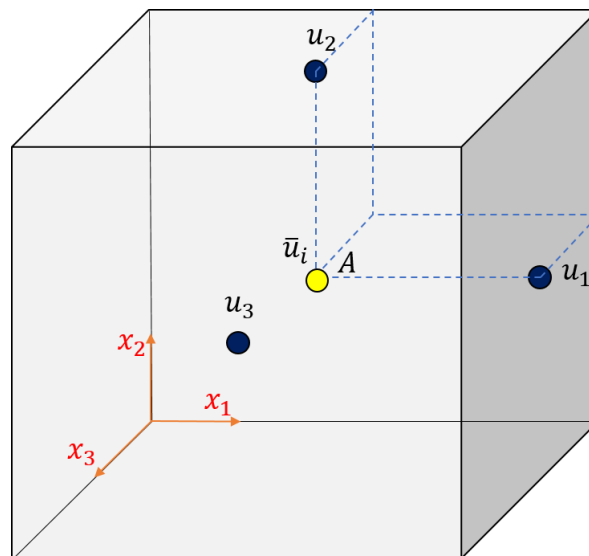


Figure C.1: The configuration of a staggered mesh showing the discretisation of actual velocity along with the interpolated velocity.

The velocity components are discretised in a staggered mesh as shown in Fig. C.1. For the sake of convenience we omit the convolution operation here. All velocities discussed here are to be interpreted as the filtered velocities $\langle u_i \rangle$. The pressure is discretised at centre of the cell (node A). However, since the closures implemented do not contain any terms dependent

of pressure, it is omitted in the representation (Fig. C.1). The velocities in the staggered configuration u_i are also interpolated to the center of the (collocated) cell at node A. The interpolated velocities are located at node A in Fig. C.1 are termed as \bar{u}_i . It must be pointed out that all interpolations performed here are linear.

All spatial derivatives are computed using a second order central difference scheme. It is therefore desired that we evaluate the SGS stress tensor elements as shown in Fig. C.2. ϕ_{ij} represents a generalised tensor whose location is decided based on the values of indices i and j . Since we deal with algebraic closures, we also require that $\langle S_{ij} \rangle, \langle \Omega_{ij} \rangle$ to be computed at the locations as shown in Fig. C.2.

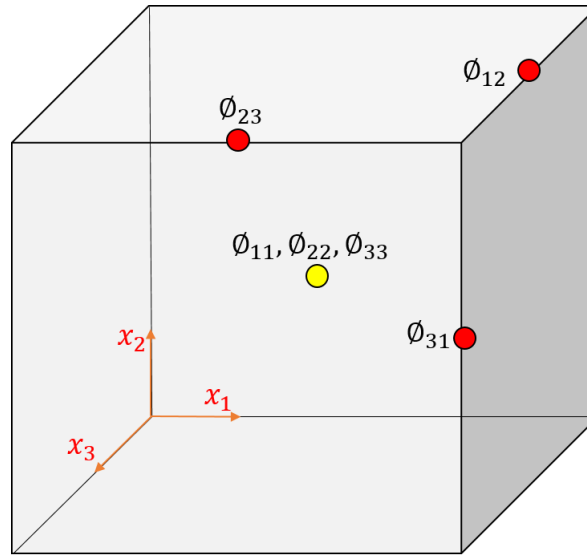


Figure C.2: Location of the tensor elements on the computational mesh.

In the formulation of an EASSM, we have two tensors $T_{ij}^{(1)}$ and $T_{ij}^{(2)}$, and two coefficients $G^{(1)}$ and $G^{(2)}$. In addition, we also have k_{sgs} , τ^* and η (in case of the non-equilibrium EASSM). Apart from the two tensors, all other quantities are termed scalars and are computed at the cell centres, i.e. node A in Fig. C.1. Recall the expression for the modelled SGS stress tensor which reads,

$$\tau_{ij} = k_{sgs} \left[G^{(1)} \tau^* \langle S_{ij} \rangle + G^{(2)} \tau^{*2} \left(\langle S_{ik} \rangle \langle \Omega_{kj} \rangle - \langle \Omega_{ik} \rangle \langle S_{kj} \rangle \right) + \frac{2}{3} \delta_{ij} \right], \quad (\text{C.1})$$

C.1 Computing scalars

From the discussion thus far, we say that all the tensors in the formulation are evaluated at the location of ϕ_{ij} shown in Fig. C.2 while all scalars are located at the central node A in Fig. C.1. It must be noticed that also $G^{(1)}$, and $G^{(2)}$ are functions of the invariant of $\langle \Omega_{ij} \rangle$ for which, not all the components are computed at node A. This is also the case for k_{sgs} and

τ^* which are functions of the $\langle S_{ij} \rangle$ in the dynamic and non-dynamic versions. We can also notice from Fig. C.2 that only the off-diagonal tensor components are not evaluated at A. Therefore in order to obtain the values of $\langle S_{ij} \rangle$ and $\langle \Omega_{ij} \rangle$ for $i \neq j$ at A, we compute these components from the interpolated velocities \bar{u}_i (using central difference scheme). By doing this, we shall obtain all components of $\langle S_{ij} \rangle$ and $\langle \Omega_{ij} \rangle$ required for computing the different scalars at the cell centre location-A.

Once we compute the scalars at node A, in evaluation Eq. (C.1), we require a product between the basis tensors and the scalar coefficients. In Fig. C.2, it can be seen that the off-diagonal tensor components are discretised on the red nodes. Therefore in order to compute the scalar-tensor product, the scalars which are at the (yellow) cell centre node will have to be interpolated onto the red nodes. In order to perform this, we simply construct a 2D cell that runs through the red and the yellow nodes involved in the product. The yellow nodes of the neighbouring cells form the corners while the red node is placed at the centre of the 2D cell. Using the four (yellow) nodes (current cell plus three neighbouring cells), we then interpolate the scalar onto the tensor node.

C.2 Computing the non-linear term: the second tensor

The first (tensorial) term in Eq. (C.1) is $\langle S_{ij} \rangle$. Since this is computed at the same location as τ_{ij} , it does not pose any problems and is evaluated in a straight-forward way. On the other hand, the second term involves a non-linearity and a summation over the repeated index k . This complicates the implementation as it requires interpolation, especially in the case of off-diagonal entries of τ_{ij} . We shall demonstrate the procedure for (a diagonal element) τ_{11} and (an off-diagonal element) τ_{12} . The extension to other elements of the tensor can be done intuitively.

C.2.1 Diagonal component

For $(i, j) = (1, 1)$, omitting the scalars and the first tensor in the Eq. (C.1), we obtain,

$$\begin{aligned} \tau_{11} &\sim \langle S_{1k} \rangle \langle \Omega_{k1} \rangle - \langle \Omega_{1k} \rangle \langle S_{k1} \rangle \\ &= 2 \langle S_{1k} \rangle \langle \Omega_{k1} \rangle, \end{aligned} \quad (\text{C.2})$$

where the RHS of Eq. (C.2) is summed over $k = 1, 2, \text{ and } 3$. When $k = 1$, $\langle \Omega_{11} \rangle = 0$. When $k = 2$,

$$\begin{aligned} RHS_{k=2} &= 2 \langle S_{12} \rangle \langle \Omega_{21} \rangle \\ &= -2 \langle S_{12} \rangle \langle \Omega_{12} \rangle. \end{aligned} \quad (\text{C.3})$$

Figure C.3 shows the points at which $\langle S_{ij} \rangle$ and $\langle \Omega_{ij} \rangle$ are evaluated for the current cell (shown in red) and for the neighbouring cells (shown in light blue). Since we need the value of Eq.

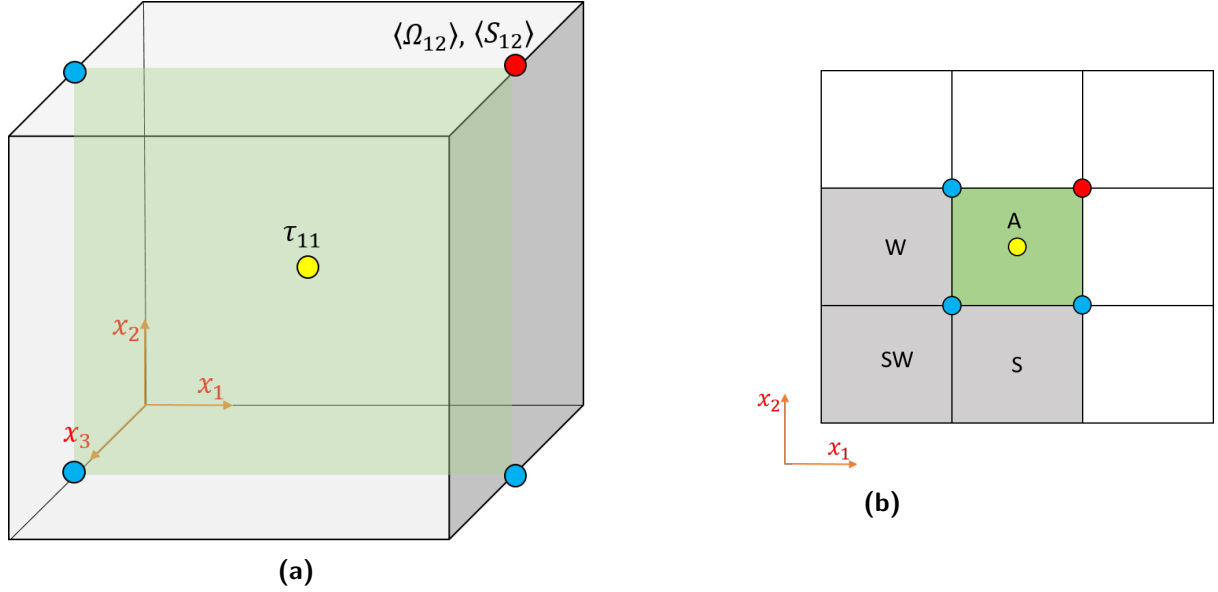


Figure C.3: (a) Discretisation of the tensor elements in the non-linear term required for τ_{11} when the index $k = 2$ and (b) the corresponding nodes of the current and the neighbouring cells on the shaded x_1x_2 - plane shown in (a). The cells to the west, south-west and south are shaded in grey.

(C.3) at the node A, where τ_{11} is evaluated (shown in yellow in Fig. C.3), the non-linear product is first computed at the red and blue nodes (corresponding to the cell to the west, south, and south-west of the current cell) and then interpolated to the yellow node.

Similarly, for $k = 3$, we obtain,

$$\begin{aligned} RHS_{k=3} &= 2\langle S_{13} \rangle \langle \Omega_{31} \rangle \\ &= -2\langle S_{31} \rangle \langle \Omega_{31} \rangle. \end{aligned} \quad (\text{C.4})$$

We follow a similar procedure in that first, Eq. (C.4) is evaluated at each node and then interpolated from the points on the x_1x_3 -plane as shown in Fig. C.4.

Finally, once the entire RHS of Eq. (C.2) is computed at A, it is now at the same location as τ_{11} . We follow the same approach to evaluate τ_{22} and τ_{33} as well, i.e. first compute the non-linear product and interpolate the non-linear terms to the cell centre.

C.2.2 Off-diagonal component

The evaluation of the non-linear term for the off-diagonal entries is more strenuous than for diagonal entries. This is because, for the diagonal elements, the tensors involved in the non-linear product have the same indices $-\langle S_{ik} \rangle \langle \Omega_{ik} \rangle$ and therefore computing product (before interpolating to node A) is direct. However, for the off-diagonal elements we will demonstrate

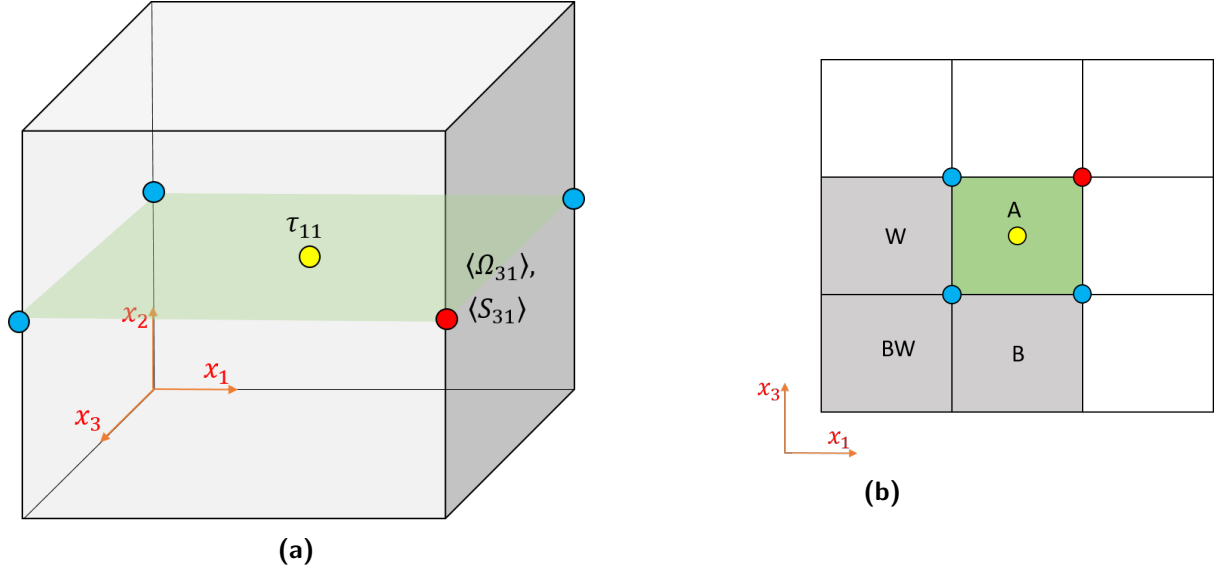


Figure C.4: (a) Discretisation of the tensor elements in the non-linear term required for τ_{11} when the index $k = 3$ and (b) the corresponding nodes of the current and the neighbouring cells on the shaded x_1x_3 - plane shown in (a). The cells to the west, behind-west and behind are shaded in grey.

that this is not the case. For this purpose, we examine the evaluation of τ_{12} . Ignoring the scalars and the first linear tensor in Eq. (C.1), we obtain,

$$\tau_{12} \sim \langle S_{1k} \rangle \langle \Omega_{k2} \rangle - \langle \Omega_{1k} \rangle \langle S_{k2} \rangle. \quad (\text{C.5})$$

For $k = 1$, we obtain

$$\begin{aligned} RHS_{k=1} &= \langle S_{11} \rangle \langle \Omega_{12} \rangle - \langle \Omega_{11} \rangle \langle S_{12} \rangle. \\ &= \langle S_{11} \rangle \langle \Omega_{12} \rangle \end{aligned} \quad (\text{C.6})$$

Figure C.5 shows the discretisation of the tensor elements required in Eq. (C.6). Since τ_{12} and $\langle \Omega_{12} \rangle$ are at the same location, we will first have to interpolate $\langle S_{11} \rangle$ from the cell centre yellow node to the red node. The value of $\langle S_{11} \rangle$ for the cell to the north, north-east, and east are included for interpolation. Once $\langle S_{11} \rangle$ is interpolated to the red node, we compute the product in Eq. (C.6).

For $k = 2$, we obtain,

$$\begin{aligned} RHS_{k=2} &= \langle S_{12} \rangle \langle \Omega_{22} \rangle - \langle \Omega_{12} \rangle \langle S_{22} \rangle. \\ &= -\langle \Omega_{12} \rangle \langle S_{22} \rangle. \end{aligned} \quad (\text{C.7})$$

The evaluation of the expression in Eq. (C.7) is done in the same way as explained Eq. (C.6), since the only term that is different is $\langle S_{22} \rangle$ in the place of $\langle S_{11} \rangle$ and they are both evaluated at the cell centre, i.e. yellow node (A).

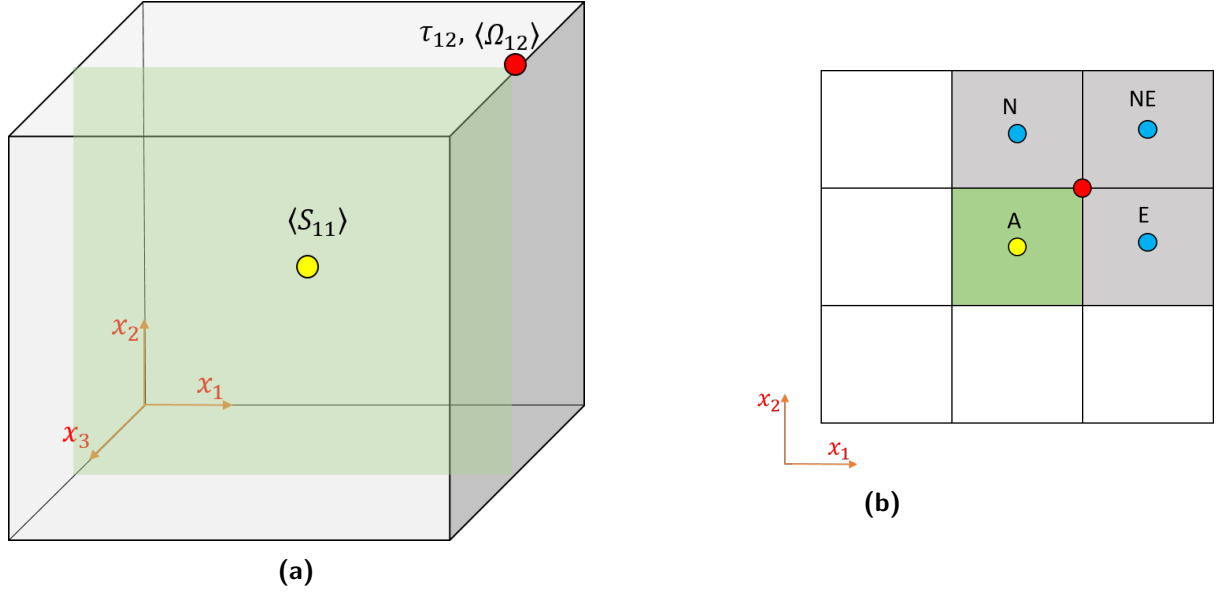


Figure C.5: (a) Discretisation of the tensor elements in the non-linear term required for τ_{12} when the index $k = 1$ and (b) the corresponding nodes of the current and the neighbouring cells on the shaded x_1x_2 - plane in (a). The cells to the north, north-east and east are shaded in grey.

For $k = 3$, we obtain

$$\begin{aligned} RHS_{k=3} &= \langle S_{13} \rangle \langle \Omega_{32} \rangle - \langle \Omega_{13} \rangle \langle S_{32} \rangle \\ &= -\langle S_{31} \rangle \langle \Omega_{23} \rangle + \langle \Omega_{31} \rangle \langle S_{23} \rangle. \end{aligned} \quad (\text{C.8})$$

The two terms in Eq. (C.8) are very similar in the sense that they are both product between two tensors which have indices (3, 1) and (2, 3). Hence, the procedure involved in evaluating the two terms the expression in Eq. (C.8) is also the same. For generality we represent this product using two generalised tensors, ϕ_{ij} as $\phi_{31}\phi_{23}$. The position of these elements on the computational grid is shown in Fig. C.6.

Since the position of τ_{12} , ϕ_{23} , and ϕ_{31} are all different, we first proceed by interpolating ϕ_{23} and ϕ_{31} (shown in orange and red) to the black node in Fig. C.6a. The east and the north cells, respectively are used for this operation. After this interpolation, we compute the product of the two interpolated components at the black node. Finally, the non-linear term is again interpolated to the grey node (marked with τ_{12}) in Fig. C.6 by performing an interpolation of the product evaluated for the current cell and the cell behind (in $-x_3$ direction). The planes along which the interpolation is done at each stage and the relevant nodes are colour coded in Fig. C.6b.

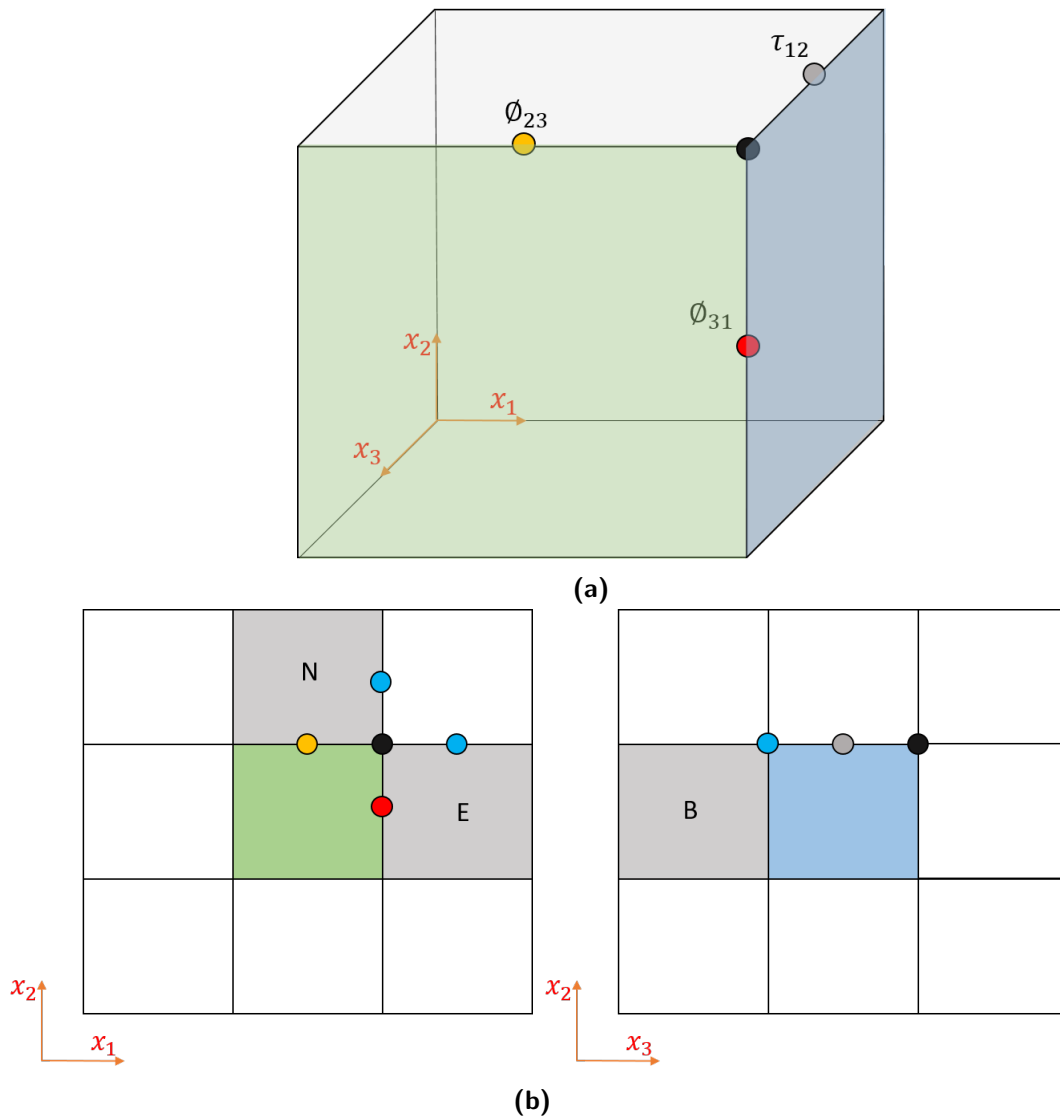


Figure C.6: (a) Discretisation of the tensor elements in the non-linear term required for τ_{12} when the index $k = 3$; (b) the cells required for interpolating the the tensor components to the black node shown in (a); (c) the cells required for interpolating the non-linear term at the black node onto the grey node where τ_{12} is evaluated.

Appendix D

A short note on inertial waves in rotating turbulence

The peculiar nature of rapidly rotating turbulence is attributed to the propagation of inertial waves plays a major role in the non-linear dynamics of rotating turbulence (Greenspan (1968)).

If we consider the linearised, inviscid governing equation, or in other words, if we consider the isolated effect of the Coriolis force while the non-linear and viscous forces are taken to be negligible in comparison, the solution of the pressure Poisson equation takes the form of (plain) inertial waves. The dispersion frequency and phase velocity corresponding to a wavevector is then given by

$$\sigma = 2\Omega_s \frac{\kappa_{\parallel}}{\|\kappa\|} = 2\Omega_s \cos \theta, \quad \text{and} \quad c_p = \frac{\sigma}{\|\kappa\|^2} \vec{\kappa}, \quad \text{respectively.} \quad (\text{D.1})$$

In Eq. (D.1), θ is the angle between the wavevector and the system rotation vector (or simply rotation axis). A wave that is travelling in a direction of $\vec{\kappa}/\|\kappa\|$ will propagate energy in the perpendicular direction with a velocity that is given by

$$c_g = 2\vec{\kappa} \times \frac{\vec{\Omega}_s \times \vec{\kappa}}{\|\kappa\|^3}. \quad (\text{D.2})$$

A low frequency disturbance (due to wavevectors that are nearly orthogonal to the rotation vector) will distribute energy along the axis of rotation at velocities that scale with $2\Omega_s/\kappa$ (Davidson (2004)). On the other hand, high frequency disturbances ($\kappa_{\parallel} = 0$) propagate in the direction perpendicular to the rotation axis at nearly negligible velocities. Though it seems from the theory that the horizontal and vertical modes are perfectly decoupled, in reality, the three-dimensional coupling is said to be taken care of by the pressure-fluctuations (Davidson (2004)).

